



MONASH University

**Additive Effect of Noble Metal to Nickel Based
Alumina Supported Catalyst**

By

Sheryl Soo Fun Moh

Bachelor (Honours) in Chemical Engineering

A thesis submitted in the fulfilment of the requirements

for the degree of

Research Master

Department of Chemical Engineering

Faculty of Engineering

Monash University

Australia

May 2018

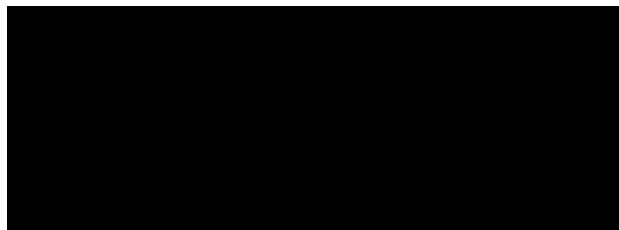
This page intentionally left blank

Copyright Notice

© The author 2018.

Under the Copyright Act 1968, this thesis must be used only under the normal conditions of scholarly fair dealing. In particular no results or conclusions should be extracted from it, nor should it be copied or closely paraphrased in whole or in part without the written consent of the author. Proper written acknowledgement should be made for any assistance obtained from the thesis

I certify that I have made all reasonable efforts to secure copyright permissions for third-party content included in this thesis and have not knowingly added copyright content to my work without the owner's permission.



Sheryl Soo Fun Moh

Contents

Chapter 1	Introduction	1
1.1	Background	2
1.1.1	Hydrogen Production via Aqueous Phase Reforming (APR) Reaction	2
1.1.2	Water-Gas Shift (WGS) Reaction	6
1.1.3	Catalyst	6
1.1.4	Catalyst Support	7
1.1.5	Synthesis of Catalyst	8
1.1.6	Impregnation Method	11
1.1.7	X-Ray Absorption Fine Structure (XAFS)	12
1.2	Research Aims	16
1.3	Outline for Dissertation	17
1.4	References	19
Chapter 2	Literature Review	23
2.1	Hydrogen Production	24
2.1.1	Glycerol Derived from Bio-Diesel	25
2.2	Catalyst	26
2.2.1	Monometallic Catalyst in the Development of Reforming Reaction	27
2.2.2	Bimetallic Catalyst in the Development of Reforming Reaction	29
2.2.3	Catalyst Support in the Development of Reforming Reaction	31
2.3	X-Ray Absorption Near Edge Spectroscopy (XANES) in the Development of Reforming Reaction	32
2.4	Gaps in Knowledge	33
2.5	References	35
Chapter 3	Methodology	41
3.1	Synthesis of Catalyst	42
3.1.1	Impregnation Method	42
3.2	Aqueous Phase Reforming (APR) of Glycerol	43
3.2.1	Gas Chromatography (GC) of Vapour Product	44
3.2.2	High Performance Liquid Chromatography (HPLC) of Liquid Product	45
3.3	Characterisation of Catalyst	47
3.3.1	Surface Area and Pore Structure by Physisorption	47

3.3.2	<i>Scanning Electron Microscope (SEM)</i>	48
3.3.3	<i>Transmission Electron Microscope (TEM)</i>	48
3.3.4	<i>CO - Temperature Programmed Desorption (TPD)</i>	48
3.3.5	<i>X-Ray Powder Diffraction (XRD)</i>	50
3.4	<i>X-Ray Absorption Near Edge Spectroscopy (XANES)</i>	51
3.5	<i>References</i>	53
Chapter 4 APR of Glycerol With Noble Metal-Nickel Based Catalyst Supported on Alumina		56
4.1	<i>Results and Discussions</i>	57
4.1.1	<i>Catalyst Characterisation</i>	57
4.1.2	<i>APR Activity</i>	62
4.2	<i>Conclusion</i>	65
4.3	<i>References</i>	66
Chapter 5 Ex-Situ XANES Analysis of Pd, Rh and Ru Mono-, Bi-Metallic Catalyst		68
5.1	<i>Results and Discussions</i>	69
5.1.1	<i>Ex-Situ XANES Analysis of Mono- and Bi-Metallic Catalyst</i>	69
5.1.2	<i>APR Activity</i>	76
5.2	<i>Conclusion</i>	78
5.3	<i>References</i>	80
Chapter 6 Conclusions and Recommendations		82
6.1	<i>Conclusions</i>	83
6.2	<i>Hypotheses</i>	85
6.3	<i>Recommendations</i>	85
6.4	<i>References</i>	87
Appendix		89
A.1	<i>Catalyst Characterisation</i>	90
A.1.1	<i>Surface Area and Pore Structure by Physisorption</i>	90
A.1.2	<i>CO-Temperature Programmed Desorption (TPD)</i>	92
A.2	<i>APR Activity</i>	94
A.2.1	<i>Rate of Hydrogen Production and Glycerol Conversion</i>	94
A.2.2	<i>Rate of Carbon Dioxide and Carbon Monoxide Production</i>	97

List of Figures

Chapter 1

1.1.1-1	Graph of Hydrogen and Alkane Selectivity against Oxygenated Hydrocarbon 1 wt% Oxygenated Hydrocarbon Over 3Pt/Al ₂ O ₃ catalyst at 538 K.....	3
1.1.4-1	Preparation of transition alumina.....	8
1.1.7-1	X-ray traversed a distance into the slab, the intensity has been reduced to $I = I_0 e^{-\mu x}$	13
1.3-1	Additive Effect of Noble Metal to Nickel Based Catalyst	17

Chapter 2

2.2.2-1	Relative rates of C-C bond cleavage reaction (white), WGS reaction (grey), methanation reaction (black)	28
---------	---	----

Chapter 3

3.2-1	APR reaction set up.....	43
3.2-2	Schematic diagram of APR reaction set up	43
3.2.2-1	Glycerol calibration curve on HPLC	46
3.2.2-2	1 wt% of unreacted glycerol in liquid product	47
3.3.4-1	CO-Temperature Programmed Desorption set up	48
3.3.4-2	Temperature and gas flow profile of CO Chemisorption	49

Chapter 4

4.1.1-1	XRD patterns of fresh and used alumina supported (i) Ni/Al ₂ O ₃ (ii) Ni:Pd(10:1)/Al ₂ O ₃ (iii) Ni:Pd(1:1)/Al ₂ O ₃ (iv) Pd/Al ₂ O ₃ (v) Ni:Rh(10:1)/Al ₂ O ₃ (vi) Ni:Rh(1:1)/Al ₂ O ₃ (vii) Rh/Al ₂ O ₃ (viii) Ni:Ru(10:1)/Al ₂ O ₃ (ix) Ni:Ru(1:1)/Al ₂ O ₃ (x) Ru/Al ₂ O ₃ . ◇ denotes alumina, X denotes Ni Oxide, Δ denotes Pd oxide, O denotes Rh oxide and □ denotes Ru oxide	58
4.1.1-2	TEM Images of (i) Fresh and (ii) Used Ru/Al ₂ O ₃	60
4.1.1-3	TEM Images of (i) Fresh and (ii) Used Ni: Rh (1:1)/Al ₂ O ₃ , (ii) Fresh and (iii) Used Rh/Al ₂ O	61
4.1.2-1	(i) Rate of hydrogen gas production and (ii) liquid glycerol conversion.....	62
4.1.2-2	(i) Ratio of CO ₂ /CO gas production (WGS reaction) and (ii) rate of CH ₄ production (methane reaction).....	62
4.1.2-3	Refractive Index Signal of liquid product mixture at 60 min (reaction condition: 210 °C,	

	35 bar, 10 sccm Argon, 2 wt% glycerol feedstock, Ru/Al ₂ O ₃ catalyst)	64
4.1.2-4	Refractive Index Signal of liquid product mixture at 60 min (reaction condition: 210 °C, 35 bar, 10 sccm Argon, 2 wt% glycerol feedstock, Ni:Pd(10:1)/Al ₂ O ₃ catalyst)	65
Chapter 5		
5.1.1-1	Normalised near spectra of (i) Pd foil, PdO, Ni:Pd(10:1)/Al ₂ O ₃ , Ni:Pd(1:1)/Al ₂ O ₃ , Pd/Al ₂ O ₃ (ii) Pd foil, PdO, Reduced Ni:Pd(10:1)/Al ₂ O ₃ , Reduced Ni:Pd(1:1)/Al ₂ O ₃ , Reduced Pd/Al ₂ O ₃ (iii) Rh foil, Rh ₂ O ₃ , Ni:Rh(10:1)/Al ₂ O ₃ , Ni:Rh(1:1)/Al ₂ O ₃ , Rh/Al ₂ O ₃ (iv) Rh foil, Rh ₂ O ₃ , Reduced Ni:Rh(10:1)/Al ₂ O ₃ , Reduced Ni:Rh(1:1)/Al ₂ O ₃ , Reduced Rh/Al ₂ O ₃ (v) Ru foil, RuO ₂ , Ni:Ru(10:1)/Al ₂ O ₃ , Ni:Ru(1:1)/Al ₂ O ₃ , Ru/Al ₂ O ₃ (vi) Ru foil, RuO ₂ , Reduced Ni:Ru(10:1)/Al ₂ O ₃ , Reduced Ni:Ru(1:1)/Al ₂ O ₃ , Reduced Ru/Al ₂ O ₃	69
5.1.1-2	The normalised near spectra obtained for (i) Pd foil, PdO, Ni:Pd(10:1)/Al ₂ O ₃ and Reduced Ni:Pd(10:1)/ Al ₂ O ₃ (ii) Rh foil, Rh ₂ O ₃ , Ni:Rh(10:1)/ Al ₂ O ₃ and Reduced Ni:Rh(10:1)/ Al ₂ O ₃ (iii) Ru foil, RuO ₂ , Ni:Ru(10:1)/Al ₂ O ₃ and Reduced Ni:Ru(10:1)/Al ₂ O ₃	70
5.1.1-3	Close-up of normalised near spectra obtained for (i) Pd foil, PdO and Reduced Ni:Pd(x:y)/Al ₂ O ₃ (ii) Rh foil, Rh ₂ O ₃ and Reduced Ni:Rh(x:y)/Al ₂ O ₃ (iii) Ru foil, RuO ₂ and Reduced Ni:Ru(x:y)/Al ₂ O ₃ where x:y = 10:1, 1:1, 0:1	72
5.1.1-4	Radial structure function of (i) Pd foil, PdO, Ni:Pd(10:1)/Al ₂ O ₃ , Ni:Pd(1:1)/Al ₂ O ₃ , Pd/Al ₂ O ₃ (ii) Pd foil, PdO, Reduced Ni:Pd(10:1)/Al ₂ O ₃ , Reduced Ni:Pd(1:1)/Al ₂ O ₃ , Reduced Pd/Al ₂ O ₃ (iii) Rh foil, Rh ₂ O ₃ , Ni:Rh(10:1)/Al ₂ O ₃ , Ni:Rh(1:1)/Al ₂ O ₃ , Rh/Al ₂ O ₃ (iv) Rh foil, Rh ₂ O ₃ , Reduced Ni:Rh(10:1)/Al ₂ O ₃ , Reduced Ni:Rh(1:1)/Al ₂ O ₃ , Reduced Rh/Al ₂ O ₃ (v) Ru foil, RuO ₂ , Ni:Ru(10:1)/Al ₂ O ₃ , Ni:Ru(1:1)/Al ₂ O ₃ , Ru/Al ₂ O ₃ (vi) Ru foil, RuO ₂ , Reduced Ni:Ru(10:1)/Al ₂ O ₃ , Reduced Ni:Ru(1:1)/Al ₂ O ₃ , Reduced Ru/Al ₂ O ₃	74
Appendix		
A.1.1-1	N ₂ physisorption isotherm linear plot (i) Ni/Al ₂ O ₃ (ii) Ni:Pd(10:1)/Al ₂ O ₃ (iii) Ni:Pd(1:1)/Al ₂ O ₃ (iv) Pd/Al ₂ O ₃ (v) Ni:Rh(10:1)/Al ₂ O ₃ (vi) Ni:Rh(1:1)/Al ₂ O ₃ (vii) Rh/Al ₂ O ₃ (viii) Ni:Ru(10:1)/Al ₂ O ₃ (ix) Ni:Ru(1:1)/Al ₂ O ₃ (x) Ru/Al ₂ O ₃	90
A.1.2-1	Rate of CO and CO ₂ desorption μmolg _{cat} ⁻¹ min ⁻¹ of (i) Ni/Al ₂ O ₃ (ii) Ni:Pd(10:1)/Al ₂ O ₃ (iii) Ni:Pd(1:1)/Al ₂ O ₃ (iv) Pd/Al ₂ O ₃ (v) Ni:Rh(10:1)/Al ₂ O ₃ (vi) Ni:Rh(1:1)/Al ₂ O ₃ (vii) Rh/Al ₂ O ₃ (viii) Ni:Ru(10:1)/Al ₂ O ₃ (ix) Ni:Ru(1:1)/Al ₂ O ₃ (x) Ru/Al ₂ O ₃	92
A.2.1-1	Rate of Hydrogen Gas Production with Standard Error Bar of Average 4 Runs (i) Ni:Pd(x:y)/Al ₂ O ₃ (ii) Ni:Rh(x:y)/Al ₂ O ₃ (iii) Ni:Ru(x:y)/Al ₂ O ₃	94

A.2.1-1	<i>Glycerol Conversion with Standard Error Bar of Average 4 Runs (i) Ni:Pd(x:y)/Al₂O₃ (ii) Ni:Rh(x:y)/Al₂O₃ (iii) Ni:Ru(x:y)/Al₂O₃</i>	96
A.2.2-1	<i>Rate of (i) Carbon Dioxide and (ii) Carbon Monoxide production</i>	97

List of Tables

Chapter 1

1.1.5-1	<i>Impregnation, ion exchange, co-precipitated, deposition-precipitation and sol-gel method</i>	10
---------	---	----

Chapter 3

3.1.1-1	<i>Mono- and bi- metallic catalyst sample.....</i>	42
3.2.1-1	<i>Parameters and formulas conventionally applied to evaluate APR performance ...</i>	45
3.4-1	<i>Photon Delivery System of XAFS.....</i>	51
3.4-2	<i>Sample to be analysed at Mode 3 using Si(311)</i>	52

Chapter 4

4.1.1-1	<i>Textual properties of the alumina supported mono- and bi-metallic catalysts.....</i>	57
4.1.1-2	<i>XRD of samples.....</i>	60

Abstract

Hydrogen production via aqueous phase reforming (APR) process presents important advantages when compared to the steam reforming: (i) the vaporization of the mixture is not necessary, reducing the energetic requirement. (ii) The decomposition reactions that take place at elevated temperatures are minimized. (iii) H_2 with low CO content is obtained because the water gas shift reaction (WGS) is favoured in the APR conditions.

An effective approach to obtain hydrogen via APR reaction is such that the catalyst must be active for the C-C bond cleavage and it must promote the WGS reaction. Meanwhile, to obtain liquid oxygenated products, the catalyst should be active in the C-O bond cleavage.

Attempt had been made on Ni based catalyst to enhance the catalytic performance in aqueous phase reforming (APR) of sugars and sorbitol to produce hydrogen. These catalysts were synthesised by impregnating the corresponding metal precursors on alumina, followed by calcination in air, resulting in nanoclusters (<20 nm in size) of Ni and noble metal finely dispersed on the surface of the support. Studies had demonstrated that addition of small amount of noble metal (atom ratio of Ni to noble metal up to 30:1) would enhance the catalytic activity, selectivity and durability several folds as compared with those of individual metals. For instance, it was suggested that the synergistic effects of noble metals with Ni increases the reducibility while decreases poisoning and carbon fouling as well as increases the rate of hydrogen transfer on the surface of the catalysts.

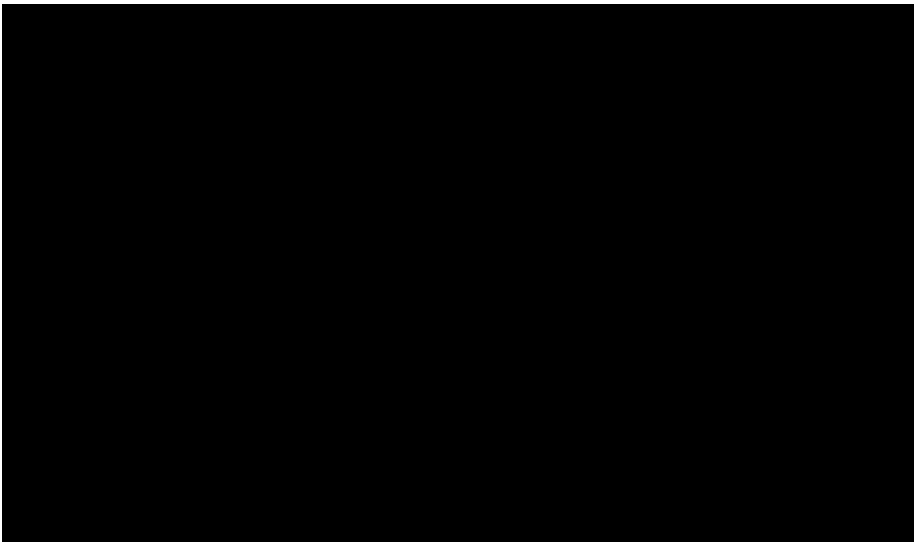
To improve the catalytic properties of mono- and bi-metallic sample, it was noteworthy to study the effect of various additive with difference metal loading such as Pd, Rh and Ru over Ni/ Al_2O_3 catalyst via aqueous phase reforming reaction of glycerol. In this research study, the chemical effect including their structural phase and oxidation state with the introduction of second metal to Ni catalyst prior to and after reduction will also be analysed. For instance, X-ray Absorption Near Edge Spectroscopy (XANES) is a potential useful technique to complement the chemical effect.

By combining the catalytic performance tests and results of X-ray Absorption Near Edge Spectroscopy (XANES), the experiments aimed to contribute to the elucidation of issues concerning the Ni-catalysed APR reactions include: (i) the change in oxidation state and phase of metal component (e.g. Pd, Rh and Ru) in Ni catalyst supported on γ - Al_2O_3 after reduction (ii) in depth understanding of the structural mechanism of various metal loading impregnated with Ni catalyst.

In the XANES analysis, the higher the metal loading impregnated on Ni catalyst (i) the metal particle size decreases with increasing Ni contents which in turn greater surface species (ii) the larger particles size prevents the catalyst from being easily reduced to its metallic state and this would influence the retention of catalytic activities (iii) bimetallic samples are slightly more oxide. This could also explained the overall rate of hydrogen production decreased in the following order: Ni:M (10:1)/Al₂O₃ > Ni:M(1:1)/Al₂O₃ > M(1:1)/Al₂O₃ (M= Pd and Ru). However, Rh based did not exhibit the general trend. The presence of Ni and support alumina prevent Rh catalyst from being easily reduced Rh metal. Therefore, introduction of noble metal to nickel catalyst greatly influences the reducibility of bimetallic catalyst.

General Declaration

I hereby declare that this thesis contains no material which has been accepted for the award of any other degree or diploma at any university or equivalent institution and that, to the best of my knowledge and belief, this thesis contains no material previously published or written by another person, except where due reference is made in the text of the thesis.



Date:

11/05/2018

.....

Acknowledgements

First, I would like to express my sincere gratitude to my main supervisor Dr. Akshat Tanksale for his guidance and supervision throughout this research project. Beside research advices, he had also provided me with invaluable assistant and support while I was in doubt and stress during my research. I would not have completed my studies without his supervision.

Second, my gratitude will go to my associate supervisor Dr. Lian Zhang for his confidence in me and agreed to take me on-board as his student. He had also introduced me to the XAFS expert Dr. Barbara Etschmann to provide me with great guidance with one of the chapter in the thesis. I am truly grateful with the unconditional advice and feedback she had given me. Also, sincere appreciation is extended to all staff in the Australian Synchrotron, particularly Peter Kappen for helping me with data analysis.

Next, I would like to acknowledge some of the research colleagues that provided me with valuable feedback and assist me through challenging times: Dr Teck Kwang Choo, Bai Qian, Teck Wei Ching, Negin Amini, Paunarmi Chandran, Sunaina Dayal and Dr. Bayzid Kazi as well as my office-mate: Madura Ananda Kumar, May Gin Lee, Amanda Lum, Jamie Castillo and Kahlil Desai for always bringing laughter and joy to share with, not to forget also the delicious snacks.

I would also like to give my sincere thanks to my fellow Catalysis for Green Chemicals group members. Special thanks to Dr. Alimohammad Bahmanpour, Dr. Fan Liang Chan, Teck Wei Ching, Tigabwa Ahmed, Negin Amini and Pratik Gholkar.

In addition, I would like to acknowledge Lilyanne Price, Jill Crisfield, Kim Phu, Harry Bouwmeester and Ross Ellingham for their invaluable assistance during my research studies. I am also grateful for all the assistance I received from MCEM. Thanks Russell King and Tim William for their time and expertise in training me to use the TEM.

Last but not least, I would like to thank my family for supporting me throughout all these years. Special love to my partner Peter So for all the supports and encouragement that are given to me. My hearty thanks for putting up with my down-time and stressful moment during my studies.

Abbreviations

APR	Aqueous Phase Reforming
BET	Brunauer Emmett Teller
BJH	Barret Joynew Halenda
DOE	Department of Energy
EXAFS	Extended X-Ray Absorption Fine Structure
FA	Fatty Acids
FID	Flame Ionization Detector
FWHM	Full Width at Half Maximum
GC	Gas Chromatograph
GHG	Green House Gases
HPLC	High Performance Liquid Chromatograph
IEA	International Energy Agency
IUPAC	International Union of Pure and Applied Chemistry
RGA	Residual Gas Analyser
RID	Refractive Index Detector
RSF	Radial Structure Function
SEM	Scanning Electron Microscope
SRS	Stanford Research System
TCD	Thermal Conductivity Detector
TEM	Transmission Electron Microscope
TPD	Temperature Programmed Desorption
WGS	Water Gas Shift
XAFS	X-Ray Absorption Fine Structure
XANES	X-Ray Absorption Near Edge Spectroscopy
XRD	X-Ray Diffraction

Nomenclature

μ	Absorption Coefficient
μ_0	Smooth Background Function
$\Delta\mu_0$	Jump in Absorption
θ	Bragg Angle
σ	Debye Waller Factor
β	Line Broadening at Half Maximum Intensity
δ	Phase Shift
λ	Wavelength
A	Surface Area
CN	Coordination Number
D	Particle Size
E	X-Ray of Energy
E_0	Threshold Energy
FT	Fourier Transformation
h	Planck's Constant
I	Transmitted X-Ray Intensities
I_0	Incident X-Ray Intensities
K	Shape Factor
k	Wave Vector
M	Metal Dispersion
m	Electron Mass
N	Total Number of Atoms
R	Radial Distance
r	Reforming Ratio
S	Selectivity
V	Volume
x	Homogenous Sample of Thickness
Y	Yield

This page intentionally left blank

CHAPTER 1: INTRODUCTION

Abstract

Outlined the background, objectives and scope of this research. Thesis organizations are also included in Chapter 1: Introduction.

Chapter Contents

1.1	Background	2
1.1.1	Hydrogen Production via Aqueous Phase Reforming (APR) Reaction	2
1.1.2	Water-Gas Shift (WGS) Reaction	6
1.1.3	Catalyst	6
1.1.4	Catalyst Support	7
1.1.5	Synthesis of Catalyst	8
1.1.6	Impregnation Method	11
1.1.7	X-Ray Absorption Fine Structure (XAFS)	12
	Extended X-Ray Absorption Fine Structure (EXAFS)	13
	X-Ray Absorption Near Edge Spectroscopy (XANES)	15
1.2	Research Aims	16
1.3	Outline for Dissertation	17
1.4	References	19

1.1 Background

The inter-related problems of energy and environment are among the biggest challenges facing the world today, most particularly with energy sustainability and carbon emissions from the fossil fuels. Hydrogen is a clean energy carrier with high energy density property 120.7 kJ/g and it has been projected as an important source of future energy supply [1]. Hydrogen is known as the clean energy carrier as it can be combusted and oxidised with only water vapour as a by-product while without emitting any environmental pollutant, such as, NO_x , CO_x and VOC_s . In 2003, the United States Department of Energy (DOE) launched an Energy Hydrogen Program to address the important of hydrogen in the needs of its application in chemical, petrochemical and food industries as well as fuel cells, internal engine combustion and in oil refining [2].

Hydrogen can be produced from fossil fuels, water electrolysis and splitting of biomass. However, the current debates concerning hydrogen economy are intimately linked to the clean production of hydrogen from fossil fuels (e.g., natural gas, collar propane, methane, gasoline, light diesel), dry biomass and biomass-derived liquid fuels (e.g., methanol and biodiesel), and water [3]. Although coal is cheap and widely available to produce hydrogen via coal gasification through water- gas shift (WGS) reaction, the undesired carbon dioxide emission is not friendly to the environment. Thus, hydrogen production and converted to electricity in fuel cells, leaving only water as a product is the ideal future energy source.

1.1.1 Hydrogen Production via Aqueous Phase Reforming (APR) Reaction

Steam reforming is the conventional approach to generate large amount of hydrogen by reforming a hydrocarbon source in the presence of steam over an appropriate catalyst [3]. In fact, steam reforming has been commercially chosen due to its high hydrogen yield, but they are mostly based on non-renewable fossil fuels and resulted in CO_x emissions [4]. Therefore, introducing biomass would be a highly desirable approach in future to diminish the use of fossil fuels. Efforts have been made into convert biomass to hydrogen. However, techniques including gasification, pyrolysis and enzymatic decomposition suffer from wither harsh conditions or complex requirements or low hydrogen production rates.

A new process then been discovered such that hydrogen could be efficiently produced from biomass at mild conditions around 500 K in a single reaction of aqueous phase reforming (APR) reaction [5]. As compared to steam reforming, this process is more energy saving because the vaporization of water and oxygenated of hydrocarbons is not required. In addition, APR reaction can be carried out at lower temperature to promote the thermodynamically favour water gas shift reaction, thus lead to low level of CO production [4]. In addition, the ideal carbon to oxygen ratio in reactant should be one and these can be easily obtained from renewable sources including glucose, cellulose, ethylene glycol, sorbitol and glycerol [6]. This can be proven as the Figure 1.1.1-1 shown below that feedstock having lower number of C-atom favours hydrogen selectivity rather than alkane selectivity [6].

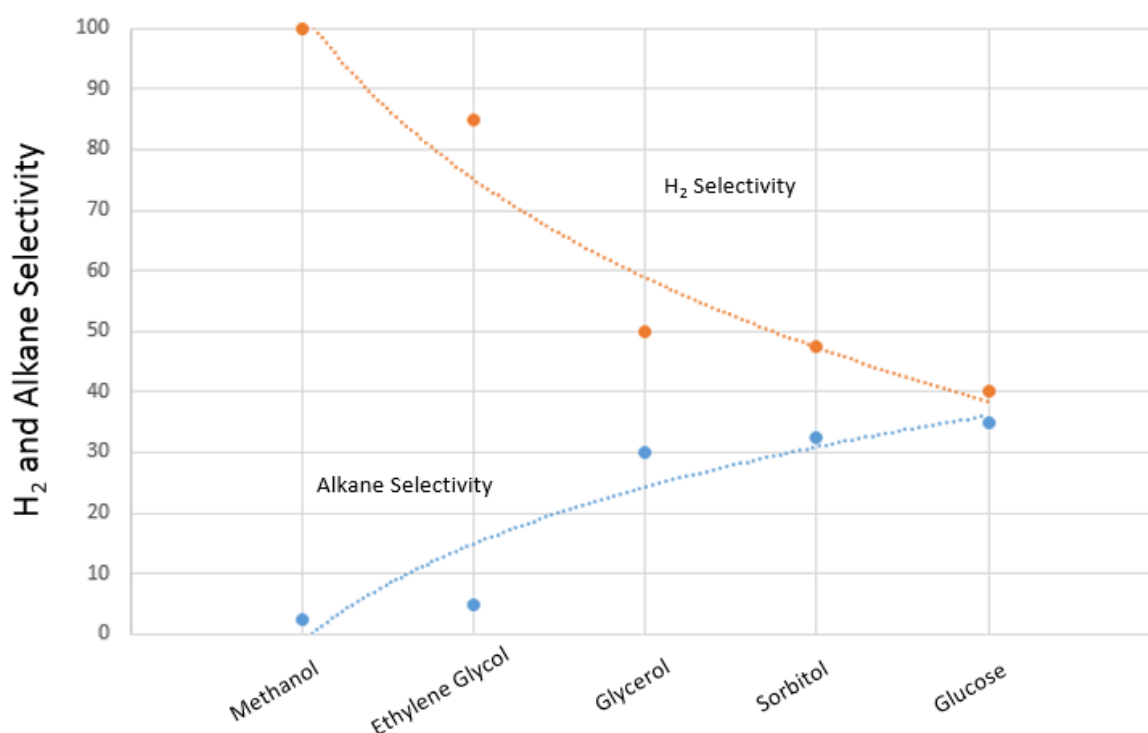


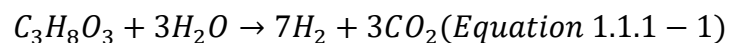
Figure 1.1.1-1: Graph of Hydrogen and Alkane Selectivity against Oxygenated Hydrocarbon 1 wt% Oxygenated Hydrocarbon Over 3Pt/Al₂O₃ catalyst at 538 K [6] [7] [8] (Reproduced from Dumesic, Permission Granted 12.07.02017)

They are also several advantages of hydrogen production via APR with carbohydrate source over existing steam reforming of hydrocarbon [9]:

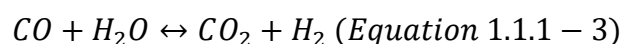
1. APR eliminates the need to vaporize both water and the oxygenated hydrocarbon which reduces the energy requirement for producing hydrogen.

2. The oxygenated compounds of interest are non-flammable and non-toxic, allowing them to be stored and handled safely.
3. APR occurs at reaction temperature where the water gas shift reaction is favourable, making it possible to generate hydrogen with low amounts of CO in a single chemical reactor.
4. APR is conducted at pressure (typically 15-50 bar) where the hydrogen-rich effluent can be effectively purified using pressure swing adsorption or membrane technologies and the carbon dioxide can also be effectively separated for either sequestration or use as a chemical.
5. APR occurs at low temperature that minimize undesirable decomposition reactions typically encountered when carbohydrates are heated to elevated temperatures.
6. Production of H₂ and CO₂ from carbohydrates may be accomplished in a single-step, low temperature process in contrast to the multi-reactor steam reforming system required for producing hydrogen from hydrocarbons.

Glycerol is a potentially a useful feedstock for hydrogen production because one mole of glycerol can produce up to seven moles of hydrogen according to the stoichiometric reaction shown below [4]:



In aqueous phase reforming (APR) of glycerol, the (endothermic) one step process takes place over a catalyst at low temperature (473-523K) and moderate pressure (1.6-4.0 MPa) [8]. APR of glycerol reactions occur at substantially low temperature than conventional alkane steam reforming (typically 923 K). The two reactions that would occur during the reactions conditions are the C-C cleavage and water gas shift reaction (refer Section 1.1.2) as shown below [4]:

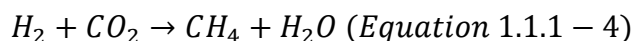


The product of aqueous phase reforming consist of two phases, namely, gas and liquid which can be collected from two different streams. The composition and flow rate of gaseous

products can be accurately measured. Among the produced gas, hydrogen is regarded as the main product of aqueous phase reforming and to be considered as the majority of performance parameters applied to evaluate APR reaction [7].

On the other hand, even though it is not explicitly stated on the APR Equation 1.1.1-1 above, the liquid products often comprise a complex mixture of hydrocarbons and oxygenated hydrocarbons, in some cases difficult to identify. Liquid product that could be present in a APR of glycerol: glyceraldehyde, hydroxyacetone, ethylene glycol, propylene glycol, 1,2-ethanediol, acetaldehyde, propanal, 1-propanal, 2-propanol, 1-propanol, ethanol, methanol, 2-methyl propylene, butane, pentane, acetic acid, propanoic acid, lactic acid [7]. However, some of these possible liquid bi-product will be discuss further in Chapter 4 Section 4.2.2.

With a lower operating temperature and the water gas shift reaction being favourable at a lower operating temperature, higher hydrogen production with low amount CO in a single reactor is achieved. Moreover, the important selectivity challenges govern the production of H₂ by APR because the mixture of H₂ and CO₂ formed in this process is thermodynamically unstable at low temperature with respect to the formation of methane [4]:



In order to promotes the production of hydrogen, the metal used in APR reaction not only catalysed the C-C cleavage bond but also active for the water gas shift reaction [6]. Water gas shift (WGS) reaction appears to one of the most crucial step in hydrogen production. Moreover, the catalyst should be inert to competing parallel and sequential reactions such as C-O cleavage and the methanation reaction as shown in Equation 1.1.1-4 above, which greatly deteriorate the yield of hydrogen.

In the case of APR over TiO₂ supported 5 wt% metal catalysts, the activity as well as the selectivity differ depending on the kind of metals with the following activity order: Ru > Rh > Pt > Ir. Over Pt/TiO₂ and Ir/TiO₂, a large amount of acetic acid was formed by the hydration of acetaldehyde with smaller amounts of CO₂ and CH₄ (1:1 ratio), indicating the absence of complete reforming process with water [11]. On the other hand, over Rh/TiO₂ and Ru/TiO₂ catalyst, major products were CH₄ and CO₂ with a smaller amount of liquid phase products and excess CH₄ was forms afterward indicating the operation of an unfavourable methanation

reaction [11]. Based on the catalytic activity, both Ru and Rh will be of interest of study and it would be also worthwhile analysing the effect of mono- and bi-metallic catalyst such as Ru, Rh, Ru-Ni and Rh-Ni on APR reaction.

On other hand, Pt, Ni, Co and Cu catalyst supported on Al_2O_3 , active C, SiO_2 , MgO, HUSY ($\text{SiO}_2/\text{Al}_2\text{O}_3=4.8$) and SAPO-11 were also studied. It was found that the activity of metal catalysts increased in the order of Co, Ni, Cu and Pt [1]. It was also found that the activity of supported Pt catalyst was given as follows: SAPO-11 < active carbon < HUSY < SiO_2 < MgO < Al_2O_3 [1]. Therefore, Al_2O_3 was the subject of this research study as compared to other catalyst support.

Although Pt catalysts are highly active for APR, the high cost of Pt makes it an undesirable element [10]. Pt catalysts supported on Al_2O_3 also suffer from severe deactivation due to coke deposition, oxidation or sintering [12]. Ni, on the other hand, show initial APR activity comparable to that of Pt, but was subject to significant deactivation [13]. Thus, it was recommended to improve the catalytic activities of the Ni catalysts by impregnating them with other metallic element [14].

1.1.2 Water-Gas Shift (WGS) Reaction

Since the early 1940, the WGS reaction has represented an important step in the industrial production of hydrogen [3]. In the reaction, the water in the form of steam is mixed with carbon monoxide to obtain hydrogen and carbon dioxide as shown below [10]:



The WGS reaction is reversible and exothermic [3]. Due to its exothermicity, the WGS reaction is thermodynamically unfavourable at elevated temperature, as illustrated by the continuous decline and eventual sign change in the Gibbs free energy as a function of temperature and the corresponding decreasing equilibrium constant as the temperature increased [3].

1.1.3 Catalyst

Catalysts play a vital role in sustaining the competitiveness of large parts of a modern economy. They are speciality chemicals, produced by a small number of expert companies, many of which are based in the EU. They are carefully formulated to provide uniformity of

properties in terms of performance and durability to the customer. In a number of process industries, most notably oil refining, chemical processing, and pharmaceuticals, modern catalysts deliver substantial improvements in selectivity, output quality and process innovation, as well as major reductions in energy consumption, feedstock use, waste and cycle time.

In the field of chemistry, 90% of chemical processes are catalysis reaction [7]. The International Union of Pure and Applied Chemistry (IUPAC) has defined a catalyst as “a substance that increases the rate of reaction without modifying the overall standard Gibbs energy change in the reaction [7]. The chemical process of increasing the reaction rate is called catalysis and the catalyst is both a reactant and a product of the reaction. The catalyst itself is not consumed by the overall reaction and is restored after each catalytic act. Furthermore, the catalyst does not influence the thermodynamical equilibrium composition after the cessation of the reaction [7].

Catalysts work by providing an alternative mechanism involving a different transition state and lower activation energy. Hence, catalysts can assist reactions that would not run without the presence of a catalyst, or perform them much faster, more specifically, or at lower temperatures. This means that catalysts reduce the amount of energy required to initiate a chemical reaction [8].

1.1.4 Catalyst Support

In order to testify the effect of the support on the activity and H₂ selectivity in APR reaction, APR reaction with 10 wt % ethylene glycol at operating temperature 210 and 225 °C over Pt supported on TiO₂, Al₂O₃, carbon, SiO₂, SiO₂-Al₂O₃, ZrO₂, CeO₂ and ZnO were conducted [9]. As a results, a high turnover frequency of 8-15 min⁻¹ at 225 °C was observed over Pt supported on TiO₂, carbon and Al₂O₃ while Pt supported on SiO₂-Al₂O₃ and ZrO₂ exhibited a moderate turnover frequency of about 5 min⁻¹ as compared to Pt supported on CeO₂, ZnO and SiO₂ with a lowest turnover frequency [9]. In addition, Pt supported on carbon, TiO₂ and SiO₂-Al₂O₃ also lead to the formation of gaseous alkanes and liquid phase alkane at higher conversion [9]. It can be concluded that alumina supported catalysts are active and selective for production of hydrogen in APR reaction [9].

Besides that, alumina is commonly used because it is relatively inexpensive and readily coupled with accessible pore structure. In synthesis of alumina catalyst support, the preparation route is similar as the preparation of the alumina that is smelted to give aluminium metal. Aluminium is dissolved in NaOH and separated from the impurities present in the original ore [10]. The resultant sodium aluminate solution is generally prepared from a solution of pure salt such as nitrate for its purity. The salt solution will then be treated with an alkali to give oxide precipitate and it is ready to be calcined to bring about dehydration as well as the formation of alumina [10]. It is important to note that the drying and calcination steps can be significant in determining the structure of the resultant alumina. This could be indicated in the formation of various transition alumina as shown in Figure 1.1.4-1 due to different calcination temperature. The forms of alumina other than γ -, χ - and η - Al_2O_3 are seldom used as catalyst support as their surfaces areas are much lower than those transition alumina [10].

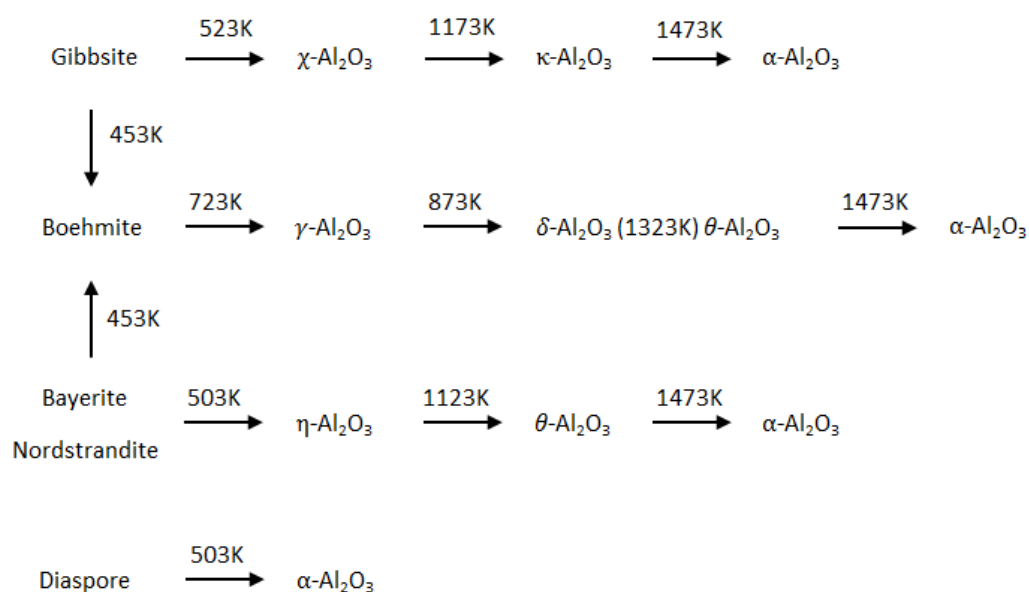


Figure 1.1.4-1: Preparation of transition alumina [10] (Reproduced from Julian, Permission Granted 12.07.02017)

1.1.5 Synthesis of Catalyst

The active phase of catalyst is introduced into the support structure by various preparation methods. The methods usually used to prepare supported nickel catalyst include

impregnation, deposition-precipitation, co-precipitation and sol gel as tabulated in Table 1.1.5-1 [11].

Table 1.1.5-1: Impregnation, ion exchange, co-precipitated, deposition-precipitation and sol-gel method

METHOD	DESCRIPTION	ADVANTAGES	DISADVANTAGES
Impregnation	Solution of the active phase is brought in contact with the support [12]	<ul style="list-style-type: none"> Usually employed for practical and economic reason Allow the use of pre-shaped or structured support, optimal properties can be selected [13] Simple and easy to operate as well as scale up the preparation of catalyst 	<ul style="list-style-type: none"> Difficulties in the control of the catalyst particle size and distribution Poor dispersion of catalyst [14]
Ion Exchanged	Allows introduction, in a controlled way, of a precursor from aqueous solution onto a support, ionic species from aqueous solution are attracted electrostatically by charged sites on the support surface [12].	<ul style="list-style-type: none"> Able to modify sample size and accessibility of the internal pores [12] 	<ul style="list-style-type: none"> High cost industrial application [15] Additional separation procedures have to be involved [16]
Co-Precipitated	Related to deposition precipitation (refer to Appendix A.1.4), but here the base and active precursor solution are injected simultaneously to the suspension of catalyst support [13].	<ul style="list-style-type: none"> Simple direct process 	<ul style="list-style-type: none"> Not easy to control and reproduce Not suitable for the preparation of high pure, accurate stoichiometric phase Does not work well if the reactants have very different solubility as well as different precipitate rate Difficulty in obtaining good macroscopic homogeneity [12]
Deposition-Precipitation	The chemical processes occurring involve a reactant which transforms the catalyst precursor into an insoluble form which is generated slowly in solution, and its concentration is raised homogeneously [17].	<ul style="list-style-type: none"> Well dispersed and homogeneous deposition High metal loading Strong precursor-support interaction Improved stability against sintering and higher catalytic activities [12] 	<ul style="list-style-type: none"> Active metals are randomly distributed over the surface of support [18] Complicated procedure
Sol-Gel	Involves first formation of a sol, which is a suspension of solid particles in a liquid then of a gel, which is a disphasic material with a solid encapsulating a liquid [19].	<ul style="list-style-type: none"> Versatility and excellent control over a product's properties Particle sizes, surface areas and mechanical properties can be altered according to the temperature, operating conditions and to the used precursor [20] Smaller particle size and morphological control in catalyst synthesis [21] Uniformity of products [21] Higher thermal stability and higher resistance to deactivation while allowing a better flexibility in controlling catalyst properties including its particle size, surface area and pore size distribution [20]. Low temperature processes and consolidation is possible [21] Sintering at low temperature also possible [21] Better homogeneity and phase purity High metal dispersion and loading 	<ul style="list-style-type: none"> Precipitation and formation of homogeneous gel [21] Several steps are involved, close monitoring of the process is needed [21] Complicated procedure

The most common method for catalyst preparation is impregnation method was due to its simplicity but it results in poor control over nickel dispersion [11]. On the other hand, ion-exchanged, deposition-precipitation, sol-gel method provide a better control over nickel dispersion. The following methods were not chosen in the study due to the fact that ion exchanged is restricted to the capacity of the support utilized; deposition-precipitation and sol-gel methods involve several complicated steps which may results in costly catalyst [22].

1.1.6 Impregnation Method

Impregnated catalysts are prepared by impregnating (e.g., spraying) a solution of a metal salt or mixture onto pellets of a porous support [23]. The metal loading in the finished catalyst is typically 1~5% but can be as low as 0.1%. When liquid is slowly added to a porous solid powder, the liquid is first absorbed in the pores and the powder will flow as if it is dry. When the pores have been filled the outside of the granules suddenly become wet, the granules will tend to stick together and the powder will form lumps instead of flowing freely. The pellets are dried and calcined to transform the metal into an insoluble form [23]. The distribution of the metal is controlled through the interaction of the metal solution(s) with the support; for example, through varying the metal counter-ion, through control of pH or through addition of chelating agents to the impregnation liquid. The drying conditions can also affect the distribution.

Compared to other catalyst preparation methods, impregnation offers several advantages. For example, the pellets may be shaped before the metal is added, the filtering and washing of the catalysts are not necessary, low metal loadings are easily achieved and control over the distribution of the metal in pellets is possible [23]. There are also come disadvantages. For example, high metal loadings are not possible without multiple impregnations steps and an impregnation solution may not be available [23].

In a parallel, it has been studied that hydrogen production by APR reaction could be maximised without the change of catalyst properties during reduction and calcination. Therefore, the nature of the catalyst before and after catalyst reduction would have remarkable influence on the activity as well as the distribution of the products. In this study, the effect of the changes in metal component (e.g. Ni, Pd, Ph and Ru) alumina supported

catalyst on the activities of APR of reaction was investigated by the X-ray Absorption Fine Structure (XAFS) spectroscopy.

1.1.7 X-Ray Absorption Fine Structure (XAFS)

X-ray absorption spectroscopy (XAS) refers to the details of how X-rays are absorbed by an atom at energies near and above the core-level binding energies of that particular atom. The absorption of X-ray on the high energy side of absorption edges does not vary monotonically in condensed matter but has a complicated behaviour which extends past the edge up to about ~ 1 keV [24]. This non-monotonic variation is known as the X-ray absorption fine structure (XAFS). XAFS spectroscopy is the only spectroscopic technique that provides information on the electronic and structural properties of catalysts under reaction conditions and in the presence of reactants. This is true, because XAFS is only one of the few probes that utilises photons exclusively (i.e., photon in and using transmission or fluorescence yield photons out). X-ray diffraction (XRD) is similar in this regard, but it requires longer range order and provides only geometric information [25].

A monochromatic beam of X-ray of the energy, E , which passes through a homogeneous sample of the thickness, x as attenuated in Figure 1.1.7-1 [26]. In analogy to the Lambert Beer law, it can be described as [27]:

$$I(E) = I_0(E)e^{-\mu(E).x} \text{ (Equation 1.1.7 – 1)}$$

where $I_0(E)$ and $I(E)$ are the incident and transmitted X-ray intensities and $\mu(E)$ is the linear absorption coefficient which describes how strongly X-ray are absorbed as a function of X-ray energy E . Generally, $\mu(E)$ smoothly decreases as the energy increases (approximately as $1/E^3$), the X-ray become more penetrating [24]. At certain energies, the absorption increases drastically and gives rise to an absorption edge. Each such edge occur when the energy of the incident photons is just sufficient to cause excitation of a core electron of the absorbing atom to a continuum state, to produce photoelectron. Accordingly, the absorption edge rises from the electronic transitions from the innermost states to unoccupied states above.

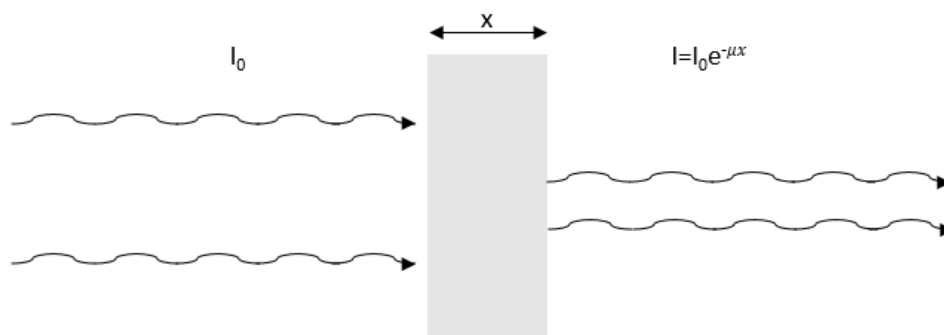


Figure 1.1.7-1: X-ray traversed a distance x into the slab, the intensity has been reduced to $I = I_0 e^{-\mu x}$ [27]

In short, XAFS is formed when the energy of the incoming photons is large enough to excite an electron from a deeper core level to a vacant excited state or to the continuum, a sharp rise in the absorption intensity appears. This sharp rise is denoted as the threshold energy or absorption edge.

The X-ray absorption fine structure is typically divided into two regimes: X-ray absorption near edge structure (XANES) and extended-X-ray absorption fine structure (EXAFS) [24]. XANES occurs in the region from the edge to approximately 40 eV above the edge while EXAFS extends from ~ 40 eV to 1000 eV above the edge [28]. The reason for this division into the XANES and EXAFS regions is that the XANES region is theoretically difficult to describe while the EXAFS region is relatively simple to interpret. XANES is sensitive to the treatment of interactions between the photoelectron and the core hole while the effects of the core hole on the EXAFS are relatively weak. Quantitative analysis of EXAFS has been available since the 1970s and the standard technique have been developed to extract the parameters of interest [28]. On the other hand, quantitative XANES analysis has only been available for a few years and is not a widely used technique.

Extended X-Ray Absorption Fine Structure (EXAFS)

The EXAFS process can be thought of as an in situ electron diffraction, in which X-ray absorbing atom is the photoelectron source. When the kinetic energy of the ejected photoelectron is great enough to enable it to escape the bound state, it interacts with electron in the bound states of other atoms within the local chemical environment surrounding the absorber [29]. Energetically, the continuum is up to several hundred electron volts (eV) above the absorption edge. Interactions between ejected photoelectron and other electrons produce secondary sources of scattering and interference on return of the

backscattering waves to the absorber. Interferences between outgoing scattering and incoming backscattering wave results in low frequency oscillations between ~ 50 and ~ 1000 eV above the absorption edge [30]. These oscillations constitute EXAFS and are area of interest as they contain structural and chemical information specific to the scattering atomic shells. Quantitatively, the amplitude of the EXAFS oscillations also able to identify the type and number of backscattering atoms as well as the distribution of these atoms [31].

XAFS spectrum consists of a range of increasing X-ray energies, single- and multiple- scattering events dominate in different portions of the spectrum. The higher energy portions of EXAFS spectra are dominated by single-scattering events. Therefore, the simplest theory of these spectra is based on the single scattering plane-wave approximation. In this approximation, the electron wave is viewed as a plane wave, rather than a spherical wave to simplify the mathematical derivation. The plane wave approximation assumes that the atomic radii are much smaller than the inter-atomic distances, and is valid only for higher k-values ($k > 3\text{\AA}$) where k is the wave vector refer also to Equation 1.1.7-2. At lower k values the curved wave or spherical wave, theory has to be used, to give reasonable agreement with experiment [25].

$$k = \sqrt{\frac{2m(E - E_o)}{h^2}} = 0.263\sqrt{(E - E_o)(\text{in eV})} \text{ (Equation 1.1.7 - 2)}$$

where E_0 is absorption edge energy and m is the electron mass.

EXAFS function is defined in the oscillations well above the absorption edge as $x(E)$ [24]:

$$x(E) = \frac{\mu(E) - \mu_0(E)}{\Delta\mu_0(E)} \text{ (Equation 1.1.7 - 3)}$$

where $\mu(E)$ is the measured absorption coefficient, $\mu_0(E)$ is a smooth background function representing the absorption of an isolated atom and $\Delta\mu_0(E)$ is the measured jump in the absorption $\mu(E)$ at the threshold energy E_0 . It is common to convert X-ray energy to k, the wave vector as depicted in Equation 1.1.7-2. The primary quantity for EXAFS is then $x(k)$, the oscillations as a function of photoelectron wave number and $x(k)$ is often referred to simply as “the EXAFS” [24].

In EXAFS data analysis, the oscillatory fine structure $x(k)$ is first extracted from the data by subtracting a smooth background function μ_0 . The most prevalent method for obtaining μ_0 is to fit the curve to a cubic or other spline function which is constrained to have low curvature [32]. The oscillatory EXAFS signal $x(k)$ is then Fourier transformed to real (R) space which gives an amplitude that is akin to a radial distribution function with contributions from longer scattering paths parking at higher R value where R is the interatomic distance. The Fourier transformation of $x(k)$ is defined as [33]:

$$FT(R) = \frac{1}{\sqrt{2\pi}} \int_{k_{min}}^{k_{max}} k^n x(k) e^{i2kR} dk \quad (\text{Equation 1.1.7 - 4})$$

Phase correction gives a $|x(R)|$ which is akin to the radial distribution functions. The peak at the Fourier transform appear at approximately different shell distance. Fitting model to the data is performed in R space using a limited range of Fourier transformed data in order to isolate the contribution from a relatively small number of short scattering paths. Thus, the parameters that are determined from the fitting of the theoretical model to the experimental EXAFS data are the average coordination number CN, ΔR , ΔE_0 , Debye Waller factor σ^2 and reduction factor S_0^2 which includes the intrinsic losses due to inelastic effects in the data analysis [34]. The final EXAFS equation can then be derived [24]:

$$x(k) = \sum_j \frac{CN_j}{kR_j^2} S_0^2 f_j(k) e^{-2k^2\sigma_j^2} e^{-\frac{2R_j}{\lambda(k)}} \sin[2kR_j + \delta_j(k)] \quad (\text{Equation 1.1.7 - 5})$$

Where N is the coordination number and Debye Waller Factor, σ which is the fluctuation in R_j due to thermal motion or structural disorder, $\delta_j(k)$ is the phase shift.

X-Ray Absorption Near Edge Spectroscopy (XANES)

The physical principles that govern EXAFS apply equally in the XANES region. However, at low kinetic energy the photoelectron mean-free-path increases dramatically. XANES is a much larger signal than EXAFS and can be obtained at lower concentrations. The processes responsible for near edge absorption structure are related to ejection of core electrons into continuum states and involve single- and multiple-scattering events off the first atomic shell surrounding the absorber as well as multiple-scattering events from more distant atomic shells [35].

XANES can be used to extract chemical information about oxidation states, three dimensional geometry and coordination environment of elements under investigation. Clearly, the edge position and shape is sensitive to formal valence state, ligand type and coordination environment. Hence, the edge features (position and shape) reflect oxidation state and coordination environments in vicinity of the absorber [35].

In terms of edge features, an important and common application of XANES is to use the shift of the edge position to determine the valence state. This technique is now routinely applied to discern coordination and oxidation states of metals in compounds and complexes [35]. On the other hand, the height and positions of pre-edge peaks are reliably used to empirically determine oxidation state and coordination chemistry [35].

1.2 Research Aims

Aqueous phase reforming (APR) of glycerol is the attractive technique due to low temperature requirements, less CO production and possible value added by-products formations. In this research, the primary objective is to compare the rate of hydrogen production between monometallic Ni and bimetallic Ni catalyst.

Then, by combining the mono-/bi-metallic catalytic performance tests and X-ray Absorption Near Edge Spectroscopy (XANES) analysis, the experiments aimed to contribute to the elucidation of issues concerning the Ni-catalysed APR reactions include:

- (i) To study effect of bi-metallic catalyst loading in the rate of hydrogen production via aqueous phase reforming (APR) of glycerol. The ratio of noble metal to Ni was systematically varied while keeping the total metal loading same to study their effect.
- (ii) To study the change in the oxidation state of bi-metallic catalyst with the change in type and loading of noble metal. It is believe that noble metals assist in Ni reduction via hydrogen spill-over effect which helps maintain Ni sites in active Ni⁰ state during the reaction in presence of oxidising agents such as water.
- (iii) To study the relationship between noble metal Ni alloy formation on the dispersion of active sites and subsequently their effect on rate of hydrogen production in APR of glycerol.

1.3 Outline for Dissertation

The overall research study outlined can be illustrated in Figure 1.3-1:

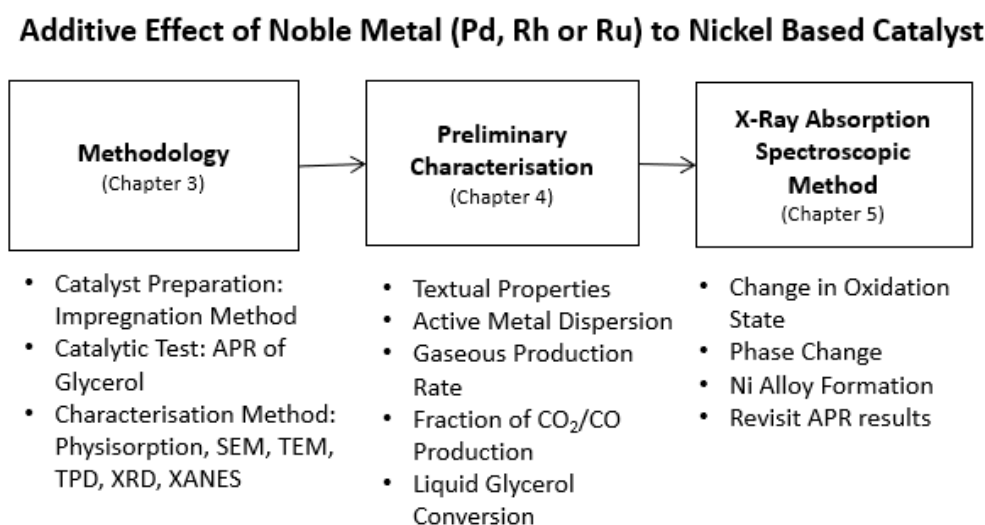


Figure 1.3-1: Additive Effect of Noble Metal to Nickel Based Catalyst

The thesis is divided into seven chapters including **Chapter 1** on general introduction. **Chapter 2** outlined the detailed literature review on hydrogen production, catalyst, and aqueous phase reforming (APR) reaction as well as X-Ray Absorption Fine Structure (XAFS).

Chapter 3 describes the synthesis methodology of the catalysts, fabrication of APR test rig facility and basic principle behind the characterization techniques used in this study. Ni:Pd(10:1)/Al₂O₃, Ni:Pd(1:1)/Al₂O₃, Pd/Al₂O₃, Ni:Rh(10:1)/Al₂O₃, Ni:Rh(1:1)/Al₂O₃, Rh/Al₂O₃, Ni:Ru(10:1)/Al₂O₃, Ni:Ru(1:1)/Al₂O₃ and Ru/Al₂O₃ were prepared by impregnation method. Catalyst were then put into application of glycerol APR and liquid as well as gaseous products were analysed. Samples were also characterized by various physiochemical techniques, including Physisorption, Scanning Electron Microscope (SEM), Transmission Electron Microscope (TEM), Temperature Programmed Desorption (TPD), X-Ray Diffraction (XRD) and X-Ray Absorption Near Edge Spectroscopy (XANES).

Chapter 4 investigates the effect of various additives with different metal loading such as Pd, Rh or Ru over Ni catalyst supported on alumina via aqueous phase reforming (APR) reaction of glycerol with respect to their catalyst activity, such as overall rate of hydrogen, carbon monoxide, carbon dioxide, methane production and glycerol conversion. The ratio of noble metal to Ni was systematically varied while keeping the total metal loading same while studying their characterisation. Textural properties of the mono- and bi-metallic Nickel

catalyst including BET surface area, total pore volume, mean pore diameter, metal dispersion were analysed. Furthermore, a greater understanding of the relationship between noble metal Ni alloy formation on the dispersion of active sites, change in particle size and electronic effect of bimetallic catalyst as compared to monometallic Ni/Al₂O₃ and subsequently their effect on rate of hydrogen production in APR of glycerol. The ratio of CO₂/CO and methane production were analysed to study the extent of WGS and methanation reaction respectively.

Chapter 5 stresses out the changes in oxidation state and structural mechanism of various metal loading impregnated with Ni catalyst prior to and after reduction with the X-ray Absorption Near Edge Spectroscopy (XANES) technique. This chapter then contribute in investigating how these changes affect the rate of hydrogen production via APR of glycerol.

Chapter 6 provide an overall summary and conclusions of the work presented in the thesis. Future work needed were also recommended in this chapter.

1.4 References

- [1] H. Heubaum, F. Biermann, Integrating global energy and climate governance: The changing role of the International Energy Agency, *Energy Policy*, 87 (2015) 229-239.
- [2] R. Turner, Renewable hydrogen could fuel Australia's next export boom after CSIRO breakthrough, in, *ABC News*, 2017.
- [3] G. Wen, Y. Xu, H. Ma, Z. Xu, Z. Tian, Production of hydrogen by aqueous-phase reforming of glycerol, *international journal of hydrogen energy*, 33 (2008) 6657-6666.
- [4] B. Zhang, X. Tang, Y. Li, Y. Xu, W. Shen, Hydrogen production from steam reforming of ethanol and glycerol over ceria-supported metal catalysts, *International Journal of Hydrogen Energy*, 32 (2007) 2367-2373.
- [5] S. Adhikari, S. Fernando, S.R. Gwaltney, S. Filip To, R. Mark Bricka, P.H. Steele, A. Haryanto, A thermodynamic analysis of hydrogen production by steam reforming of glycerol, *International Journal of Hydrogen Energy*, 32 (2007) 2875-2880.
- [6] C. Crisafulli, S. Scirè, S. Minicò, L. Solarino, Ni–Ru bimetallic catalysts for the CO₂ reforming of methane, *Applied Catalysis A: General*, 225 (2002) 1-9.
- [7] I. Fechete, Y. Wang, J.C. Védrine, The past, present and future of heterogeneous catalysis, *Catalysis Today*, 189 (2012) 2-27.
- [8] EuropeanNickelInstitute, *The Importance of Nickel Compounds: Catalysts*, in, San Francisco, 2007.
- [9] J. Shabaker, G. Huber, R. Davda, R. Cortright, J. Dumesic, Aqueous-phase reforming of ethylene glycol over supported platinum catalysts, *Catalysis Letters*, 88 (2003) 1-8.
- [10] J.R. Ross, *Heterogeneous catalysis: fundamentals and applications*, Elsevier, 2011.
- [11] H. Chen, M. Xue, S. Hu, J. Shen, The effect of surface acidic and basic properties on the hydrogenation of laurionitrile over the supported nickel catalysts, *Chemical Engineering Journal*, 181 (2012) 677-684.

- [12] J.A. Schwarz, C. Contescu, A. Contescu, Methods for preparation of catalytic materials, *Chemical Reviews*, 95 (1995) 477-510.
- [13] J.A. Anderson, M.F. Gracia, *Supported Metals in Catalysis*, World Scientific London, 2005.
- [14] G. Wilde, *Nanostructured Materials*, Elsevier, Great Britain, 2009.
- [15] Remco, Ion Exchange, in, USEPA 1981.
- [16] A.A. Zagorodni, *Ion Exchange Materials*, Elsevier, Great Britain 2007.
- [17] R.A.V. Santen, P.W.N.M.V. Leeuwen, J.A. Moulijn, B.A. Averill, *Catalyst: An Integrated Approach*, 2nd ed., Elsevier, Netherlands, 2000.
- [18] J. van de Loosdrecht, A. van Dillen, A. Van Der Horst, A. Van Der Kraan, J. Geus, Nickel-iron catalysts prepared by homogeneous deposition-precipitation of cyanide complexes on a titania support, *Topics in Catalysis*, 2 (1995) 29-43.
- [19] D.A. Ward, E. Ko, Sol-Gel Preparation of Zirconium Oxide, *PREPRINTS OF PAPERS-AMERICAN CHEMICAL SOCIETY DIVISION FUEL CHEMISTRY*, 40 (1995) 356-356.
- [20] G. Gonçalves, M.K. Lenzi, O.A.A. Santos, L.M.M. Jorge, Preparation and characterization of nickel based catalysts on silica, alumina and titania obtained by sol-gel method, *Journal of Non-Crystalline Solids*, 352 (2006) 3697-3704.
- [21] S. Vivekanandhan, *Experimental Techniques*, in, 2010.
- [22] B. Delmon, P.A. Jacobs, R. Maggi, J.A. Martens, P. Grange, G. Poncelet, *Preparation of Catalysts*, Elsevier Science, Netherlands, 2012.
- [23] A. Basrur, D. Sabde, Chapter 4 - Catalyst Synthesis and Characterization A2 - Joshi, Sunil S, in: V.V. Ranade (Ed.) *Industrial Catalytic Processes for Fine and Specialty Chemicals*, Elsevier, Amsterdam, 2016, pp. 113-186.
- [24] A. Gaur, B.D. Shrivastava, H. Nigam, X-Ray Absorption Fine Structure (XAFS) Spectroscopy—A Review, *Proceedings of the Indian National Science Academy*, 79 (2013) 921-966.

- [25] D. Koningsberger, B. Mojet, G. Van Dorssen, D. Ramaker, XAFS spectroscopy; fundamental principles and data analysis, *Topics in catalysis*, 10 (2000) 143-155.
- [26] J.J. Rehr, R.C. Albers, Theoretical approaches to x-ray absorption fine structure, *Reviews of modern physics*, 72 (2000) 621.
- [27] B.K. Agarwal, *X-ray spectroscopy: an introduction*, Springer, 2013.
- [28] J. Kas, Toward quantitative calculation and analysis of x-ray absorption near edge spectra, in, University of Washington, 2009.
- [29] S.R. Sutton, M. Newville, 15.12 - Synchrotron x-Ray Spectroscopic Analysis A2 - Holland, Heinrich D, in: K.K. Turekian (Ed.) *Treatise on Geochemistry (Second Edition)*, Elsevier, Oxford, 2014, pp. 213-230.
- [30] W. Gates, *Handbook of clay science, X-ray absorption spectroscopy*. Elsevier, Amsterdam, (2006) 789-864.
- [31] S. Kelly, D. Hesterberg, B. Ravel, Analysis of soils and minerals using X-ray absorption spectroscopy, *Methods of soil analysis. Part, 5* (2008) 387-463.
- [32] M. Newville, P. Liviš, s.Y. Yacoby, J. Rehr, E. Stern, Near-edge x-ray-absorption fine structure of Pb: A comparison of theory and experiment, *Physical Review B*, 47 (1993) 14126.
- [33] P.J. Riggs-Gelasco, T.L. Stemmler, J.E. Penner-Hahn, XAFS of dinuclear metal sites in proteins and model compounds, *Coordination chemistry reviews*, 144 (1995) 245-286.
- [34] M.L. Barbelli, M.D. Mizrahi, F. Pompeo, G.F. Santori, N.N. Nichio, J.M. Ramallo-Lopez, EXAFS Characterization of PtNi Bimetallic Catalyst Applied to Glycerol Liquid-Phase Conversion, *The Journal of Physical Chemistry C*, 118 (2014) 23645-23653.
- [35] A.J. Berry, A.C. Harris, V.S. Kamenetsky, M. Newville, S.R. Sutton, The speciation of copper in natural fluid inclusions at temperatures up to 700 °C, *Chemical Geology*, 259 (2009) 2-7.

This page intentionally left blank

CHAPTER 2: LITERATURE REVIEW

Abstract

Literature were reviewed on hydrogen production from aqueous phase reforming with various catalyst samples as well as XAFS techniques.

Chapter Contents

2.1	Hydrogen Production.....	24
2.1.1	Glycerol Derived from Bio-Diesel	25
2.2	Catalyst.....	26
2.2.1	Monometallic Catalyst in the Development of Reforming Reaction	27
2.2.2	Bimetallic Catalyst in the Development of Reforming Reaction	29
2.2.3	Catalyst Support in the Development of Reforming Reaction	31
2.3	X-Ray Absorption Near Edge Spectroscopy (XANES) in the Development of Reforming Reaction	32
2.4	Gaps in Knowledge.....	33
2.5	References	35

2.1 Hydrogen Production

Since the 19th century, global carbon dioxide emissions from fossil fuel combustion have grown from almost zero to over 31 gigatons annually, making energy consumption the most important source of greenhouse gas (GHG) emissions by far [1]. Therefore, there would be a major need to seek for alternative energy source.

Hydrogen energy is considered to be an ideal energy carrier in the future because it is environmentally clean and efficient for energy conversion as compared to conventional fossil fuel combustion. If air is used for flame combustion of hydrogen, insignificant amount of NO_x are generated, otherwise, only water vapours are emitted during combustion of hydrogen.

As hydrogen being a clean energy source, some key players in the industry sees the potential in hydrogen energy being one of the most promising energy substitution to prevent the diminishing of fossil fuels and reduce impact on the environment. In Japan, the 2020 Tokyo Olympics will be also showcasing its dream of becoming a hydrogen society, as it shifts away from nuclear power after the Fukushima disaster [2]. The Australian governments are beginning to actively embrace the potential of hydrogen as a lean alternative fuel source and export industry. South Australia, for example, is looking to invest hydrogen projects via \$ 150 million clean energy fund as it tried to secure its energy supplies. The ACT government announced last year it would spend \$ 180 million on hydrogen projects, including a fleet of cars and refuelling station. It comes as the Australian Renewable Energy Agency recently made the exporting renewable energy such as hydrogen one of its top priorities for \$ 800 million of investments [2].

In view of growing environmental concerns such as global warming and the depletion of fossil fuels reserves, major efforts are being dedicated in developing the utilisation of renewable energy sources [3]. Over the last decade, renewable energy source such as biodiesel has been successfully used as an alternative fuel and as fossil fuel additive, on the other hand, its productions are also expected to grow in the future. With increased production of biodiesel, a glut of glycerol (C₃H₈O₃) can be obtained as a by-product during bio-diesel production by trans-esterification of vegetable oils, which are available at low cost in large supply renewable raw materials [4]. Currently, glycerol is used in many applications, such as personal care, food,

oral care, tobacco, polymer and pharmaceutical applications [5]. However, explosive growth of biodiesel industry has created a glut in glycerol that has demeaned the market value of this commodity. Therefore, it is important to find an alternative uses for glycerol. One such possibility is using glycerol as a source of producing hydrogen.

In this aspect, study had dealt with hydrogen production of feedstock glycerol which can be derived from biomass. Glycerol, the main by-product in the production of bio-diesel is a promising source for future bio-refineries as it can be converted to various derivatives used in fuels, chemicals, automotive, pharmaceuticals and detergent. One tonne of biodiesel yields about 110 kg of crude glycerol or about 100 kg of pure glycerol [6]. Consequently, the production cost of biodiesel can also be lowered by selling waste glycerol. The price of glycerol was dropped from \$0.43/kg in 2003 to \$0.18/kg and \$0.02/kg in 2010 for pure and crude glycerol respectively [7].

2.1.1 Glycerol Derived from Bio-Diesel

Glycerol derived from the biodiesel production process has a dark colour and contains variable amounts of soap, catalyst, alcohol (typically methanol), monoglycerides, diglycerides, glycerol oligomers, polymers, water and unreacted triacylglycerols and biodiesel. This crude glycerol contain glycerol concentrations of 40 to 85% depending on the efficiency of the steps involved in the biodiesel production process [8]. When subjected to a partial purification process involving the addition of mineral acid the derivatives of fatty acids are removed and the glycerol content increases to 80-85% and the product contains water, methanol and dissolved salts [8].

In thermal decomposition of glycerol, the major constituents of the compounds formed are carbon monoxide, hydrogen and carbon dioxide. The gaseous mixture resulting from this process also contains small proportions of compounds such as methane and short chain alcohols such as methanol, ethanol, ethylene, acetaldehyde, acetic acid, acetone, acrolein, ethanol and water [9]. Glycerol reforming processes are a promising alternative for hydrogen production, since glycerol is a co-product of the production of biodiesel obtained from renewable sources.

Steam reforming of glycerol is the method most commonly used by the chemical industry to produce hydrogen. In this process, glycerol reacts with water vapor in the presence of a catalyst, producing mainly hydrogen, carbon dioxide and carbon monoxide [10] [11]. According to previous studies, the best results for the glycerol steam reforming process are obtained at temperature in the range of 525-725 °C [10] [12] [13] [14] [15]. However, the process is difficult to control in this temperature range; moreover, high temperatures increase operating costs, energy consumption and the cost of material for construction of reactor. At lower temperature, the main products formed are H₂, CO₂ and CH₄ decreasing the selectivity for H₂.

In the last decade, many research has been done regarding the heterogenous catalysis involved in the steam reforming reaction of glycerol. Catalysts suitable for glycerol steam reforming are the ones that can cleave the C-C, O-H and C-H bonds. The ones that stand out are Ni based catalysts with various supports and promoters. They are also used in large scale industrial processes because of their ready availability and low cost.

Ni-Cu-Al catalyst in hydrogen production by glycerol steam reforming was carried out in a fixed bed continuous flow reactor under atmospheric pressure and temperature of 500-600 °C [16]. The catalyst was synthesised by the co-precipitation method with variable pH. The results revealed that with excess water, large amount of hydrogen is produced while CH₄ and CO formation is almost negligible.

Pt catalysts on different supports such as SiO₂, Al₂O₃, ZrO₂ and Ce₄Zr for glycerol steam reforming at temperature below 450 °C were previously studied [17]. The catalysts prepared with acid properties showed low activity with formation of side products. On the other hand, the support with neutral properties afforded a catalyst with good activity for gaseous products, high selectivity for H₂.

2.2 Catalyst

More efficient catalytic processes require improvements in the catalytic activity and selectivity. Both aspects can be improved by the tailored design of catalytic materials with the desired structure and the desired dispersion of active sites [18]. For instance, heterogeneous

catalysis reactions such as those predominantly used in petroleum refining, a catalyst is highly active if it has the capacity through its large inner surface to adsorb large amounts of reaction gas [19].

In aqueous phase reforming, catalysts should promote C-C bond cleavage and water gas shift reaction. In addition, the cleavage of C-O bonds and hydrogenation of CO and CO₂ should be minimised. These could be dictated by the type of active species – monometallic or bimetallic, catalyst support and synthesis methods which will be discussed in depth in the following Section 2.2.1 - 2.2.3.

2.2.1 Monometallic Catalyst in the Development of Reforming Reaction

The most commonly encountered active species including metals, oxides and sulphides capable of catalysing either specific reaction or a whole range of related reactions [20]. Metal species, mostly transition metals are typically used for hydrocarbon related reactions such as hydrocarbon reforming or steam reforming of natural gas. In the hydrocarbon reactions, transition metals can absorb C-C bond selectively resulting in cleavage and formation of CH-OH group adsorbed on metal. CO-OH then dehydrogenates to produce CO and H₂ [21]. Oxides are most commonly used in selective reactions which they can exhibit either acidic or basic properties. The oxides of transition metals combined with other oxides are surrounded by an electronic holes which allows the hydroxyl groups to move on the surface of the catalyst and the ability to store hydrogen or oxygen in its structure [22]. The deficiency of oxygen of oxides would lead to the formation of electronic holes which makes them semi-conductor. These holes, in fact, are capable of receiving or giving oxygen and play a role as a regulator of existing oxygen in the catalysts [22]. On the other hand, sulphides can be used in hydrodesulphurization in which involving sulphur-containing reactions.

In APR reaction of ethylene glycol at pressure 22 bar and 483 K, active species such as nickel (Ni), palladium (Pd), ruthenium (Ru) and rhodium (Rh) supported on silica were analysed for their overall catalytic activity and hydrogen selectivity [23]. It was observed that the overall catalytic activity for ethylene glycol APR decreases in the order: Ni > Ru > Rh ~ Pd [23]. On the other hand, the hydrogen selectivity decreases in the order: Pd > Ru > Ni > Rh [23].

Palladium catalyst exhibited the highest selectivity of H₂ production, approximately 98% while nickel and ruthenium catalyst exhibited low selectivity of H₂ production even though they showed a relatively high selectivity of CO₂ production [23]. It was suggested that low levels of CO were produced as compared to the amount of CO₂ production during APR reaction of ethylene glycol as well as significant nickel catalyst deactivation at operating temperature of 225 °C [23].

In further catalytic studies, the step-by-step reactions occurred during APR were compared as shown in the Figure 2.2.1-1 below, including the relative rates of C-C bond cleavage during ethane hydrolysis, WGS reaction took place over different metals [23] [24] [25] [26]:

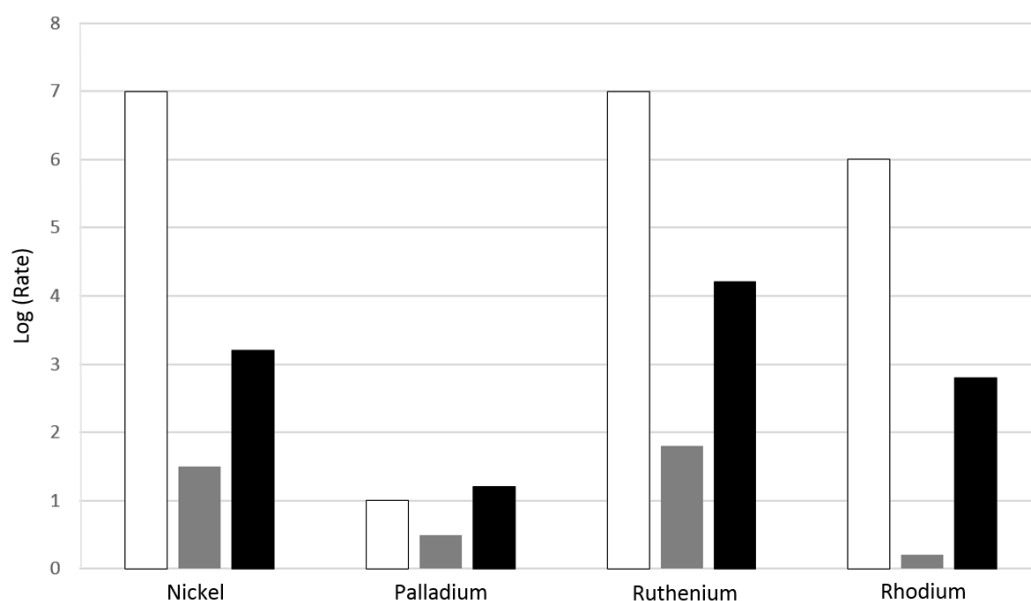


Figure 2.2.1-1: Relative rates of C-C bond cleavage reaction (white), WGS reaction (grey), methanation reaction (black) [24] [25] [26] [23] (Reproduced from Davda, Permission Granted 12.07.02017)

Among the metals, it was observed that ruthenium and nickel are the two highest rate of C-C bond cleavage and WGS reaction followed by rhodium and palladium. The trend is also similar to that of relative rate of methanation.

Therefore, after the various metal studies in their overall catalytic activity, selectivity of hydrogen production, relative rate in C-C bond cleavage and WGS reaction, nickel and ruthenium exhibit the suitability of catalysis in APR reaction despite of its high relative rate of methanation.

2.2.2 Bimetallic Catalyst in the Development of Reforming Reaction

Many studies have been evidenced that bimetallic catalysts are more active and selective than monometallic catalysts for H₂ production in steam reforming reaction. For instance, catalyst precursors composed of Ni/Mg/Al oxides with added La and Ce were tested in ethanol steam reforming reaction [27]. The catalyst precursors consist of a mixture of oxides, with the nickel in the form of NiO strongly interacting with the support Mg/Al. The reaction data showed that the addition of Ce and La resulted in better H₂ production at 550 °C. The CeNi catalyst provided with the higher ethanol conversion, with lower acetaldehyde production, possibly due to a favouring of water adsorption on the weakly interacting clusters of CeO₂ on the surface [27].

Another study on steam reforming of ethanol, the catalytic activity of Ni/La₂O₃-Al₂O₃ catalyst was modified with noble metal Pt and Pd. It was analysed that the formation of inactive nickel aluminate was prevented by the presence of La₂O₃ dispersed on the alumina [28]. The promoting effect of noble metals included a marked decrease in the reduction temperatures of NiO species interacting with the support, due to the hydrogen spillover effect, facilitating greatly the reduction of the promoted catalyst [28]. It was seen that the addition of noble metal stabilized the Ni sites in the reduced state throughout the reaction, increasing ethanol conversion and decreasing coke formation, irrespective of the nature or loading of the noble metal [28].

In steam reforming of glycerol, the catalytic activity of Ni/CeO₂-Al₂O₃ catalysts modified with noble metals, including Pt, Ir, Pd and Ru were investigated. The results showed that the formation of inactive nickel aluminate was prevented by presence of CeO₂ dispersed on alumina [29]. The promoting effect of noble metals included a decrease in the reduction temperatures of NiO species interacting with the support due to the hydrogen spillover effect. It was seen that the addition of noble metal stabilized the Ni sites in the reduced state along the reforming reaction, increasing glycerol conversions and decreasing the coke formation. The highest catalytic performance was obtained for the NiPd catalyst which presented an effluent gaseous mixture with the highest H₂ yield with low amounts of CO [29].

In carbon dioxide reforming of methane, addition of manganese to Ni/Al₂O₃ improves the stability of the catalyst in the reaction [30]. Manganese addition promotes the adsorption of

CO₂ by forming reactive carbonate species and the surface of nickel is partly covered by patches of MnO_x. Both effects appear responsible for the suppression of carbon deposition over Ni/MnO-Al₂O₃ [30].

However, few previous studies were conducted on bimetallic catalyst in aqueous phase reforming. For instance, Pt and Ni in various ratios supported on alumina doped with 3 wt% ceria and resulting materials were characterised and tested as catalyst for the APR of glycerol. Amongst the catalyst, bimetallic 1Pt-6Ni/3CeAl consists of 1 wt% Pt and 6 wt% Ni gave the highest H₂ yield (86%) and gas phase C yield (94%) [31]. Adding Ni impacted the crystallite and electronic structure of Pt. These effects likely to conspired to produce the higher glycerol conversion and gas phase C yield as well as high H₂ yield [31].

It was also found that the rate of hydrogen production via APR of sorbitol to be the highest for co-impregnated Ni-Pt/Alnf, followed by ZrO₂ and CZ_xS supported catalysts [32].

In Ko studies, Pt-Ni bimetallic catalysts was found to have more active sites than monometallic Pt or Ni catalysts [33].

Tupy found that after 24 hrs on stream in APR of ethylene glycol, Pt-Ni catalyst was more active than a Pt monometallic catalyst. This is due to the segregation of Ni and the Ni-enriched surface of the catalyst [34].

Manfro suggested that Ni-Cu bimetallic catalysts prepared from hydrotalcite-like precursor exhibited a higher activity than monometallic catalysts in the APR of glycerol. Ni-Cu bimetallic catalysts encouraged the alloy phase formation and Ni reducibility after reduction as well as the active metal dispersion [35].

It was also reported that 15Ni-5Cu/LaAl₂O₃ exhibited the highest glycerol conversion and hydrogen selectivity. The addition of the secondary metal had attributed to smaller crystal size, higher metal dispersion, higher surface area and enhanced the catalysts reducibility [36].

As compared to hydrogen production via steam reforming reaction, there have been only a few studies have been attempted in analysing catalytic activity of introduction of secondary metal to nickel catalyst with respect to hydrogen production in APR of glycerol. Therefore, in

this research study, the bimetallic Ni-M (Pd, Rh and Ru) catalytic system were introduced and analysed via aqueous phase reforming of glycerol.

2.2.3 Catalyst Support in the Development of Reforming Reaction

Many heterogeneous catalysts used in industry consist of very small metal particles on a support. Since the catalysis occurs at the surface of the metal particles, the catalysts are prepared to expose a large surface area, typically $10 - 100 \text{ m}^2\text{g}^{-1}$ of catalyst. A support also contains pores having irregular shapes. These pores fall into three size ranges. Micropores have diameter 2 nm or less and are due to the "roughness" of the solid surface itself, or the structure of the crystal lattice. Pore diameter in between 2nm to 50 nm falls in the mesopore size range. Macropores have diameter of 50 nm or more and are formed from cracks/spaces between crystallites. [37].

They exercise several functions, primarily to increase and stabilize the area of the metal particles. The size of the metal particles may be reported as the total area of the metal surface, as the diameter of the metal particles (commonly 3- 15 nm) and as the so-called metal dispersion (defined as the fraction of all metal atoms that are present at the metal particle surface, commonly from 20 up to about 80%) [37]. It also provides mechanical strength and thermal stability to metal particles in return facilitate a higher metal dispersion [38]. Moreover, the catalytic activity and production selectivity also depends significantly on the type of supports used.

In APR reaction, the H_2 production selectivity of ethylene glycol over silica supported catalyst is lower than alumina supported catalyst [23]. The more acidic supports (e.g. $\text{SiO}_2\text{-Al}_2\text{O}_3$) lead to high selectivity for alkane formation, whereas the more neutral/basic supports favour hydrogen production. For instance, the effect of supports including Al_2O_3 , SiO_2 , AC, MgO, HUSY and SAPO-11 on the activity and selectivity of hydrogen production via APR of glycerol using a fixed bed flow reactor were studied [3]. It was reported that the overall activity of Pt supported catalyst increased in the order of: SAPO-11 < HUSY < SiO_2 < MgO < Al_2O_3 [3]. Pt supported on basic support resulted in high activity and higher hydrogen molar concentration whereas acidic support increase alkane formation [3].

2.3 X-Ray Absorption Near Edge Spectroscopy (XANES) in the Development of Reforming Reaction

XANES techniques had been demonstrated on monometallic nickel catalyst supported on alumina. Three different nickel loadings were assessed [39]. XANES demonstrated that nickel particles are partially reduced during steam reforming of ethanol and are more oxidized after co-feeding oxygen. XANES also showed that the catalyst bed is predominantly oxidized at the entrance, where ethanol is mainly dehydrogenated to acetaldehyde [39].

In bimetallic catalyst XANES studies, two groups of catalysts containing Ni and/or Co metals and Mg/AlO_x as support material were analysed. The results show that bimetallic Ni-Co catalysts resulted in smaller nanoparticles upon reduction [40].

Also, the effect of potassium in the structural properties of a Ni/Al₂O₃ catalyst had been analysed [41]. In the XANES analysis, it was indicated that the presence of potassium facilitates the reduction of nickel during the activation treatment (heat treatment in H₂ at 773K, 2hr) [41].

Mono-metallic nickel and rhodium catalysts and bimetallic Ni-Rh catalysts were prepared and evaluated for catalysing steam and auto-thermal reforming of n-butane [42]. XANES analysis showed the presence of rhodium in Ni stabilized the spinel phase as well as NiO_x species upon reforming while Ni alone was mostly reduced into metallic species [42]. The XANES data also evidenced of Ni-Rh alloy during preparation and even further an accelerated aging at 900 °C in H₂/H₂O atmosphere [42].

XANES studies were also used to analysed samples in steam reforming, oxidative steam reforming, auto-thermal reforming reactions.

In steam reforming of ethanol, the effect of ceria in cobalt-ceria-alumina catalyst was studied using *in situ* XANES at Co K-edge and Ce L_{III} – edge [43]. The introduction of ceria in this catalyst resulted in a significant removal of Co from CoAl₂O₄ spinel phase to Co to CoO phases. The Co K-edge revealed the symmetry changes in Co according to the temperature and atmosphere in reduction process [43]. The stability of Co sites as well as oxidation state of ceria in operando steam reforming of ethanol reaction [43]. After reduction of Ce⁴⁺ to Ce³⁺, no

significant changes were observed by XANES. Co/Ce/Al₂O₃ catalyst exhibited as promising material to be applied in hydrogen production in steam reforming reaction [43].

In oxidative steam reforming of ethanol, the effect of Co addition on the structural properties of Ni/Al₂O₃ was studied. The XANES analysis indicated that the Co addition into the Ni/Al₂O₃ system has a considerable effect on the metal-support interaction, by assisting the formation of NiO and Co₃O₄ species weakly interacting with the alumina surface compared to the monometallic system [44]. It was found that the reducibility of the metallic oxides species in bimetallic CoNi/Al₂O₃ catalysts increases with increasing the Co content. The bimetallic CoNi/Al₂O₃ exhibited a higher resistance to oxidation compared to that of monometallic system in the reaction by hindering the oxidation of the metallic Ni and Co particles on the surface [44].

In auto-thermal reforming of methane, the effects of Pt trace addition to the oxi-reduction properties of Ni/Al₂O₃ catalysts were investigated [45]. The *in situ* XANES analysis for Pt-Ni/Al₂O₃ under H₂ and CO revealed that the presence of Pt sites can initiate the NiO reduction process by rapid dissociation of H₂ and migration of atomic H to the NiO surface by hydrogen spillover [45]. On the other hand, *in situ* XANES analysis under CH₄ showed that the presence of Pt sites induces the activation of methane, probably by initial dissociation of methane (CH₄ → CH₃ + H) followed by migration of atomic H to NiO surface [45]. The catalytic test results demonstrate that Pt is an important promoter to maintain Ni in the metallic state at the inlet region of the catalytic bed [45].

2.4 Gaps in Knowledge

In previous studies of aqueous phase reforming reaction, it was described that addition of minute quantities of noble metal to Ni, forms alloy catalyst increased the rate of hydrogen formation. The increase in the activity was believed to be due to two factors. First, the increase in reducibility of the Ni catalysts resulted in higher number of active sites. Second, alloying of Ni decreased the CO binding energy on the active metal sites which reduced catalyst poisoning and also increased the fraction of active sites available for the reforming reactions.

To date only a few studies have been attempt in analysing the effect of introduction of secondary metal to nickel catalyst. However, no XAS study on Ni:Pd, Ni:Rh and Ni:Ru bimetallic catalyst have been conducted and understanding of their effect on APR of glycerol. Even though these catalysts have been used for APR, their promotion effect is not fully understood.

Therefore, it is important to stress the change in the particle size, oxidation state and synergistic effect of bi-metallic catalyst with the change in type and loading of noble metal. The ratio of noble metal to Ni was systematically varied while keeping metal loading same to study their effect. Subsequently, their effect on rate of hydrogen production in APR of glycerol.

2.5 References

- [1] H. Heubaum, F. Biermann, Integrating global energy and climate governance: The changing role of the International Energy Agency, *Energy Policy*, 87 (2015) 229-239.
- [2] R. Turner, Renewable hydrogen could fuel Australia's next export boom after CSIRO breakthrough, in, *ABC News*, 2017.
- [3] G. Wen, Y. Xu, H. Ma, Z. Xu, Z. Tian, Production of hydrogen by aqueous-phase reforming of glycerol, *international journal of hydrogen energy*, 33 (2008) 6657-6666.
- [4] B. Zhang, X. Tang, Y. Li, Y. Xu, W. Shen, Hydrogen production from steam reforming of ethanol and glycerol over ceria-supported metal catalysts, *International Journal of Hydrogen Energy*, 32 (2007) 2367-2373.
- [5] S. Adhikari, S. Fernando, S.R. Gwaltney, S. Filip To, R. Mark Bricka, P.H. Steele, A. Haryanto, A thermodynamic analysis of hydrogen production by steam reforming of glycerol, *International Journal of Hydrogen Energy*, 32 (2007) 2875-2880.
- [6] A. Behr, J. Eilting, K. Irawadi, J. Leschinski, F. Lindner, Improved utilisation of renewable resources: new important derivatives of glycerol, *Green Chemistry*, 10 (2008) 13-30.
- [7] R.L. Maglinao, B.B. He, Catalytic thermochemical conversion of glycerol to simple and polyhydric alcohols using raney nickel catalyst, *Industrial & Engineering Chemistry Research*, 50 (2011) 6028-6033.
- [8] C.A. Schwengber, H.J. Alves, R.A. Schaffner, F.A. da Silva, R. Sequinel, V.R. Bach, R.J. Ferracin, Overview of glycerol reforming for hydrogen production, *Renewable and Sustainable Energy Reviews*, 58 (2016) 259-266.
- [9] G. Yang, H. Yu, F. Peng, H. Wang, J. Yang, D. Xie, Thermodynamic analysis of hydrogen generation via oxidative steam reforming of glycerol, *Renewable Energy*, 36 (2011) 2120-2127.
- [10] S. Adhikari, S. Fernando, S.R. Gwaltney, S.D. Filip To, R. Mark Bricka, P.H. Steele, A. Haryanto, A thermodynamic analysis of hydrogen production by steam reforming of glycerol, *International Journal of Hydrogen Energy*, 32 (2007) 2875-2880.

- [11] E.A. Sánchez, M.A. D'Angelo, R.A. Comelli, Hydrogen production from glycerol on Ni/Al₂O₃ catalyst, *International Journal of Hydrogen Energy*, 35 (2010) 5902-5907.
- [12] K.S. Avasthi, R.N. Reddy, S. Patel, Challenges in the Production of Hydrogen from Glycerol – A Biodiesel Byproduct Via Steam Reforming Process, *Procedia Engineering*, 51 (2013) 423-429.
- [13] S. Adhikari, S.D. Fernando, A. Haryanto, Hydrogen production from glycerin by steam reforming over nickel catalysts, *Renewable Energy*, 33 (2008) 1097-1100.
- [14] J.M. Silva, M.A. Soria, L.M. Madeira, Challenges and strategies for optimization of glycerol steam reforming process, *Renewable and Sustainable Energy Reviews*, 42 (2015) 1187-1213.
- [15] A. Iriondo, J.F. Cambra, M.B. Güemez, V.L. Barrio, J. Requies, M.C. Sánchez-Sánchez, R.M. Navarro, Effect of ZrO₂ addition on Ni/Al₂O₃ catalyst to produce H₂ from glycerol, *International Journal of Hydrogen Energy*, 37 (2012) 7084-7093.
- [16] B. Dou, C. Wang, Y. Song, H. Chen, Y. Xu, Activity of Ni–Cu–Al based catalyst for renewable hydrogen production from steam reforming of glycerol, *Energy Conversion and Management*, 78 (2014) 253-259.
- [17] F. Pompeo, G. Santori, N.N. Nichio, Hydrogen and/or syngas from steam reforming of glycerol. Study of platinum catalysts, *International Journal of Hydrogen Energy*, 35 (2010) 8912-8920.
- [18] I. Fechete, Y. Wang, J.C. Védrine, The past, present and future of heterogeneous catalysis, *Catalysis Today*, 189 (2012) 2-27.
- [19] EuropeanNickelInstitute, *The Importance of Nickel Compounds: Catalysts*, in, San Francisco, 2007.
- [20] J.R. Ross, *Heterogeneous catalysis: fundamentals and applications*, Elsevier, 2011.
- [21] K.I. Gursahani, R. Alcalá, R.D. Cortright, J.A. Dumesic, Reaction kinetics measurements and analysis of reaction pathways for conversions of acetic acid, ethanol, and ethyl acetate over silica-supported Pt, *Applied Catalysis A: General*, 222 (2001) 369-392.

- [22] A. Alouche, Preparation and characterization of Copper and/or Cerium catalysts supported on Alumina or Ceria, *Jordan Journal of Mechanical and Industrial Engineering*, 2 (2008) 111-116.
- [23] R.R. Davda, J.W. Shabaker, G.W. Huber, R.D. Cortright, J.A. Dumesic, Aqueous-phase reforming of ethylene glycol on silica-supported metal catalysts, *Applied Catalysis B: Environmental*, 43 (2003) 13-26.
- [24] J.H. Sinfelt, Specificity in Catalytic Hydrogenolysis by Metals, in: H.P. D.D. Eley, B.W. Paul (Eds.) *Advances in Catalysis*, Academic Press, 1973, pp. 91-119.
- [25] D.C. Grenoble, M.M. Estadt, D.F. Ollis, The chemistry and catalysis of the water gas shift reaction: 1. The kinetics over supported metal catalysts, *Journal of Catalysis*, 67 (1981) 90-102.
- [26] M.A. Vannice, The catalytic synthesis of hydrocarbons from H₂CO mixtures over the group VIII metals: II. The kinetics of the methanation reaction over supported metals, *Journal of Catalysis*, 37 (1975) 462-473.
- [27] A.F. Lucrédio, J.D.A. Bellido, E. Assaf, Effects of adding La and Ce to hydrotalcite-type Ni/Mg/Al catalyst precursors on ethanol steam reforming reactions, *Applied Catalysis A: General*, 388 (2010) 77-85.
- [28] L.P. Profeti, J.A. Dias, J.M. Assaf, E.M. Assaf, Hydrogen production by steam reforming of ethanol over Ni-based catalysts promoted with noble metals, *Journal of Power Sources*, 190 (2009) 525-533.
- [29] L.P. Profeti, E.A. Ticianelli, E.M. Assaf, Production of hydrogen via steam reforming of biofuels on Ni/CeO₂-Al₂O₃ catalysts promoted by noble metals, *International Journal of Hydrogen Energy*, 34 (2009) 5049-5060.
- [30] S.-H. Seok, S.H. Han, J.S. Lee, The role of MnO in Ni/MnO-Al₂O₃ catalysts for carbon dioxide reforming of methane, *Applied Catalysis A: General*, 215 (2001) 31-38.

- [31] M. Rahman, T.L. Church, M.F. Variava, A.T. Harris, A.I. Minett, Bimetallic Pt–Ni composites on ceria-doped alumina supports as catalysts in the aqueous-phase reforming of glycerol, *RSC Advances*, 4 (2014) 18951-18960.
- [32] A. Tanksale, J.N. Beltramini, G.M. Lu, A review of catalytic hydrogen production processes from biomass, *Renewable and Sustainable Energy Reviews*, 14 (2010) 166-182.
- [33] E.-Y. Ko, E.D. Park, K.W. Seo, H.C. Lee, D. Lee, S. Kim, Pt–Ni/ γ -Al₂O₃ catalyst for the preferential CO oxidation in the hydrogen stream, *Catalysis letters*, 110 (2006) 275-279.
- [34] S.A. Tupy, A.M. Karim, C. Bagia, W. Deng, Y. Huang, D.G. Vlachos, J.G. Chen, Correlating ethylene glycol reforming activity with in situ EXAFS detection of Ni segregation in supported NiPt bimetallic catalysts, *ACS Catalysis*, 2 (2012) 2290-2296.
- [35] R.L. Manfro, T.P. Pires, N.F. Ribeiro, M.M. Souza, Aqueous-phase reforming of glycerol using Ni–Cu catalysts prepared from hydrotalcite-like precursors, *Catalysis Science & Technology*, 3 (2013) 1278-1287.
- [36] Y. Kim, Crystallographic study of cerium aluminate (CeAlO₃), *Acta Crystallographica Section B: Structural Crystallography and Crystal Chemistry*, 24 (1968) 295-296.
- [37] A. Basrur, D. Sabde, Chapter 4 - Catalyst Synthesis and Characterization A2 - Joshi, Sunil S, in: V.V. Ranade (Ed.) *Industrial Catalytic Processes for Fine and Specialty Chemicals*, Elsevier, Amsterdam, 2016, pp. 113-186.
- [38] J.A. Anderson, M.J. Castaldi, G. Centi, J.J. Spivey, K. Dooley, *Catalysis*, Royal Society of Chemistry, 2009.
- [39] S. Dantas, K. Resende, C. Ávila-Neto, F. Noronha, J. Bueno, C. Hori, Nickel supported catalysts for hydrogen production by reforming of ethanol as addressed by in situ temperature and spatial resolved XANES analysis, *International Journal of Hydrogen Energy*, 41 (2016) 3399-3413.
- [40] H. Wang, J.T. Miller, M. Shakouri, C. Xi, T. Wu, H. Zhao, M.C. Akatay, XANES and EXAFS studies on metal nanoparticle growth and bimetallic interaction of Ni-based catalysts for CO₂ reforming of CH₄, *Catalysis Today*, 207 (2013) 3-12.

- [41] J. Juan-Juan, M. Román-Martínez, M. Illán-Gómez, Catalytic activity and characterization of Ni/Al₂O₃ and NiK/Al₂O₃ catalysts for CO₂ methane reforming, *Applied Catalysis A: General*, 264 (2004) 169-174.
- [42] M. Ferrandon, A.J. Kropf, T. Krause, Bimetallic Ni-Rh catalysts with low amounts of Rh for the steam and autothermal reforming of n-butane for fuel cell applications, *Applied Catalysis A: General*, 379 (2010) 121-128.
- [43] A.E.P. de Lima, D.C. de Oliveira, In situ XANES study of Cobalt in Co-Ce-Al catalyst applied to Steam Reforming of Ethanol reaction, *Catalysis Today*, 283 (2017) 104-109.
- [44] S. Andonova, C. De Ávila, K. Arishtirova, J. Bueno, S. Damyanova, Structure and redox properties of Co promoted Ni/Al₂O₃ catalysts for oxidative steam reforming of ethanol, *Applied Catalysis B: Environmental*, 105 (2011) 346-360.
- [45] N. Parizotto, D. Zanchet, K. Rocha, C. Marques, J. Bueno, The effects of Pt promotion on the oxo-reduction properties of alumina supported nickel catalysts for oxidative steam-reforming of methane: Temperature-resolved XAFS analysis, *Applied Catalysis A: General*, 366 (2009) 122-129.

This page intentionally left blank

CHAPTER 3: METHODOLOGY

Abstract

Outlined the experimental techniques that applied in this research such as synthesis of catalyst, APR of glycerol and characterisation approaches including physisorption, SEM, TEM, CO-TPD, XRD as well as XANES.

Chapter Contents

3.1	Synthesis of Catalyst	42
3.1.1	Impregnation Method	42
3.2	Aqueous Phase Reforming (APR) of Glycerol	43
3.2.1	Gas Chromatography (GC) of Vapour Product	44
3.2.2	High Performance Liquid Chromatography (HPLC) of Liquid Product	45
3.3	Characterisation of Catalyst.....	47
3.3.1	Surface Area and Pore Structure by Physisorption	47
3.3.2	Scanning Electron Microscope (SEM).....	48
3.3.3	Transmission Electron Microscope (TEM).....	48
3.3.4	CO - Temperature Programmed Desorption (TPD).....	48
3.3.5	X-Ray Powder Diffraction (XRD)	50
3.4	X-Ray Absorption Near Edge Spectroscopy (XANES)	51
3.5	References	53

3.1 Synthesis of Catalyst

3.1.1 Impregnation Method

Mono- and bi-metallic catalyst with various metal loading were prepared by impregnating alumina support purchased from Sigma-Aldrich A1522 with various metal precursors. Nickel (II) Nitrate Hexahydrate, $\text{Ni}(\text{NO}_3)_2 \cdot 6\text{H}_2\text{O}$ (Sigma-Aldrich 203874), Palladium (II) Nitrate, $\text{Pd}(\text{NO}_3)_2$ (Sigma-Aldrich 380040), Rhodium (III) Chloride, RhCl_3 (Sigma-Aldrich 307866) and Ruthenium (III) Chloride, RuCl_3 (Sigma-Aldrich 208523) were used as the precursor for Ni, Pd, Rh and Ru catalyst preparation respectively. Various composition of mono-metallic and bi-metallic catalyst were prepared in such that the metal to alumina support ratio of 11 wt%: 89 wt% were kept constant. Table 3.1.1-1 below shows three groups of different composition of mono-metallic and bi-metallic catalyst sample in the study.

Table 3.1.1-1: Mono- and bi- metallic catalyst sample

Ni:Pd(x:y)/Al₂O₃	Ni:Rh(x:y)/Al₂O₃	Ni:Ru(x:y)/Al₂O₃
Ni:Pd(10:1)/Al ₂ O ₃	Ni:Rh(10:1)/Al ₂ O ₃	Ni:Ru(10:1)/Al ₂ O ₃
Ni:Pd(1:1)/Al ₂ O ₃	Ni:Rh(1:1)/Al ₂ O ₃	Ni:Rh(1:1)/Al ₂ O ₃
Pd/Al ₂ O ₃	Rh/Al ₂ O ₃	Rh/Al ₂ O ₃

x:y ratio is the bi-metallic mass ratio

For synthesis of 10 g of Ni:Pd(10:1)/Al₂O₃ sample catalyst, 8.9g of alumina was impregnated with a solution prepared by dissolving desired quantities of Nickel Hexahydrate, $\text{Ni}(\text{NO}_3)_2 \cdot 6\text{H}_2\text{O}$ and Palladium (II) Nitrate, $\text{Pd}(\text{NO}_3)_2$ in 250 mL of deionised water in a beaker. Suspension was then heated and mixed with a magnetic stirrer bar at temperature of 65 °C for 6 hours on a heating plate. After 6 hours of heating, the samples were dried in an oven at 120 °C overnight and calcined under flowing air in a furnace at 500 °C for 4 hours. The remaining catalysts were prepared in a similar manner but with a different required amount of precursor with Ni:M ratio 10:1, 1:1, 0:1 (M = Pd, Rh and Ru). It should be noted that the as-synthesised impregnated catalysts typically contain NiO and metal-oxides on γ -Al₂O₃.

For the reduced catalysts, the samples were treated under flowing H₂ by heating the sample from room temperature to 400 °C (~ 1 atm pressure) and holding the temperature for 5 hrs. The reduced catalysts were stored in a nitrogen environment glove box before sample analysis.

3.2 Aqueous Phase Reforming (APR) of Glycerol

APR of 2wt % glycerol reaction was carried out in a plug flow reactor as shown in Figure 3.2-1 and schematic diagram illustrated in Figure 3.2-2.

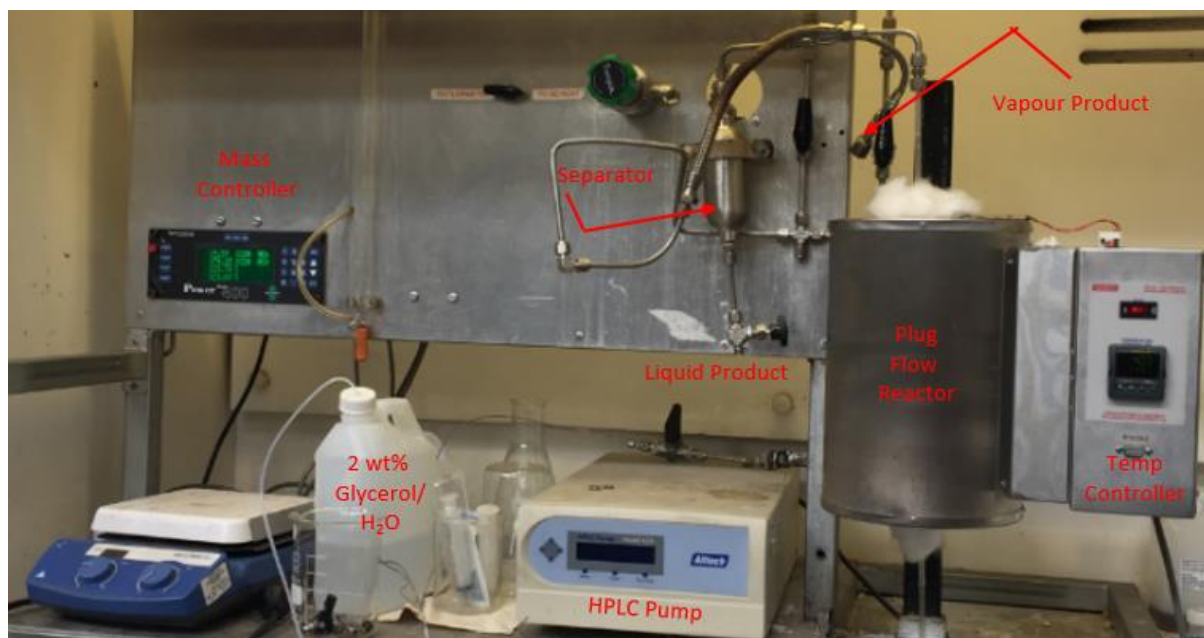


Figure 3.2-1: APR reaction set up

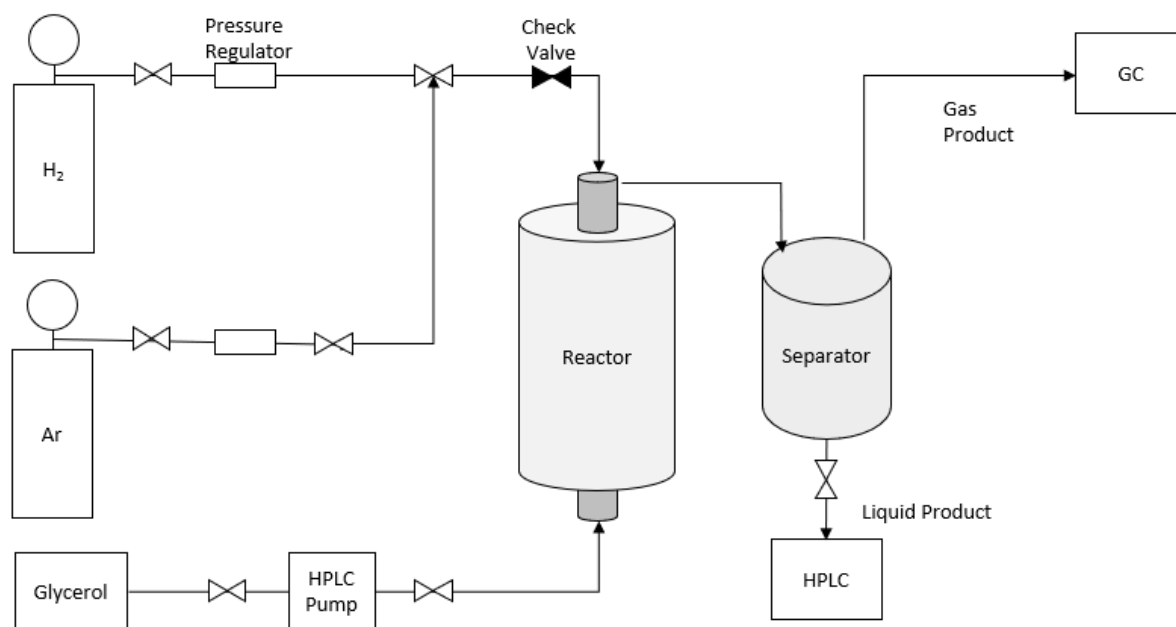


Figure 3.2-2: Schematic diagram of APR reaction set up

Approximately 1g of catalyst was loaded into a 0.5-inch stainless steel tubular reactor and held in position with quartz wool plugs. Reaction temperature was monitored by a K-type

thermocouple and it was mounted inside the reactor very close to the catalyst bed. The reactor, on the other hand, was placed in a tube furnace and the furnace temperature was controlled by the Labec temperature controller.

Prior to the activity test, the catalyst was reduced in-situ with hydrogen (10sccm) flowing through the 3-way valve into the reactor for 6 hours at 400°C and atmospheric pressure. The 3-way valve was then switched to Ar to purge the system. After purging the system with Ar and cooling down to 60°C, the backpressure regulator was set at the desired pressure (typically 425 psig), the aqueous feed solution comprising 2wt% glycerol was introduced using Alltech Model 42b HPLC digital pump at the desired feed rate (LHSV of 8.4h⁻¹). Once the liquid is introduced through the pump, it displaces the Ar gas and the reactor is now filled with liquid only. The counter-flow of Ar and liquid was set-up in such way to avoid slug flow. The check valve was also installed to stop liquid to flow back to the gas cylinder.

Then, heating of catalyst bed was initiated. When the reactor reached the desired reaction temperature, in most cases 225°C, argon flow was set as 10 sccm. The system was allowed to stabilize for about 1 hour prior to analysis of the reaction products.

3.2.1 Gas Chromatography (GC) of Vapour Product

Gas products were analysed at 20 min intervals using a gas chromatograph Shimadzu GC-2014, equipped with two molsieve 5Å columns and detectors, including the thermal conductivity detector (TCD) and flame ionization detector (FID) [1].

The TCD was used for analysis of gases such as, hydrogen, oxygen and nitrogen. In addition, the FID was used for detection of carbon dioxide, carbon monoxide and methane.

Prior to the gas analysis, the GC was calibrated using highly purity gas (grade 5.0) from Coregas. For each component calibration curves, 4~5 injections of various compositions of gas components were made to ensure consistency of data and relative standard deviation. The concentration of the gas product could then be derived based on the calibration curve obtained.

In Shimadzu Ver 3.2 software, the data collected will be interpolated against the calibration curve to determine the concentration of respective component in the gas sample. The

selectivity to H₂ can then be derived the ratio of the amount of H₂ produced divided by the amount of H₂ that could be produced if all the converted glycerol had undergone complete reforming to produce H₂ and CO and all CO shifted to CO₂. Under this definition, one mole of converted glycerol could generate 7 mol of H₂ and 3 mol of CO₂. The selectivity of the other carbon containing products refers to the percentage of carbon present in this product relative to the total carbon available based on converted glycerol [2]. Besides that, Table 3.2.1-1 below also show the formulas frequently applied to evaluate the performance of the aqueous phase reforming [3]:

Table 3.2.1-1: Parameters and formulas conventionally applied to evaluate APR performance

PARAMETER	FORMULA
Hydrogen Yield ^a	$Y_{H_2}(\%) = 100 \times \frac{mol_{out}H_2}{mol_{in}feedstock} \times \frac{1}{r}$
Hydrogen Selectivity ^a	$S_{H_2}(\%) = 100 \times \frac{mol_{out}H_2}{(mol_{in} - mol_{out})feedstock} \times \frac{1}{r}$
Hydrogen Formation Rate	$\frac{\mu mol(H_2)/min}{g(catalyst)}$
Carbon Selectivity ^b	$S_i(\%) = 100 \times \frac{C_i \text{ atom in gas product}}{C \text{ atom in gas products}}$
Carbon Yield ^c	$S_{ctoG}(\%) = 100 \times \frac{C \text{ atom in gas product}}{C \text{ atom in feedstock}}$
	$Y_{ctoL}(\%) = 100 \times \frac{C \text{ atom in liquid product}}{C \text{ atom in feedstock}}$

^a $r = H_2/CO_2$ (stoichiometry reforming ratio)

^b Carbon to gases

^c Carbon to liquids

3.2.2 High Performance Liquid Chromatography (HPLC) of Liquid Product

The liquid products were collected in a condenser downstream of the reactor bed as shown in Figure 3.2-1 and to be analysed with the Agilent Technologies 1260 Infinity high performance liquid chromatogram (HPLC) [4].

The complete Agilent Technologies 1260 Infinity system includes the following [4]:

- Agilent 1260 Infinity degasser reduced the baseline noise due to high degassing capacity.
- Agilent 1260 Infinity isocratic pump for flow precision < 0.1% RSD.
- Agilent 1260 Infinity auto sampler with single valve design.

- Agilent 1260 Infinity thermostated column.
- Agilent 1260 Infinity Refractive Index Detector (RID) with an automatic recycle valve.

Prior to the liquid sample analysis, various composition of glycerol standard solutions, including, 0 wt%, 0.01 wt%, 0.25 wt%, 0.05 wt%, 0.1 wt%, 0.5 wt%, 1wt%, 2.5 wt%, 5 wt%, 10 wt%, 20 wt% and 30 wt% were prepared and measured to generate a glycerol calibration curve as illustrated in Figure 3.2.2-1.

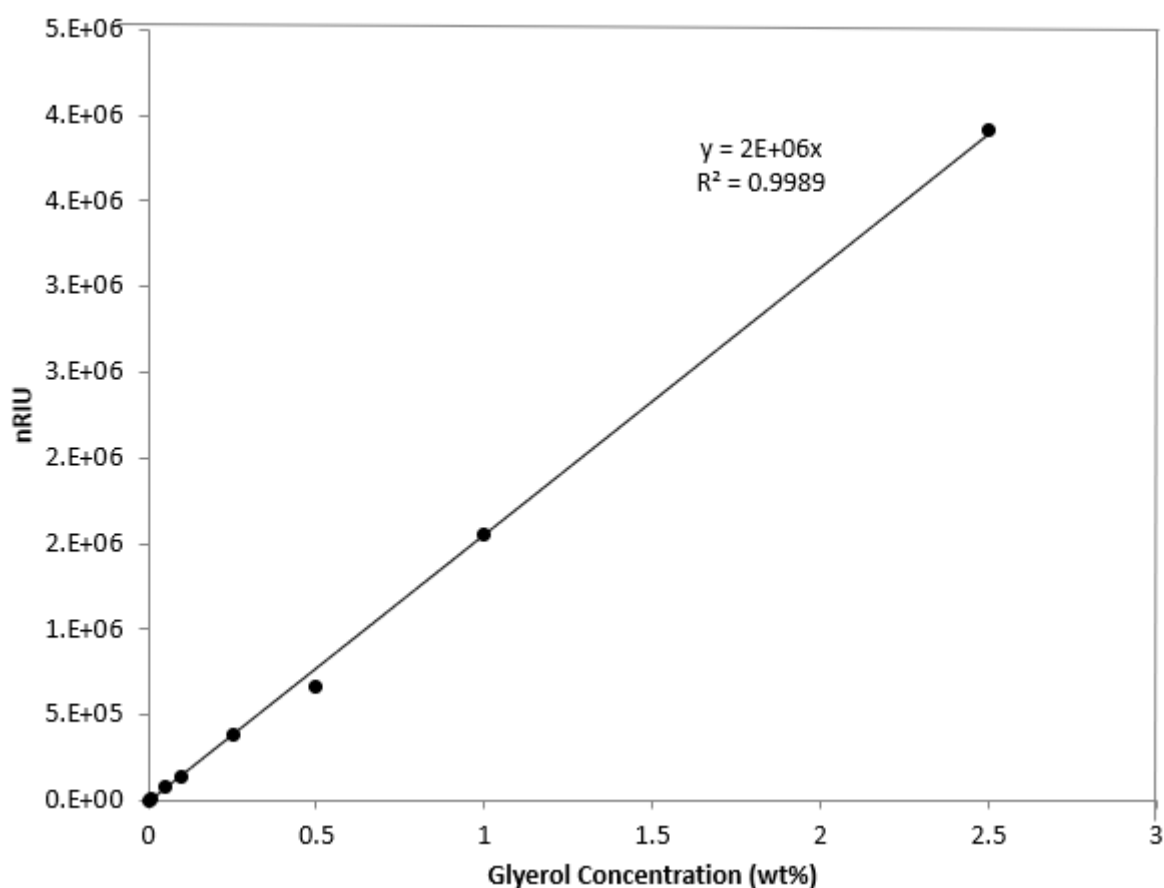


Figure 3.2.2-1: Glycerol calibration curve on HPLC

In the Agilent GPC software, the data collected will be interpolated against the glycerol calibration curve to determine the glycerol concentration reacted and fed. The glycerol conversion can then be derived from the glycerol concentration with the following formula [5]:

$$\text{Conversion} = \frac{\text{Concentration Glycerol Reacted (moles)}}{\text{Concentration Glycerol Fed (moles)}} \times 100 \text{ (Equation 3.2.2 - 1)}$$

An example of liquid product consist of 1 wt% of unreacted glycerol is shown in Figure 3.2.2-2 below.

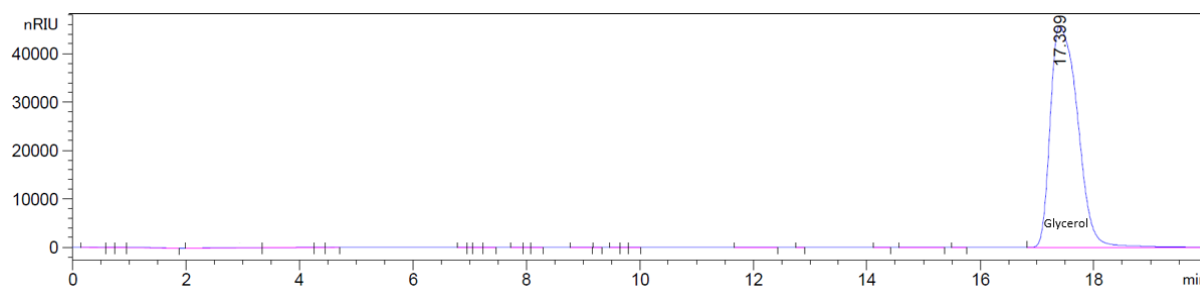


Figure 3.2.2-2: 1wt % of unreacted glycerol in liquid product

3.3 Characterisation of Catalyst

3.3.1 Surface Area and Pore Structure by Physisorption

The surface properties and pore structure of the catalyst were measured by N₂ adsorption-desorption at liquid nitrogen temperature (~ 77 K) using the Micrometrics ASAP 2020 with the association of Data Master [6].

Prior to the measurement, several sample preparation steps were required, including: the empty sample tube, firt, lid and sample were weighed using a weighing balance, samples were degassed at 200 °C for 3 hours to remove physically adsorbed components, the samples' weight after degassed were again measured. In the meantime, liquid nitrogen were transferred to the analysing port. The sample was then fixed onto the analysing port and ready to be analysed.

Micrometrics ASAP 2020 was operated in the automation mode in which the volume of absorbed N₂ at relative pressure (0-1 atm) was plotted to a close isothermal curve consisting both adsorption and desorption data. Brunauer-Emmett-Teller (BET) and Barret-Joynew-Halenda (BJH) were used to analysed the specific surface area and characterisation of pore structure, such as, total pore volume and pore sized distribution respectively [7] [8]. Specific surface area was determined from the linear portion of the BET plot and pore volume was calculated from the desorption branch of N₂ physisorption isotherm. Besides that, the pore size distribution was calculated from the desorption isotherm using Barrett-Joyner-Halenda (BJH).

3.3.2 Scanning Electron Microscope (SEM)

FEI Nova Nano SEM 450 field emission scanning electron microscope was used to analyse the morphology of the sample surface [9].

It has an energy variable beam landing from 30 kV to 0.05 kV and beam deceleration allowing stage bias from +50 V to – 4000 V. The Nova is also equipped with a Schottky FEG (S-FEG) that combines field emission and thermal emission (1800 K).

3.3.3 Transmission Electron Microscope (TEM)

FEI Tecnai G² T20 Transmission Electron Microscope was used to perform conventional imaging, diffraction and microanalysis work, particularly the insight of the inner pore structure and metal distribution of the sample catalyst [10].

It was operated at 200 kV accelerating voltage and equipped with a lanthanum hexaboride (LaB₆) thermal emitter with FEI Tecnai “Twin” lens type as well as spherical aberration coefficient of $C_s = 2.2$ mm permits at point of resolution of 2.7 Å.

3.3.4 CO - Temperature Programmed Desorption (TPD)

CO-TPD was carried out to analyse the interaction between Ni-noble metal and to measure the strength as well as the number of metal active sites available on the catalyst surface. The custom-build instrument as illustrated in Figure 3.3.4-1 will be used in this investigation.



Figure 3.3.4-1: CO-Temperature Programmed Desorption set up

The reactor was mounted with a temperature controller and connected to a Stanford Research Systems (SRS) Residual Gas Analyser (RGA) 300 and Brooks 0254 Mass Flow Controller as well as a vacuum system [11] [12]. For this technique, 10 vol% CO/Ar, H₂ and Argon gas cylinder were connected to the reactor.

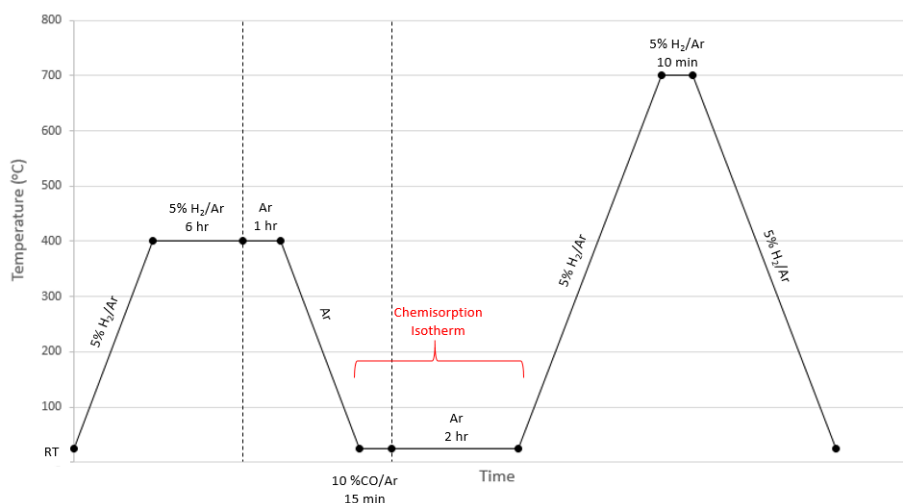


Figure 3.3.4-2: Temperature and gas flow profile of CO Chemisorption

As shown in Figure 3.3.4-2, about 0.5g catalyst sample charged into a glass tube was first reduced under 50 mLmin⁻¹ H₂ condition at 400 °C for 6 hours and then purge with inert argon gas for about 1 hour at 400 °C. After purging, the system was allowed to cool down to room temperature under Ar gas. To dope the catalyst surface with CO, the catalyst surface was introduced with 10% CO/Ar gas mixture for 15 min at a flowrate of 100 mLmin⁻¹ followed by purging with Ar gas at 100 mLmin⁻¹ for 2 hours to remove any excess CO such that only a monolayer CO adsorbed was left on the surface of the catalyst. The partial pressure of the system was then monitored by the RGA, Ar flow was subsequently reduced to 50 mLmin⁻¹ and the TPD data were recorded as the sample was heated from room temperature to 800 °C at 10 °Cmin⁻¹. Typical CO-TPD products include CO and CO₂.

During analysis, two desorption peaks were observed: the first corresponded to the weakly bonded adsorbates require less heat to break their substrate-adsorbate bonds and they desorb at a low temperature while the second corresponded to more strongly bonded adsorbates which require more energy to break their bond and thus they desorb at a higher temperature [13]. Therefore, only strongly CO bonded was considered, the area under the peak is proportional to the amount adsorbed, i.e. proportional to the surface coverage. The

surface coverage would then be compared to the calibration data obtained to obtain the dispersion, M or fraction exposed of a metal catalyst [14].

The dispersion, M or fraction exposed of a metal catalyst is also defined as the ratio of the monolayer chemisorption, N_{MS} to the total number of metal atoms, N_{Mt} [15]:

$$M = \frac{N_{MS}}{N_{Mt}} \text{ (Equation 3.3.4 – 1)}$$

3.3.5 X-Ray Powder Diffraction (XRD)

The crystalline structure and diffraction patterns of the samples were obtained on a Rigaku Mini Flex 600 X-Ray Diffraction instrument [16]. The instrument was operated at 40 kV and 15 mA with Cu K_{α} monochromatized radiation with wavelength, $\lambda = 0.154505$ nm. Scans were recorded over the range of 2θ from $10^{\circ} - 90^{\circ}$ in step size of 0.02° .

With the diffraction data collected, the average crystal size of the particles were then estimated using the Scherrer equation [17]:

$$D_{particle} = \frac{\lambda K}{\beta \cos \theta} \text{ (Equation 3.3.5 – 1)}$$

In Equation 3.3.5-1 above, K referred to shape factor, usually taken as 0.89, λ is the wavelength used in this case Cu K_{α} monochromatized radiation and equal to 0.154505 nm. β is the line broadening at half the maximum intensity, also known as the full width at half maximum (FWHM) in radians and θ is the Bragg angle.

With the average crystal particle size obtained, the particle dispersion can also be estimated in the following equation [18]:

$$Dispersion_{particle} = \frac{6V_{particle}}{D_{particle}A_{particle}} \text{ (Equation 3.3.5 – 2)}$$

In Equation 3.3.5-2, $V_{particle}$ is the single atomic volume, $D_{particle}$ referred to the crystallite particle size and $A_{particle}$ is the surface area of a single atom.

3.4 X-Ray Absorption Near Edge Spectroscopy (XANES)

XAFS experiments were measured with the XAFS beamline at Australian Synchrotron, Victoria, Australia with a photon delivery system as tabulated in Table 3.4-1 [19].

Table 3.4-1: Photon Delivery System of XAFS

PARAMETER	SPECIFICATION
Source	1.9T Wiggler
Available energy range	5 – 31 keV
Optimal energy range	Mode 1: 5 – 9 keV using Si (111) Mode 2: 8.5 - 18.5 keV using Si (111) Mode 3: 15 – 31 keV using Si(311)
Resolution $\Delta E/E$	Crystal Dependent: $\sim 1.5 \times 10^{-4}$ using Si(111) $\sim 0.4 \times 10^{-4}$ using Si(311)
Nominal beam size at sample	~ 0.25 by 0.25 mm fully focussed
Photon flux at sample	10^{10} to 10^{12} ph/s using Si(111) 10^9 to 10^{11} ph/s using Si(311)
Harmonic content at 5 – 18 keV	$< 10^{-5}$

Measurements were obtained using beamline monochromatized by a Si (311) channel-cut monochromators. For all measurements, the X-ray ring operated at energy of 3 GeV and at designed beam current of 200 mA.

All X-ray absorption spectra were carried out in the cryostat condition using fluorescence detection configuration at the Pd-K, Rh-K and Ru-K edges with 24350 eV, 22117 eV and 232200 eV respectively in mode 3 (15 – 31 keV). Apertures of 0.5 mm X 8 mm were positioned in front of the first detector (I_0), in front of the catalyst sample and in front of the second detector (I).

For the Pd-K edge scans, a 4 μ m thick Pd foil placed between the ionization chamber was used to calibrate the monochromators. Measurement obtained with the other reference compounds and catalyst sample were then reference to this calibration. Similarly, Rh and Ru foils will be used as references for Rh and Ru catalyst, respectively.

The as-synthesised impregnated catalysts typically contained NiO and M-oxides on γ - alumina. To reduce the NiO and M-oxides to Ni⁰ and M⁰ state, the catalyst will be reduced ex-situ under flowing 5% H₂/Ar gas mixture by heating the sample from room temperature to 400 °C at 1 atm pressure and holding temperature for 5 hours. The reduced catalysts were stored in a

nitrogen environment glove box before sample analysis. The as-synthesised and nitrogen-sealed reduced catalyst samples stored in the glass container were transported to the Australian Synchrotron at Melbourne, Victoria for measurement of the x-ray absorption.

Each catalyst will be scanned as-synthesis and after reduction procedure. Prior to the measurement, as-synthesised and reduced catalyst then be pelletized into a 7.5 mm pellet and then pressed into a cryostat sample holder that will be mounted in a cell designated for ex-situ XAS analysis. The sample holder was aligned with the centre axis such that all of the X-ray photon passed through a catalyst bed of relatively uniform thickness.

The sample weight required had been calculated based upon Δ edge step and assuming $\mu_0 = 1.5$. A summary of analysed samples are tabulated in Table 3.4-2.

Table 3.4-2: Sample to be analysed at Mode 3 using Si (311)

SAMPLE	SAMPLE SIZE (mg)	E (eV)
Ni:Pd(10:1)/Al ₂ O ₃	607.512	24400
Ni:Pd(1:1)/Al ₂ O ₃	382.197	
Pd/Al ₂ O ₃	265.986	
Ni:Rh(10:1)/Al ₂ O ₃	526.675	23270
Ni:Rh(1:1)/Al ₂ O ₃	344.901	
Rh/Al ₂ O ₃	240.224	
Ni:Ru(10:1)/Al ₂ O ₃	464.779	22167
Ni:Ru(1:1)/Al ₂ O ₃	317.006	
Ru/Al ₂ O ₃	224.780	

All raw data collected were automatically saved in a binary *.mda* format, which require conversion into Ascii format prior to analysis by using the MDA Display program.

The ATHENA software from the IFEFFIT package (version 1.2.11d) was used for background removal (AUTOBK algorithm), post-edge normalisation and XAFS data analysis [19]. The XANES normalised data obtained were then compared against the reference Pd, Rh, Ru foil and PdO, Rh₂O₃ as well as RuO₂ which represent different oxidation state of Pd(0), Rh(0), Ru(0), Pd(II), Rh(III) and Ru(IV), respectively.

3.5 References

- [1] Shidmazu, Capillary and Packed Gas Chromatograph, in, 2014.
- [2] D.L. King, L. Zhang, G. Xia, A.M. Karim, D.J. Heldebrant, X. Wang, T. Peterson, Y. Wang, Aqueous phase reforming of glycerol for hydrogen production over Pt–Re supported on carbon, *Applied Catalysis B: Environmental*, 99 (2010) 206-213.
- [3] I. Coronado, M. Stekrova, M. Reinikainen, P. Simell, L. Lefferts, J. Lehtonen, A review of catalytic aqueous-phase reforming of oxygenated hydrocarbons derived from biorefinery water fractions, *International Journal of Hydrogen Energy*, 41 (2016) 11003-11032.
- [4] Agilent, Agilent 1260 Infinity GPC/SEC System, in, 2012.
- [5] F. Bastan, M. Kazemeini, A.S. Larimi, Aqueous-phase reforming of glycerol for production of alkanes over Ni/CexZr1-xO2 nano-catalyst: Effects of the support's composition, *Renewable Energy*, 108 (2017) 417-424.
- [6] Micrometrics, Micrometrics Introduce the ASAP 2020, in, 2014.
- [7] S. Brunauer, P.H. Emmett, E. Teller, Adsorption of gases in multimolecular layers, *J. Am. Chem. Soc.*, 60 (1938) 309-319.
- [8] E.P. Barrett, L.G. Joyner, P.P. Halenda, The determination of pore volume and area distributions in porous substances. I. Computations from nitrogen isotherms, *J. Am. chem. soc.*, 73 (1951) 373-380.
- [9] F. NovaNanoSEM, Science Dual Life, in.
- [10] MCEM, FEI Tecnai G2 F20 Transmission Electron Microscope, in.
- [11] SRS, Residual Gas Analysers, in, 2009.
- [12] Brooks, Four Channel Power Supply, Readout and Set Point Controller in, 2010.
- [13] R. Grimm, Temperature Programmed Desorption Overview, in, Worcester Polytechnic Institute, 2016.

- [14] X. Shen, L.-J. Garces, Y. Ding, K. Laubernds, R.P. Zerger, M. Aindow, E.J. Neth, S.L. Suib, Behavior of H₂ chemisorption on Ru/TiO₂ surface and its application in evaluation of Ru particle sizes compared with TEM and XRD analyses, *Applied Catalysis A: General*, 335 (2008) 187-195.
- [15] M.A. Vannice, *Kinetics of Catalytic Reactions*, Springer Science, United States of America, 2005.
- [16] Rigaku, Rigaku introduces new 5th generation MiniFlex benchtop X-Ray Diffraction (XRD) instrument, in, 2012.
- [17] A. Morato, V. Rives, Comments on the application of the Scherrer equation in “Copper aluminum mixed oxide (CuAl MO) catalyst: A green approach for the one-pot synthesis of imines under solvent-free conditions”, by Suib et al. [*Appl. Catal. B: Environ*, 188 (2016) 227–234, doi:10.1016/j.apcatb.2016.02.007], *Applied Catalysis B: Environmental*, 202 (2017) 418-419.
- [18] J.R. Anderson, *Structure of metallic catalysts*, Academic Press, ix+ 469, 24 x 16 cm, illustrated(↔) 16. 50, (1975).
- [19] AustralianSynchrotron, *Beam Lines*, in, Ansto, Victoria, Australia, 2014.

This page intentionally left blank

CHAPTER 4: APR OF GLYCEROL WITH NOBLE METAL - NICKEL BASED CATALYST SUPPORTED ON ALUMINA

Abstract

Described the effect of Pd, Rh and Ru addition to Ni catalyst on the APR of glycerol. Catalysts were characterised and tested in a continuous plug flow reactor. It was clear that adding noble metal to Ni impacted the catalytic activity of the catalyst. The effects will also be analysed with other various characterization techniques, including physisorption, CO-TPD, SEM and XRD.

Chapter Contents

4.1	Results and Discussions	57
4.1.1	Catalyst Characterisation.....	57
4.1.2	APR Activity.....	62
4.2	Conclusion.....	65
4.3	References	66

4.1 Results and Discussions

4.1.1 Catalyst Characterisation

The textural properties of fresh catalysts are summarized in Table 4.1.1-1. The surface area, A_{BET} , pore volume, V_p and pore diameter, D_p generally decrease with the addition of Ni to monometallic catalyst, $M/\text{Al}_2\text{O}_3$ (where $M=\text{Pd}$, Rh or Ru). As Ni in the bi-metallic catalyst increases from (Ni:M where $M=\text{Pd}$, Rh or Ru) 1:1 wt% to 10:1 wt%, the surface area, pore volume and pore diameter decrease. However, bi-metallic catalyst Ni:Pd/ Al_2O_3 did not obey this trend where surface area of Ni:Pd(10:1)/ Al_2O_3 is greater than that of Ni:Pd(1:1)/ Al_2O_3 . This has also encourages the WGS reaction of Ni:Pd(10:1)/ Al_2O_3 in APR reaction.

Addition of noble metal such as Pd and Ru to Ni/ Al_2O_3 results in increase in rate of CO/ CO_2 desorption, CO-TPD and active metal sites, M of the bi-metallic catalytic system, resulting the higher overall rate of H_2 production. This could be results of several factors including:

- (i) Ni-M particles are smaller
- (ii) Ni-M increased the reducibility of Ni by forming an alloy. Alloying of Ni-M decreased the CO binding energy on the active metal site increased the fraction of active site available for the reforming reaction [1].
- (iii) Ni-M(oxide) locates preferentially at the particle surface where M is Pd, Rh and Ru [2].

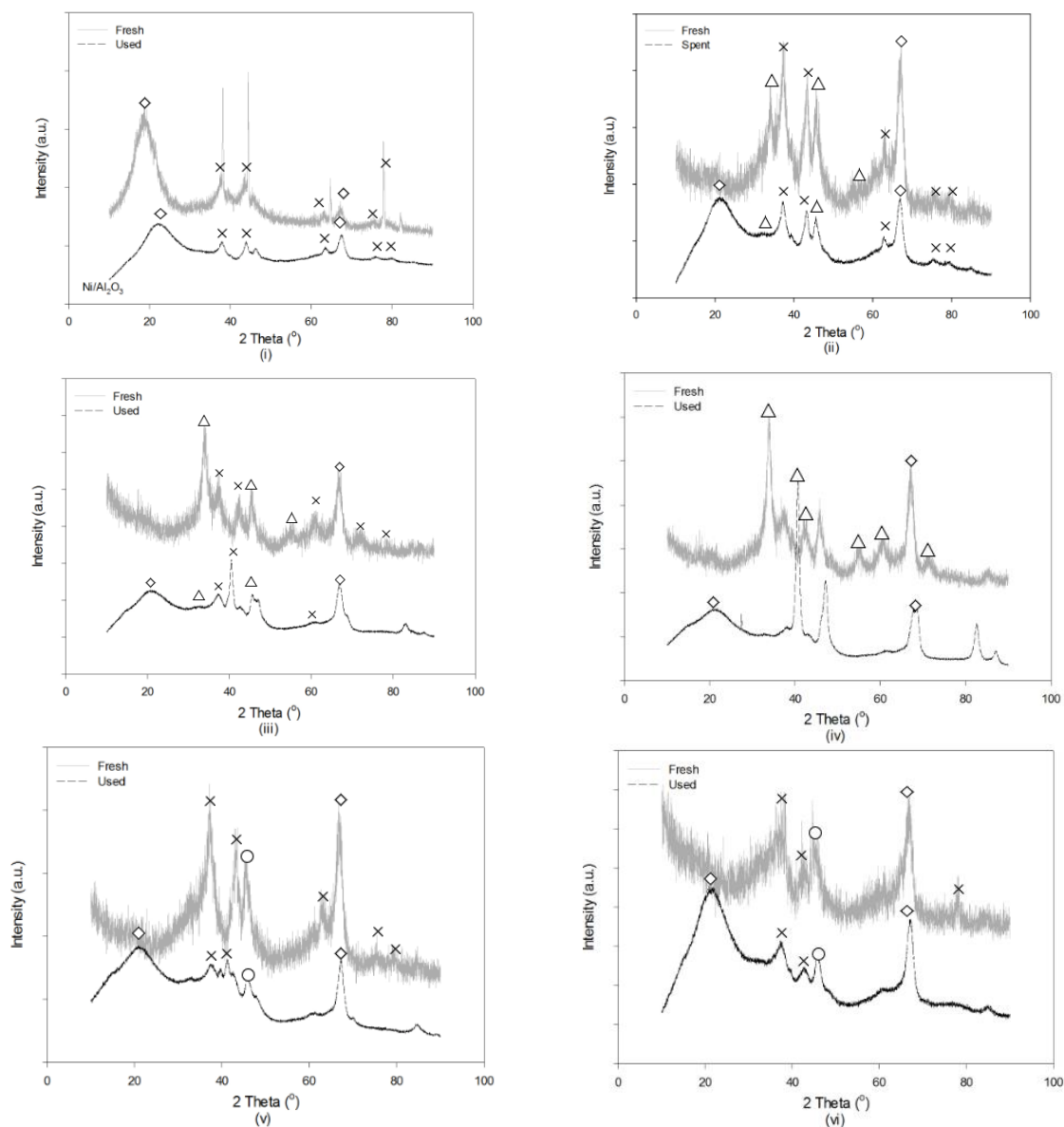
However, Ni:Rh(10:1)/ Al_2O_3 and Ni:Rh(1:1)/ Al_2O_3 catalysts did not exhibit the similar trend as that of Pd and Ru series catalysts.

Table 4.1.1-1: Textual properties of the alumina supported mono- and bi-metallic catalysts

Catalyst	A_{BET}^a	V_p^b	D_p^c	CO-TPD ^d	M^e
Ni/ Al_2O_3	91.20	0.20	6.02	84.32	4.50
Ni:Pd(10:1)/ Al_2O_3	93.48	0.21	6.26	133.48	7.42
Ni:Pd(1:1)/ Al_2O_3	90.86	0.22	6.48	199.64	13.73
Pd/ Al_2O_3	102.95	0.25	7.13	90.28	8.73
Ni:Rh(10:1)/ Al_2O_3	85.81	0.20	6.38	50.57	3.44
Ni:Rh(1:1)/ Al_2O_3	96.22	0.20	6.26	11.77	0.65
Rh/ Al_2O_3	107.47	0.23	7.02	160.19	14.99
Ni:Ru(10:1)/ Al_2O_3	85.89	0.21	6.75	129.63	7.19
Ni:Ru(1:1)/ Al_2O_3	91.97	0.24	7.41	72.84	4.92
Ru/ Al_2O_3	91.47	0.25	7.92	103.76	9.53

- ^a BET Surface Area (m^2g^{-1})
- ^b BET Total Pore Volume (cm^3g^{-1})
- ^c BET Mean Pore Diameter (nm)
- ^d Rate of CO and CO₂ Desorption ($\mu\text{molg}_{\text{cat}}^{-1}$)
- ^e Metal Dispersion (%)

For physisorption isotherms of each catalyst can be obtained in Appendix Figure A.1.1-1. Figure 4.1.1-1 shows the XRD of the fresh and used catalyst series after aqueous phase reforming reaction.



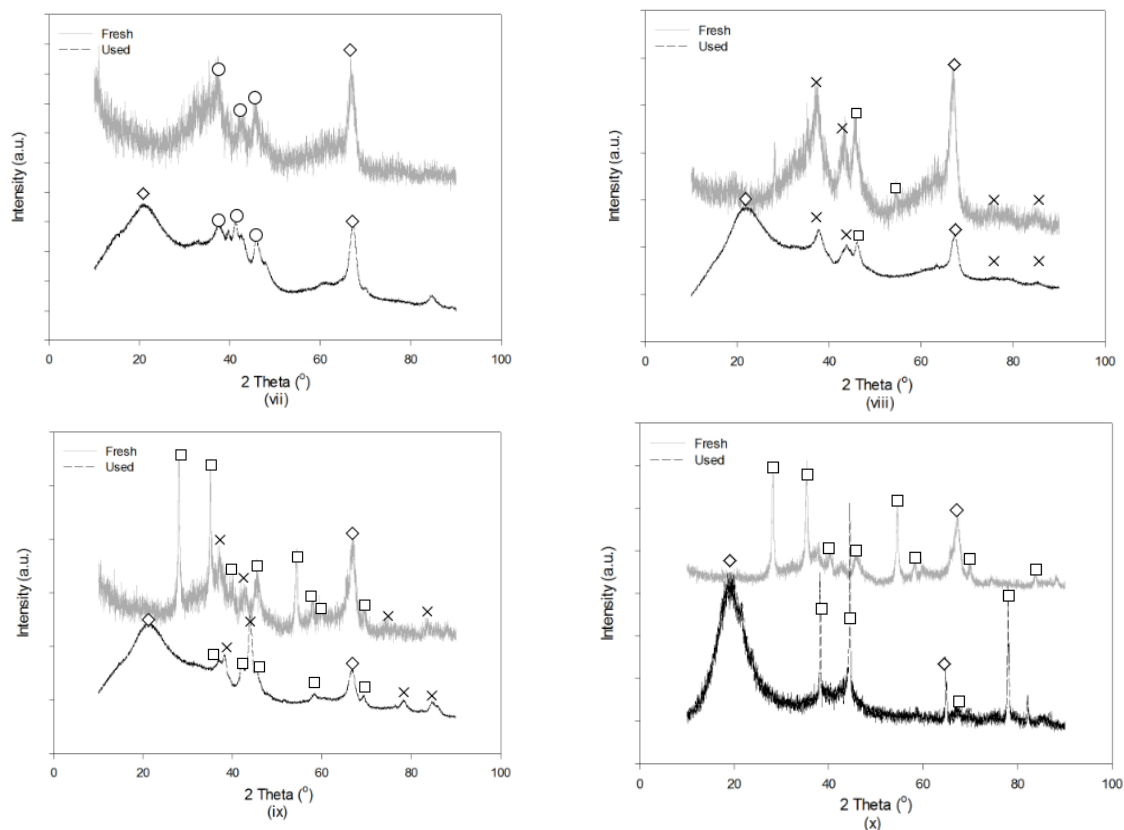


Figure 4.1.1-1: XRD patterns of fresh and used alumina supported (i) Ni/Al₂O₃ (ii) Ni:Pd(10:1)/Al₂O₃ (iii) Ni:Pd(1:1)/Al₂O₃ (iv) Pd/Al₂O₃ (v) Ni:Rh(10:1)/Al₂O₃ (vi) Ni:Rh(1:1)/Al₂O₃ (vii) Rh/Al₂O₃ (viii) Ni:Ru(10:1)/Al₂O₃ (ix) Ni:Ru(1:1)/Al₂O₃ (x) Ru/Al₂O₃ ◇ denotes alumina, X denotes Ni Oxide, Δ denotes Pd oxide, O denotes Rh oxide and □ denotes Ru oxide

In Figure 4.1.1-1 (i) of Ni/Al₂O₃ sample, peaks related to NiO at about 2 θ =37°, 43°, 63°, 75° and 79° corresponding to crystal plane (111), (200), (220), (311) and (222) respectively [3]. In Ni:Pd(1:1)/Al₂O₃ calcined samples, the peak related to NiO (220) and (311) were shifted 3° lower than the standard peak. In calcined Ni:Rh(1:1)/Al₂O₃, the peak related to NiO (111), (200) and (222) were shifted 1° lower as compared to standard peak [3]. Calcined Ni:Ru(10:1)/Al₂O₃ and Ni:Ru(1:1)/Al₂O₃ exhibited peak related to NiO (311) and (222) shifted at about 2° higher as compared to the standard NiO [3].

In monometallic Pd/Al₂O₃, peaks related to PdO were at about 2 θ =34°, 42°, 54°, 60.3° and 71.7°. Alloy effects were observed on bimetallic Ni:Pd(10:1)/Al₂O₃ and Ni:Pd(1:1)/Al₂O₃ where the peak corresponding to PdO shifted from 42° to 45° and 54° to 55° as compared to monometallic Pd/Al₂O₃ [4]. The shift in XRD peaks also indicates lattice parameter changes which imply electronic effects that promotes C-C cleavage over C-O cleavage. However, there were no peak shift in Rhodium oxide nor Ruthenium oxide observed in bimetallic Ni:Rh(x:y)/Al₂O₃ and Ni:Ru(x:y)/Al₂O₃ respectively as compared to standard samples. This may indicate that Rh and Ru were phase segregated without being in close contact with Ni [5].

The average crystallite size of NiO was determined using the Scherrer equation corresponding to Table 4.1.1-2. The interaction between Ni and alumina was further strengthened through the addition of a secondary metal species. Thus, the stronger interaction between bimetallic species and support resulting in smaller NiO size.

Table 4.1.1-2: XRD of samples

Catalyst	NiO Crystallite Size (nm)
Ni/Al ₂ O ₃	6.25
Ni:Pd(10:1)/Al ₂ O ₃	5.26
Ni:Rh(10:1)/Al ₂ O ₃	2.52
Ni:Ru(10:1)/Al ₂ O ₃	1.91

After APR reaction, peaks of alumina oxide in spent Pd/Al₂O₃ and Ru/Al₂O₃ shift towards a higher diffraction angle. This may be due to the change in lattice parameter of alumina oxide during the APR reaction [1]. The PdO peaks in used Pd/Al₂O₃ catalyst also shifted towards a higher diffraction angle after the reaction and it could be also due to the similar reason where the change in the lattice parameter of PdO during APR. In addition, RuO peaks on the used Ru/Al₂O₃ catalyst are more crystalline compared to the fresh sample because at the reaction temperature Ru mono-metallic sample is slightly sintered as compared to the bi-metallic catalyst [1]. This can be also observed in the TEM images as shown in Figure 4.1.1-2 that the tendency of sintering in Ru/Al₂O₃ catalyst. Noticeably, Ru particles showed significant aggregation from the fresh sample 44nm to about 83.3nm after APR reactions. This clearly showed that the metallic Ru species was less stable in APR reactions.

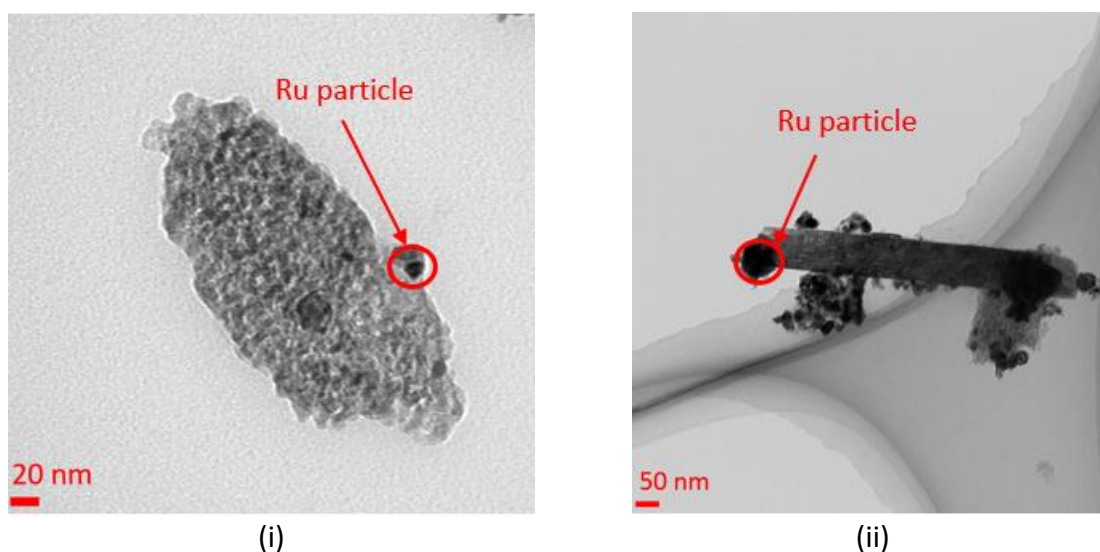


Figure 4.1.1-2: TEM Images of (i) Fresh and (ii) Used Ru/Al₂O₃

With the TEM images shown in Figure 4.1.1-3 (v), monometallic Rh/Al₂O₃ depicted the formation of coke in APR reaction which might hindered the production of hydrogen. In comparison with bimetallic catalyst, bimetallic Ni:Rh(1:1)/Al₂O₃ catalysts showed higher stability and inhibited carbon formation in the APR of glycerol.

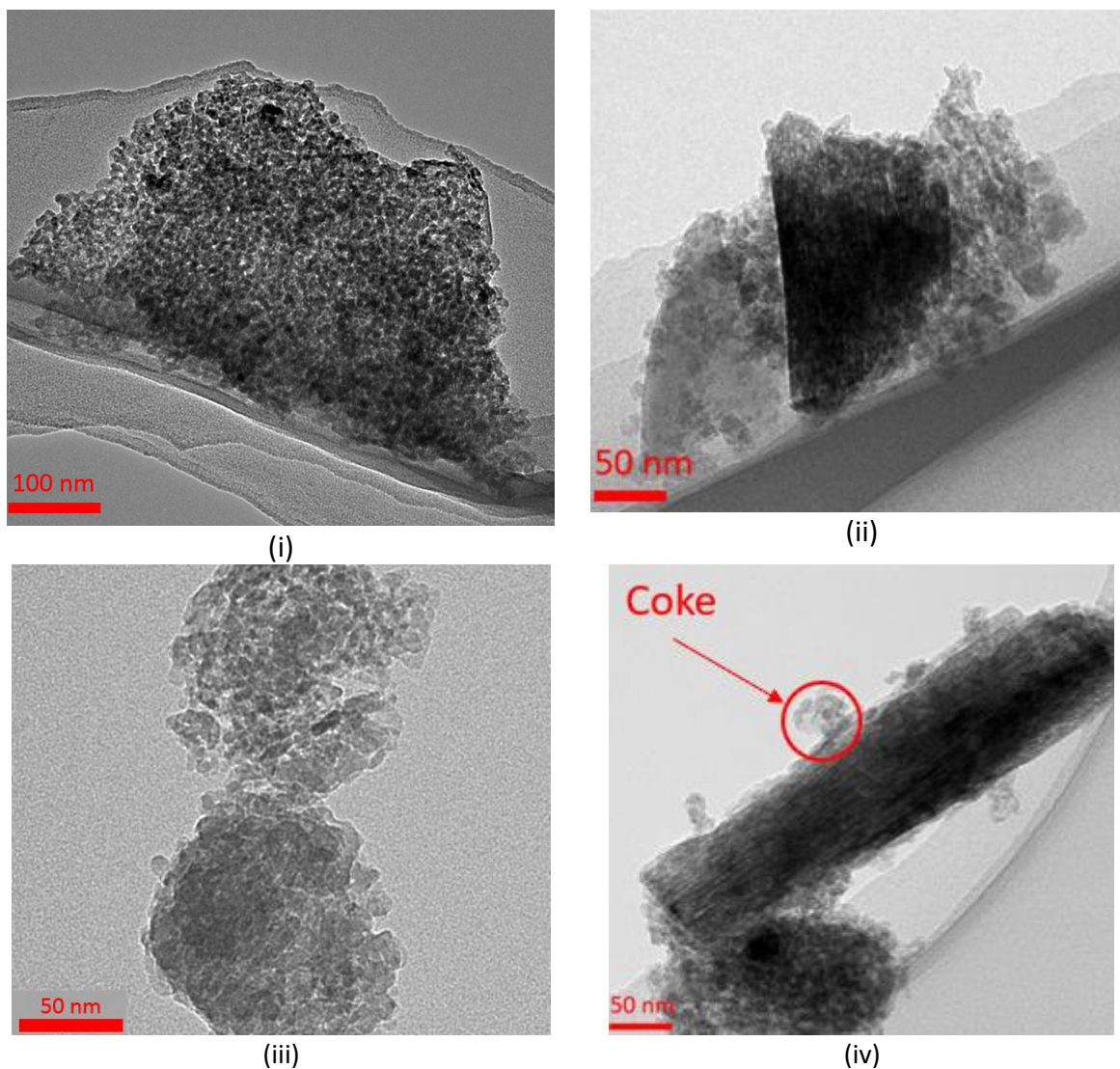


Figure 4.1.1-3: TEM Images of (i) Fresh and (ii) Used Ni: Rh (1:1)/Al₂O₃, (iii) Fresh and (iv) Used Rh/Al₂O₃

4.1.2 APR Activity

The rate of production (mmol/h.g) and liquid glycerol conversion (%) shown in Figure 4.1.2-1 were based on 4 average catalytic test runs of respective samples including Ni/Al₂O₃, Ni:Pd(10:1)/Al₂O₃, Ni:Pd(1:1)/Al₂O₃, Pd/Al₂O₃, Ni:Rh(10:1)/Al₂O₃, Ni:Rh(1:1)/Al₂O₃, Rh/Al₂O₃, Ni:Ru(10:1)/Al₂O₃, Ni:Ru(1:1)/Al₂O₃ and Ru/Al₂O₃.

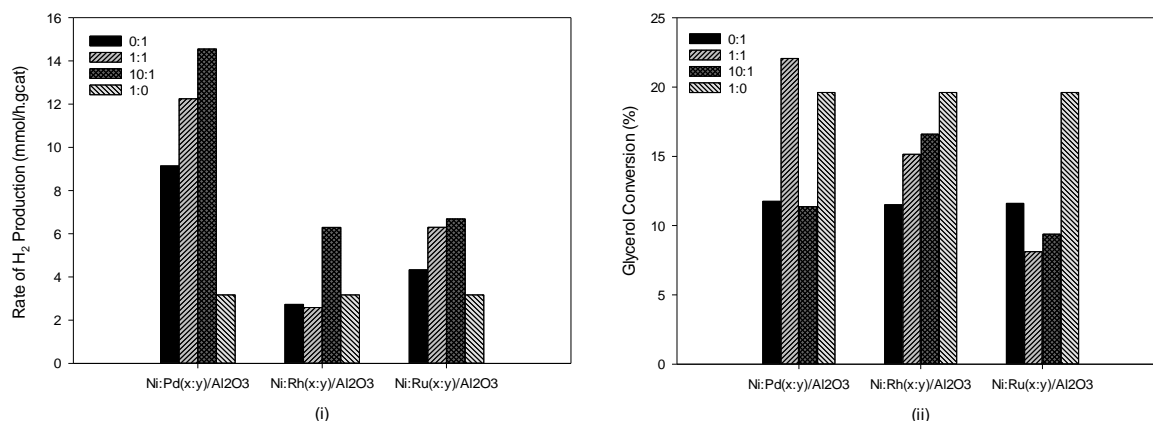


Figure 4.1.2-1: (i) Rate of hydrogen gas production and (ii) liquid glycerol conversion

It can be seen from Figure 4.1.2-1 (i) that the Ni:Pd(x:y)/Al₂O₃ overall rate of hydrogen production decreased in the following order: Ni:Pd(10:1)/Al₂O₃ > Ni:Pd(1:1)/Al₂O₃ > Pd/Al₂O₃ > Ni/Al₂O₃ and Ni:Rh(x:y)/Al₂O₃ decreased in the following order: Ni:Rh(10:1)/Al₂O₃ > Ni/Al₂O₃ > Rh/Al₂O₃ > Ni:Rh(1:1)/Al₂O₃ while Ni:Ru(x:y)/Al₂O₃ catalyst decreased in the following order: Ni:Ru(10:1)/Al₂O₃ > Ni:Ru(1:1)/Al₂O₃ > Ru/Al₂O₃ > Ni/Al₂O₃.

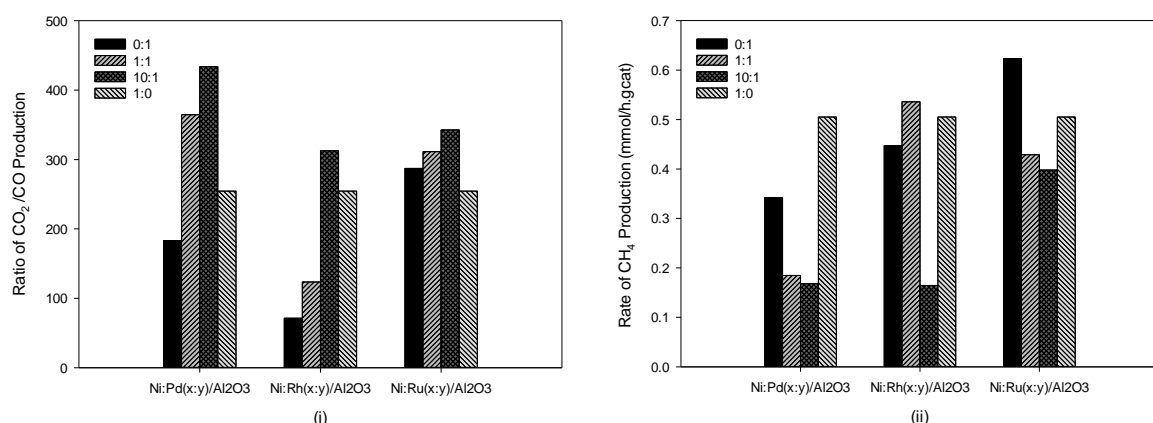


Figure 4.1.2-2: (i) Ratio of CO₂/CO gas production (WGS reaction) and (ii) rate of CH₄ production (methanation reaction)

Other gaseous product including CO₂, CO and CH₄ from the APR of glycerol are identify in Appendix Figure A.2.2-1 and Figure 4.1.2-2 (ii) respectively. The ratio of CO₂/CO production

rate is also illustrated in Figure 4.1.2-2(i). In Pd, Rh and Ru series respectively, the overall rate of CO₂/CO production decreased in the following order: Ni:Pd(10:1)/Al₂O₃ > Ni:Pd(1:1)/Al₂O₃ > Ni/Al₂O₃ > Pd/Al₂O₃ ; Ni:Rh(10:1)/Al₂O₃ > Ni/Al₂O₃ > Ni:Rh(1:1)/Al₂O₃ > Rh/Al₂O₃ and Ni:Ru(10:1)/Al₂O₃ > Ni:Ru(1:1)/Al₂O₃ > Ru/Al₂O₃ > Ni/Al₂O₃. Among the bimetallic samples, the fraction of CO₂/CO increases with the noble metal loading in the bimetallic samples, indicating the favour of WGS reaction.

Moreover, introduction of promoting metal to Ni catalyst decreases CH₄ production, indicating it does not favour methanation reaction. The Ni:Pd(x:y)/Al₂O₃ overall rate of methane production decreased in the following order: Ni > Pd > Ni:Pd(1:1)/Al₂O₃ > Ni:Pd(10:1)/Al₂O₃ and Ni:Rh(x:y)/Al₂O₃ decreased in the following order: Ni:Rh(1:1)/Al₂O₃ > Ni > Rh Ni:Rh(10:1)/Al₂O₃ while Ni:Ru(x:y)/Al₂O₃ catalyst decreased in the following order: Ru > Ni > Ni:Ru(1:1)/Al₂O₃ > Ni:Ru(10:1)/Al₂O₃.

Therefore, it could be deduced that introduction of noble metal to Ni catalytic system enhanced the rate of hydrogen production and this could be due to (i) the alter of electronic structure of Ni catalysts affecting its metal dispersion. As shown in Table 4.1.1-1, the Ni monometallic catalyst exhibited the lowest active metal active sites as compared to the M-Ni bimetallic catalyst [2]. (ii) More of the CO is getting converted into CO₂ via WGS reaction. The WGS reaction is favoured over methanation reaction which makes it more favourable for H₂ production and hence yield of hydrogen increases. This was indicated in Appendix Figure A.1.2-1(i) no observed CO₂ desorption peak on Ni/Al₂O₃ catalyst and high fraction of CO₂/CO production with bimetallic samples as compared to Ni monometallic as shown in Figure 4.1.2-2 (i).

It was also reported that Ni bi-metallic catalyst with metal loading of 10:1, such as Ni:Pd(10:1)/Al₂O₃, Ni:Rh(10:1)/Al₂O₃ and Ni:Ru(10:1)/Al₂O₃ showed highest activity for C-C bond breaking (Equation 4.1-2) and water gas shift reaction (Equation 4.1-3) and low activity for methanation thus high activity and high hydrogen concentration were obtained over the Ni impregnated with Pd, Rh and Ru of stoichiometry ratio 10:1 [6]. This could be deduced by highest fraction of CO₂/CO in Figure 4.1.2-2(i) and lowest CH₄ production in Figure 4.1.2-2 (ii) with Ni-M(10:1)/Al₂O₃ (M=Pd, Rh and Ru) respectively.

Based on Figure 4.1.2-1 (i), it was deduced that Ni impregnated with Pd, Rh and Ru with Ni:metal ratio of 10:1 and 1:1 increased the overall rate of hydrogen production as compared to monometallic catalyst. This was expected from the XRD analysis and it could be due to the change of lattice parameter of support during APR reaction.

However, the trend did not match the performance of Rh impregnated Ni catalyst sample. It showed low activity of C-C bond breaking reaction. The possible reasons for this is that Ni-Rh is less reduced compared to Pd and Ru [7]. Therefore, it was believed that the strong metal – support interaction inhibited the alloy formation and reduces the catalytic activity of bimetallic catalysts. This would also be discussed in depth in the subsequent chapter with the XAFS technique. Also, the tendency of coke formation in Ni impregnated Rh catalyst which was depicted in the TEM images. It is also important to note that Ni:Rh(1:1)/Al₂O₃ exhibited the least active metal site as shown in Table 4.1.1-1 which resulted in the lowest hydrogen production rate. Additionally, Ni:Rh(1:1)/Al₂O₃ favours methanation with high CH₄ production as indicate in Figure 4.1.2-2(i) and produce less fraction of CO₂/CO as shown in Figure 4.1.2(ii), indicating low WGS reaction.

Figure 4.1.2-1 illustrated the liquid glycerol conversion of aqueous phase reforming. However, the Ni- Pd, Rh and Ru catalysts did not exhibit a general trend as compared to rate of gaseous production. This might be due to the formation of complex mixture of hydrocarbons and oxygenated hydrocarbons which are difficult to be identified. As shown in Figure 3.2.2-2 glycerol peak could be observed at about 17.4 min on a HPLC data. Besides the glycerol peak, they were also some unknown peaks shown on the RID detector of the HPLC data obtained at about 12min, 15min and 27min. A few examples of unknown peaks observed on the HPLC data are illustrated in Figure 4.1.2-3 and 4.1.2-4.

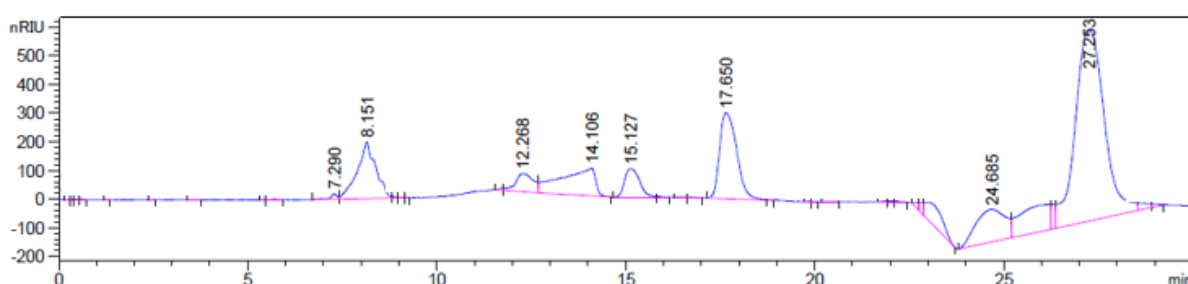


Figure 4.1.2-3: Refractive Index Signal of liquid product mixture at 60 min (reaction condition: 210 °C, 35 bar, 10 sccm Argon, 2 wt% glycerol feedstock, Ru/Al₂O₃ catalyst)

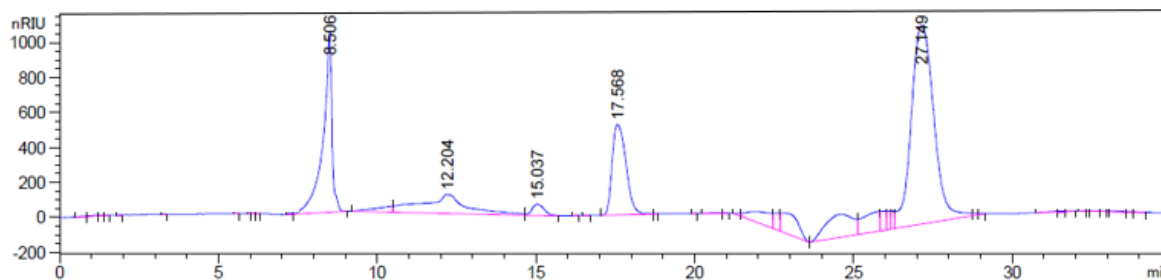


Figure 4.1.2-4: Refractive Index Signal of liquid product mixture at 60 min (Reaction Condition: 210 °C, 35 bar, 10 sccm Argon, 2 wt% glycerol feedstock, Ni:Pd(10:1)/Al₂O₃ catalyst)

The unknown peaks were tested against some of the possible liquid bi-product of APR including ethylene glycol, 1-2 propanediol, 1-3 propanediol, acetone and ethanol. The standard ethylene glycol, 1-2 propanediol, 1-3 propanediol, methanol and acetone exhibit peak at 20 min, 21 min, 22 min, 25 min and 28 min respectively and their retention time did not match any of the unknown peaks of the liquid product. This indicate that the unknown peaks observed are neither ethylene glycol, 1-2 propanediol, 1-3 propanediol, methanol nor acetone. However, one of the unknown peak matches the retention time of standard ethanol sample at about 27 min. This would then indicate the presence of ethanol traces in the liquid product of APR glycerol. These were not quantified. Further analysis would require to identify the remaining unknown peaks of the liquid product for a complete liquid glycerol conversion studies.

4.2 Conclusion

Ni impregnated with M (Pd, Rh and Ru) supported on alumina were prepared in various metal loading. While the concentration of support was kept constant, the metal loading of Ni:M was prepared in a stoichiometric ratio of (10:1, 1:1, 0:1 and 1:0). The effect of impregnating of metal on Ni on the overall rate of hydrogen production was analysed. Impregnating Ni with Pd and Ru increases the overall rate of hydrogen production. As compared to Pd, Rh and Ru series of catalyst, Ni: M of 10:1 exhibit the highest hydrogen production rate. It could also deduced that Ni:M of 10:1 showed highest activity for C-C bond breaking and water gas shift reaction and low activity for methanation thus high activity and high hydrogen concentration were obtained.

4.3 References

- [1] A. Tanksale, C.H. Zhou, J.N. Beltramini, G.Q. Lu, Hydrogen production by aqueous phase reforming of sorbitol using bimetallic Ni–Pt catalysts: metal support interaction, *Journal of Inclusion Phenomena and Macrocyclic Chemistry*, 65 (2009) 83-88.
- [2] D.L. King, L. Zhang, G. Xia, A.M. Karim, D.J. Heldebrant, X. Wang, T. Peterson, Y. Wang, Aqueous phase reforming of glycerol for hydrogen production over Pt–Re supported on carbon, *Applied Catalysis B: Environmental*, 99 (2010) 206-213.
- [3] W.Z. Wenbo Yue, *Porous Crystals of Cubic Metal Oxides Templated by Cage-Containing Mesoporous Silica*, The Royal Society of Chemistry, (2007).
- [4] C.G. Hongkun He, *A General Strategy for the Preparation of Carbon Nanotubes and Graphene Oxides Decorated with PdO Nanoparticles in Water*, (2010).
- [5] E. Fazio, S.G. Leonardi, M. Santoro, N. Donato, G. Neri, F. Neri, Synthesis, characterization and hydrogen sensing properties of nanosized colloidal rhodium oxides prepared by Pulsed Laser Ablation in water, *Sensors and Actuators B: Chemical*, 262 (2018) 79-85.
- [6] G. Wen, Y. Xu, H. Ma, Z. Xu, Z. Tian, Production of hydrogen by aqueous-phase reforming of glycerol, *international journal of hydrogen energy*, 33 (2008) 6657-6666.
- [7] T.V. Reshетенko, L.B. Avdeeva, Z.R. Ismagilov, A.L. Chuvilin, V.A. Ushakov, Carbon capacious Ni-Cu-Al₂O₃ catalysts for high-temperature methane decomposition, *Applied Catalysis A: General*, 247 (2003) 51-63.

This page intentionally left blank

CHAPTER 5: EX-SITU XANES ANALYSIS OF PD, RH AND RU MONO- , BI - METALLIC CATALYST

Abstract

Ex-situ XANES techniques were used to describe the chemical effect such as the change in oxidation state prior to and after reduction with the introduction of Pd, Rh and Ru to Ni based catalyst supported on alumina. In return, the effect on the catalytic activity of bimetallic samples via APR of glycerol.

Chapter Contents

5.1	Results and Discussions	69
5.1.1	Ex-Situ XANES Analysis of Mono- and Bi-Metallic Catalyst	69
5.1.2	APR Activity.....	76
5.2	Conclusions	78
5.3	References	80

5.1 Results and Discussions

5.1.1 Ex-Situ XANES Analysis of Mono- and Bi-Metallic Catalyst

In the first part of work, the effect of the noble metal on Ni/Al₂O₃ catalyst at different composition of Ni:M (M=Pd, Rh or Ru) at the normalised near spectrum were investigated.

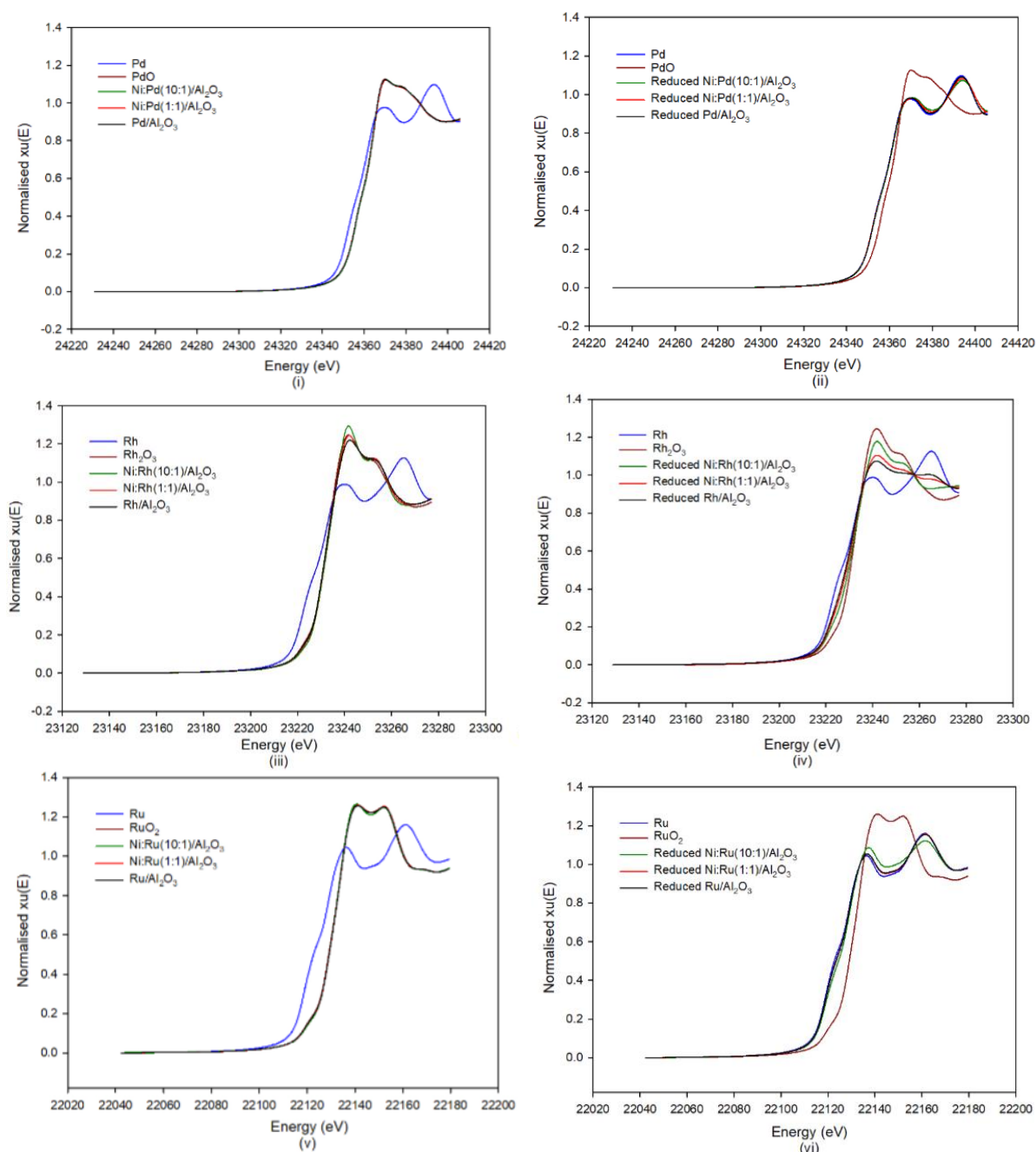
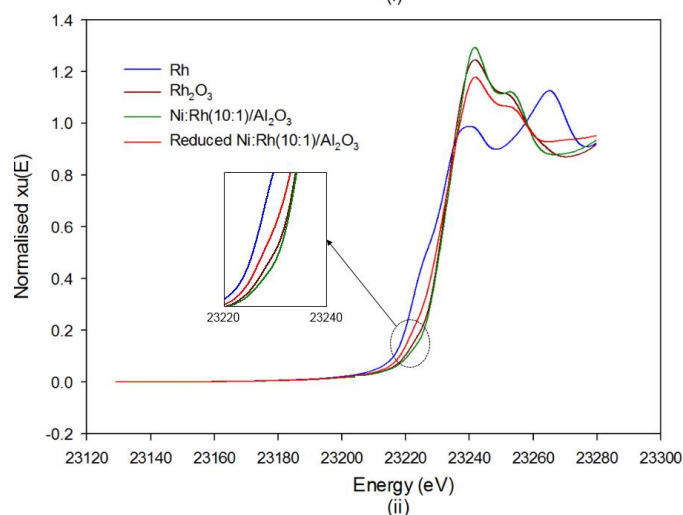
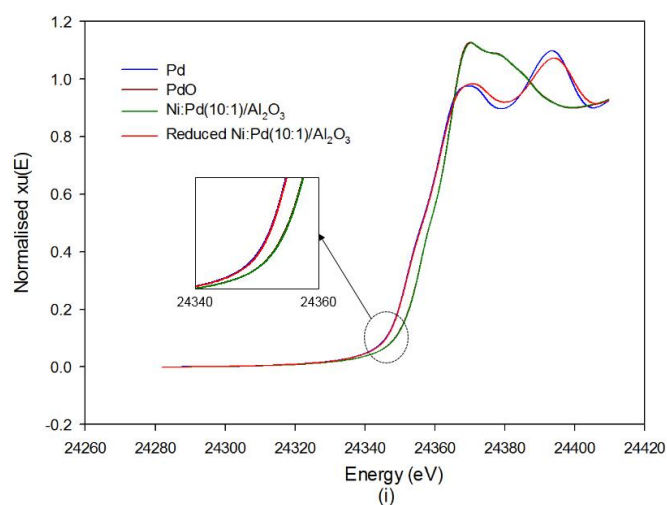


Figure 5.1.1-1: Normalised near spectra of (i) Pd foil, PdO, Ni:Pd(10:1)/Al₂O₃, Ni:Pd(1:1)/Al₂O₃, Pd/Al₂O₃ (ii) Pd foil, PdO, Reduced Ni:Pd(10:1)/Al₂O₃, Reduced Ni:Pd(1:1)/Al₂O₃, Reduced Pd/Al₂O₃ (iii) Rh foil, Rh₂O₃, Ni:Rh(10:1)/Al₂O₃, Ni:Rh(1:1)/Al₂O₃, Rh/Al₂O₃ (iv) Rh foil, Rh₂O₃, Reduced Ni:Rh(10:1)/Al₂O₃, Reduced Ni:Rh(1:1)/Al₂O₃, Reduced Rh/Al₂O₃ (v) Ru foil, RuO₂, Ni:Ru(10:1)/Al₂O₃, Ni:Ru(1:1)/Al₂O₃, Ru/Al₂O₃ (vi) Ru foil, RuO₂, Reduced Ni:Ru(10:1)/Al₂O₃, Reduced Ni:Ru(1:1)/Al₂O₃, Reduced Ru/Al₂O₃

The Pd, Rh and Ru K-edge XANES spectra of fresh catalyst are shown in Figure 5.1.1-1 are similar to that of PdO, Rh₂O₃ and RuO₂, respectively. This would also characterised the presence of Pd²⁺, Rh³⁺ and Ru⁴⁺ in the as-synthesised sample respectively [1].

After reduction, it was observed that in Figure 5.1.1-1 all Pd and Ru sample were reduced from PdO → Pd and RuO₂ → Ru respectively [1]. This is because Pd and Ru K edge XANES spectra are more similar to that of metallic Pd and Ru foil. These results suggested that reduced Pd and Ru catalyst mainly exist in metallic state (0 oxidation state). However, the result did not match with Rh bi- and mono-metallic catalyst. It is important to note that the Rh K edge does not show similar spectral shape as that of Rh foil. A very small decrease in intensity and small energy shift (~0.5 eV) as Rh loading increases were observed which indicate that some small content of +3 can be present after reduction [1]. This could then further explain a lower metal dispersion (%) of bimetallic Rh in comparison to Ni/Al₂O₃ as shown in Table 4.1.1-1.



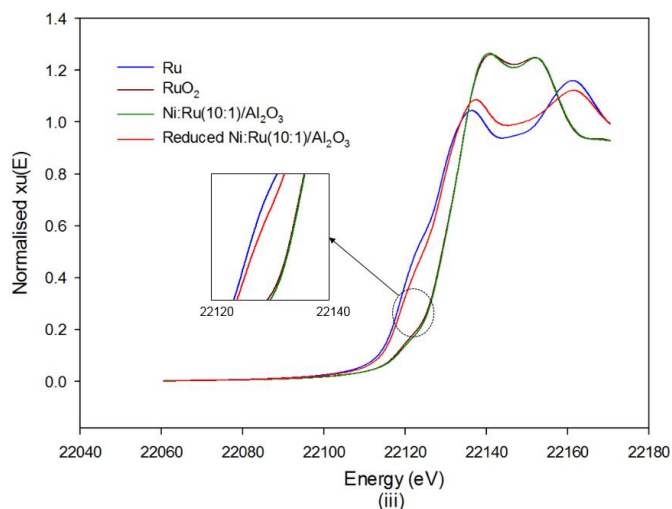


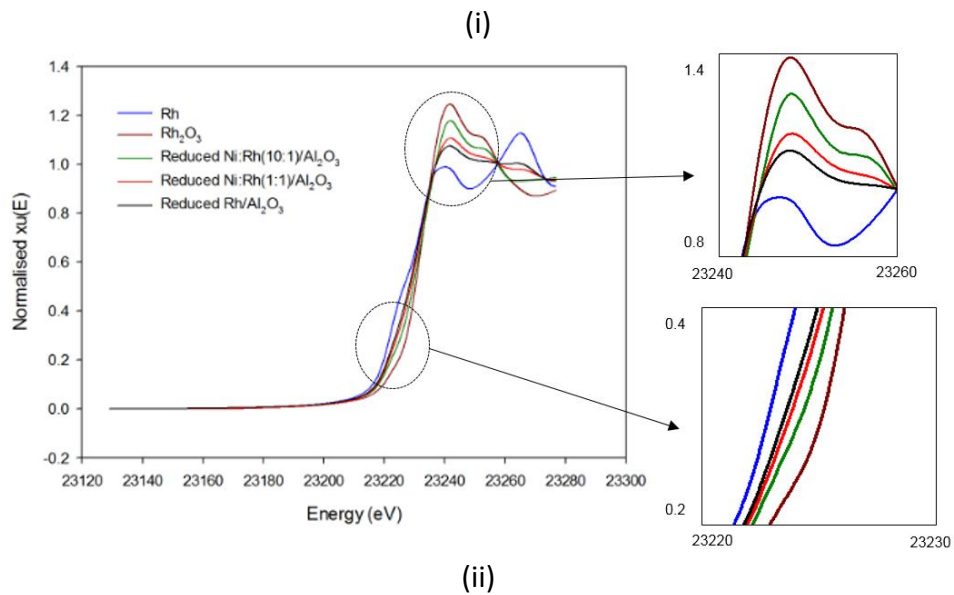
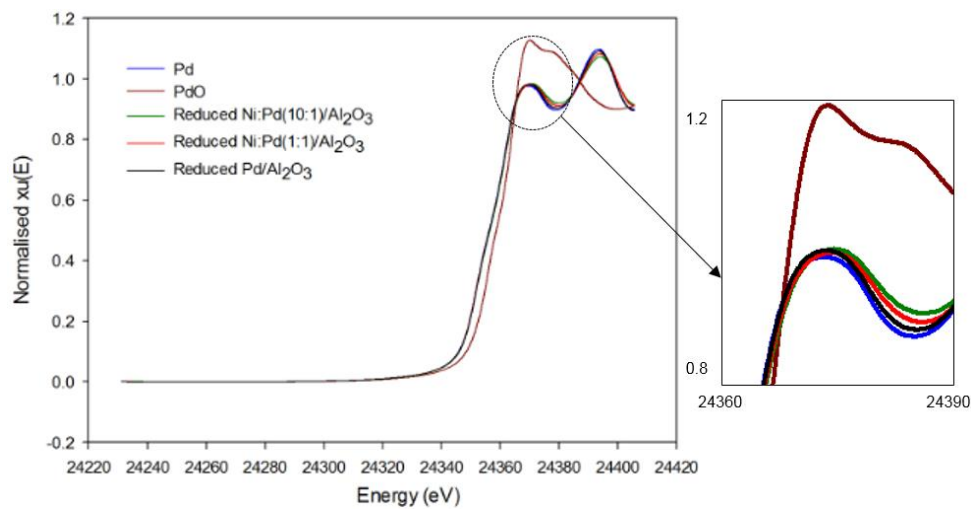
Figure 5.1.1-2: : The normalised near spectra obtained for (i) Pd foil, PdO, Ni:Pd(10:1)/Al₂O₃ and Reduced Ni:Pd(10:1)/ Al₂O₃ (ii) Rh foil, Rh₂O₃, Ni:Rh(10:1)/ Al₂O₃ and Reduced Ni:Rh(10:1)/ Al₂O₃ (iii) Ru foil, RuO₂, Ni:Ru(10:1)/Al₂O₃ and Reduced Ni:Ru(10:1)/Al₂O₃

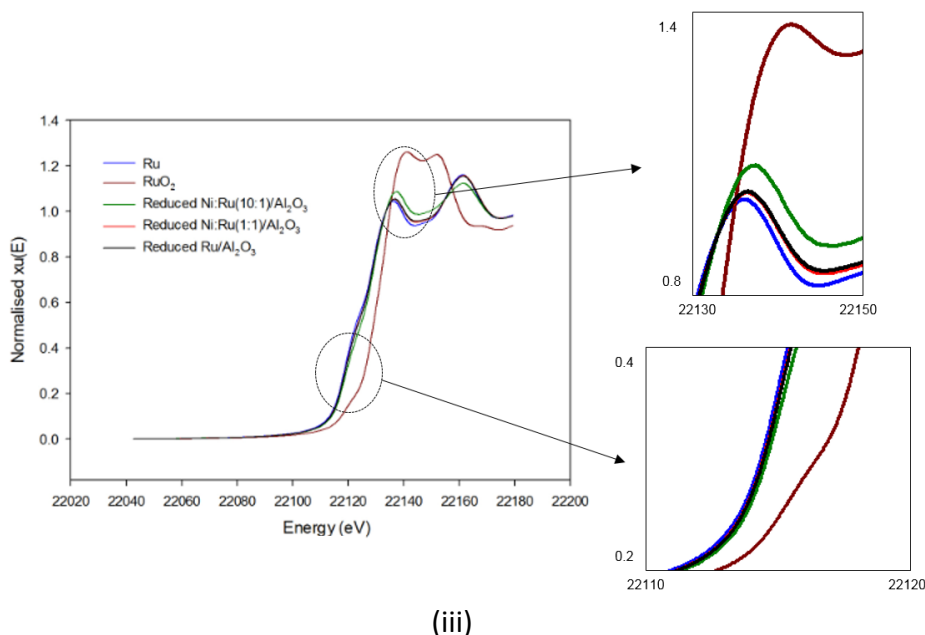
Ni:Pd(10:1)/Al₂O₃ peak is shifted about 0.01 keV to higher energies from the peak PdO while reduced Ni:Pd(10:1)/Al₂O₃ peak is shifted about 0.02keV to higher energies from peak Pd[2]. As shown in Figure 5.1.1-2(i), the spectra of reduced Ni: Pd(10:1)/Al₂O₃ is characterized by a shift in the edge of lower energy. The shift of the absorption edge to lower energy corresponds to the reduction of the absorbing Pd atom [2]. In detailed comparison of fresh and reduced spectra, the intensity of the Ni: Pd (10:1)/Al₂O₃ peak around 24.37 keV is higher than the first peak of catalyst after reduction. This characteristic of the spectral shape has been observed on a catalyst, which has high metal dispersion and activities [2]. This suggests that the fresh catalyst has high dispersion of Pd on support [2]. This could be supported by the data obtained in Table 4.1.1-1 where metal dispersion of bimetallic Ni-Pd is higher than that of monometallic Ni samples.

Qualitatively, Ni: Rh (10:1)/Al₂O₃ and reduced Ni:Rh(10:1)/Al₂O₃ peak is shifted about 0.01 keV to higher energies from the peak Rh₂O₃ and Rh, respectively. In comparison of as-synthesis and reduced Ni:Rh(10:1)/Al₂O₃, reduced sample depicts by a shift in the edge of lower energy due to the reduction of the absorbing Rh atom [2].

Likewise, Ni:Ru(10:1)/Al₂O₃ and reduced Ni:Ru(10:1)/Al₂O₃ peak is shifted about 0.01 keV to higher energies from the peak RuO₂ and Ru, respectively [2]. Like all the other noble metal-Ni catalyst, the reduced sample characterized by a shift in the edge of lower energy. The shift couple be explained by the reduction of the absorbing Ru atom [2]. The intensity of the

Ni:Ru(10:1)/Al₂O₃ peak around 22.125 keV is higher than that of the reduced catalyst due to high dispersion of Ru on alumina [2].





(iii)

Figure 5.1.1-3: Close-up of normalised near spectra obtained for (i) Pd foil, PdO and Reduced Ni:Pd(x:y)/Al₂O₃ (ii) Rh foil, Rh₂O₃ and Reduced Ni:Rh(x:y)/Al₂O₃ (iii) Ru foil, RuO₂ and Reduced Ni:Ru(x:y)/Al₂O₃ where x:y = 10:1, 1:1, 0:1

In Figure 5.1.1-3, the XANES spectra shifted to a higher energy in the order of Ni:M(10:1)/Al₂O₃ followed by Ni:M(1:1)/Al₂O₃ then M/Al₂O₃ where M is Pd, Rh and Ru. As the Nickel in the bimetallic samples increases, the shift is closer towards the reference PdO, Rh₂O₃ and RuO₂ respectively. Besides that, the intensity of the spectra also decreases in the same manner Ni:M(10:1)/Al₂O₃ followed by Ni:M(1:1)/Al₂O₃ then M/Al₂O₃. The intensity of the XANES spectra increases with the increasing nickel content in the bimetallic samples. This deduced that the higher the Nickel content in the bimetallic catalyst, the bonding between noble metal and neighbouring atom are more similar to that of PdO, Rh₂O₃ and RuO₂ respectively.

Second part of analysis work, Fourier transforms of the K-edge EXAFS spectra, which are the radial structure functions (RSF) were presented in Figure 5.1.1-4.

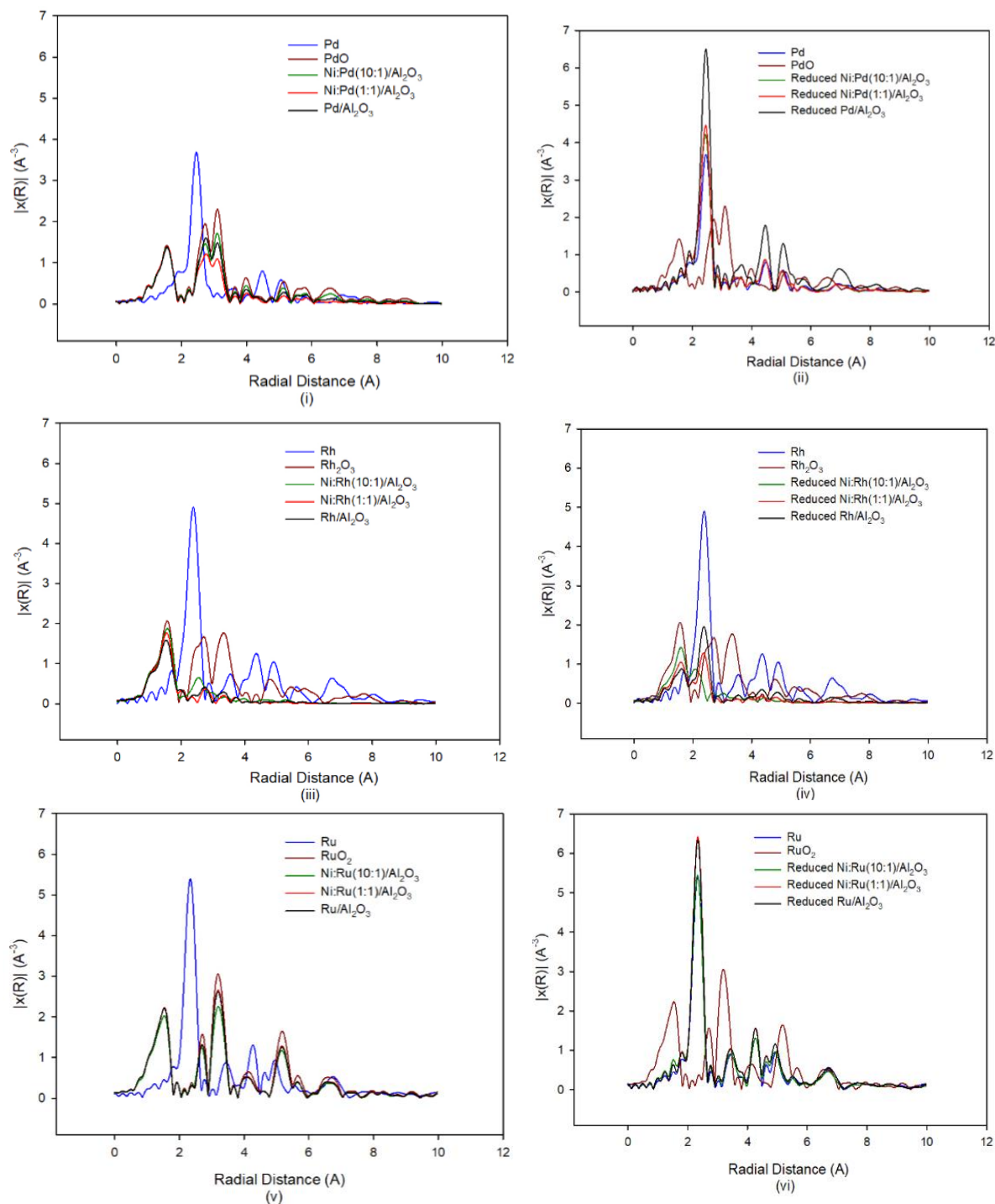


Figure 5.1.1-4: Radial structure function of (i) Pd foil, PdO, Ni:Pd(10:1)/Al₂O₃, Ni:Pd(1:1)/Al₂O₃, Pd/Al₂O₃ (ii) Pd foil, PdO, Reduced Ni:Pd(10:1)/Al₂O₃, Reduced Ni:Pd(1:1)/Al₂O₃, Reduced Pd/Al₂O₃ (iii) Rh foil, Rh₂O₃, Ni:Rh(10:1)/Al₂O₃, Ni:Rh(1:1)/Al₂O₃, Rh/Al₂O₃ (iv) Rh foil, Rh₂O₃, Reduced Ni:Rh(10:1)/Al₂O₃, Reduced Ni:Rh(1:1)/Al₂O₃, Reduced Rh/Al₂O₃ (v) Ru foil, RuO₂, Ni:Ru(10:1)/Al₂O₃, Ni:Ru(1:1)/Al₂O₃, Ru/Al₂O₃ (vi) Ru foil, RuO₂, Reduced Ni:Ru(10:1)/Al₂O₃, Reduced Ni:Ru(1:1)/Al₂O₃, Reduced Ru/Al₂O₃

In Figure 5.1.1-4 (i) of PdO spectra, the peak at 1.6 Å corresponds to the nearest Pd-O bonds and the 2.7 Å as well as the 3.1 Å correspond to the second and the third Pd-Pd shells, respectively [2]. For as-synthesised Pd mono- and Pd-Ni bi-metallic alloy catalyst, the three peaks assigned to the nearest bonds (Pd-O), second-nearest neighbour (Pd-Pd) and the third

nearest bonds (Pd-Pd) were observed to be at 1.6 Å, 2.7 Å and 3.1 Å, respectively. The three peaks are located at the same positions as those PdO. However, in each result the RSFs differ in terms of the amplitude. The amplitudes of second and third peaks of Ni: Pd(x:y)/Al₂O₃ were much weaker than those of the PdO and decreases in the order Ni: Pd(10:1)/Al₂O₃ > Pd/Al₂O₃ > Ni: Pd(1:1)/Al₂O₃ in spite that the first peaks have the same amplitudes. This kind of phenomenon has been reported where there is crystal distortion in the Pd promoted Ni catalyst [2]. NiO induces disordering of the outer shell of Pd scattering atoms in the alumina support [2]. This could also be evidenced by a shift in XRD peaks in Figure 4.1.1-1 which indicate lattice parameter changes which imply electronic effect that promotes C-C cleavage over C-O cleavage. Thus, Pd enhances hydrogen formation.

Figure 5.1.1-4 (ii) shows the FTs for catalyst of reduced Ni: Pd(x:y)/Al₂O₃ and Pd foil as standard sample. All FTs for reduced catalysts and the Pd foil show the peak corresponding to that for Pd-Pd in metal (Pd foil) at 2.4 Å. This further confirming the reduced Pd species mainly existing in metallic state. However, the intensity of the peak corresponding to the metallic Pd-Pd bond decreases in the order, reduced Pd/Al₂O₃ > reduced Ni: Pd(1:1)/Al₂O₃ > reduced Ni: Pd(10:1)/Al₂O₃, indicating that Pd particle size decreases with increasing Ni content. From Scherrer equations on XRD data in Figure 4.1.1-1 obtained, the statement was proven as Pd particle size decreased from 11.98 nm in Ni: Pd(1:1)/Al₂O₃ to 8.52 nm Pd particle size in Ni: Pd(10:1)/Al₂O₃ samples.

For Rh₂O₃ standard sample, the peak at 1.6 Å, 2.7 Å and 3.3 Å correspond to the nearest Rh – O bonds, second and the third Rh-Rh shells, respectively [3]. However, for Ni: Rh(x:y)/Al₂O₃ sample, only the peak correspond to the nearest Rh-O appear to be at the same location as those Rh₂O₃. In addition, the RSFs differ from Rh₂O₃ in term of the amplitude. The amplitude peak is much lower in those Rh mono- and bimetallic catalyst as compared to Rh₂O₃ and decreases in the order Ni: Rh (10:1)/Al₂O₃ > Ni: Rh (1:1)/Al₂O₃ > Rh/Al₂O₃. This could be explained by the crystal disordering effect with the presence of NiO on the alumina support [2]. For the reduced Rh sample and Rh foil as shown in Figure 5.1.1-4(iv), only reduced Rh/Al₂O₃ and Ni: Rh(1:1)/Al₂O₃ show the peak corresponding to that for Rh-Rh in metal (Rh foil) at 2.4 Å. This result further confirms that not all the reduced Rh catalysts are in metallic state which had been previously reported in Figure 5.1.1-1(iv). The peak intensity

corresponding to the Rh-O bond decreases in the order, reduced Rh/Al₂O₃ > reduced Ni:Rh(1:1)/Al₂O₃, indicating the presence of Ni and support alumina that prevent Rh catalyst from being easily reduced Rh metal [2].

Likewise for Ru catalyst, XANES response characteristic of RuO₂ with average Ru-O and Ru-Ru interatomic distances of 1.5 Å and 3.19 Å [4]. Ni: Ru(x:y)/Al₂O₃ depicted the same peak at 1.5 Å and 3.19 Å which correspond to the Ru-O and Ru-Ru, respectively but with different amplitude. The amplitude decreases in the order RuO₂ > Ni: Ru (1:1)/Al₂O₃ > Ru/Al₂O₃ > Ni: Ru (10:1)/Al₂O₃ >. At 2.3 Å in Figure 5.1.1-4(vi), the Ru-Ru bonds peak analogous to that of metallic Ru in which explain the existence of Ru in its metallic state but decreases with the order reduced Ru/Al₂O₃ > Ni:Ru(1:1)/Al₂O₃ > reduced Ni:Ru(10:1)/Al₂O₃ [5]. The Ru particle size decreases with increasing Ni content which could be evidenced by Scherrer equations on XRD data illustrated on Figure 4.1.1-1. Ni:Ru(10:1)/Al₂O₃ exhibited a smaller Ru crystallite size of 5.1 nm as compared to Ni:Ru(1:1)/Al₂O₃ of 9.63 nm. This results indicate that the larger particles size prevents Ru catalyst from being easily reduced to Ru metal and this could have an effect on the retention of catalytic activities [2].

5.1.2 APR Activity

The next part of work was to relate the effect of various metal loading on Nickel and its overall rate of hydrogen production. As shown in Chapter 4 Figure 4.1.2-1, Pd mono- and Pd-Ni bi-metallic supported on alumina catalyst depicted the highest overall H₂ production followed by Ru- then Rh- Ni catalyst. This could be due to high dispersion of Pd on the alumina support as evidenced in the shifting of the XANES spectra to a higher energy [2]. On the other hand, Rh-Ni catalyst showed the lowest rate of H₂ production and this is because Rh catalysts were not fully reduced to their metallic state even after reduction treatment for same time as the Pd promoted catalysts. In Rh samples, the strong metal-support interaction may have inhibited the alloy formation of the sample. These results were supported by the normalised near-edge spectra as shown in Figure 5.1.1-1 (iv) such that the Rh K edge (after reduction) does not show similar spectral shape as that of Rh foil. This could indicate that adsorbed Rh in its reduced state was not the dominant surface species during aqueous phase reforming reaction [6]. In XRD data as shown in Figure 4.1.1-1, they were not any peak shift in Rhodium

oxide bimetallic Ni:Rh(x:y)/Al₂O₃ and Ni:Ru(x:y)/Al₂O₃ respectively as compared to standard sample.

Among the Pd mono- and bi-metallic catalyst, the overall rate of H₂ rate of production decreased in the following order: Ni:Pd(10:1)/Al₂O₃ > Ni:Pd(1:1)/Al₂O₃ > Pd/Al₂O₃ while Ni:Ru(x:y)/Al₂O₃ catalyst decreased in the following order: Ni:Ru(10:1)/Al₂O₃ > Ni:Ru(1:1)/Al₂O₃ > Ru/Al₂O₃. From the results, it was deduced that the higher the metal loading impregnated on Ni depicted the higher rate of H₂ production. This could be explained by the following factors:

(i) Pd or Ru particle size decreases with increasing Ni contents which in turn greater surface species during the APR reaction [7]. The Pd and Ru particle size decreases with increasing Ni content which could also be evidenced by Scherrer equations on XRD data illustrated on Figure 4.1.1-1. Ru bimetallic catalyst exhibited Ru particle size decreased from 9.63 nm in Ni:Ru(1:1)/Al₂O₃ to 5.1 nm in Ni:Ru(10:1)/Al₂O₃ samples while Pd particle size decreased from 11.98 nm in Ni:Pd(1:1)/Al₂O₃ to 8.52 nm Pd particle size in Ni:Pd(10:1)/Al₂O₃ samples. In Figure 5.1.1-4, the intensity of the peak corresponding to the metallic Pd-Pd bond decreases in the order indicating that Pd particle size decreases. Likewise, Ru-Ru bonds peak analogous to that of metallic Ru decreases.

(ii) The larger particles size prevents Pd or Ru catalyst from being easily reduced to their metallic state and this would have an effect on the retention of catalytic activities [2]. Figure 5.1.1-3 indicated that the addition M causes the XANES spectra shift.

(iii) The higher the nickel content in the catalyst, the bonding between noble metal and neighbouring atom are more similar to that of PdO, Rh₂O₃ and RuO₂ respectively. In Figure 5.1.1.3, the higher Nickel content samples exhibited a similar spectra shape to that of PdO, Rh₂O₃ and RuO₂ respectively.

Meanwhile, H₂ production rate of Ni:Rh(x:y)/Al₂O₃ decreased in the following order: Ni:Rh(10:1)/Al₂O₃ > Rh/Al₂O₃ > Ni:Rh(1:1)/Al₂O₃. Unlike Pd and Ru, the general trend such that the higher metal loading impregnated on Ni exhibited the higher production of H₂ did not match with the performance on Rh samples. In fact, Rh/Al₂O₃ showed a higher H₂ production rate than that of Ni:Rh(1:1)/Al₂O₃. In the RSF show in Figure 5.1.1-4 (iv), the peak intensity

corresponding to the Rh-O bond decreases in the order, reduced Rh/Al₂O₃ > reduced Ni:Rh(1:1)/Al₂O₃, indicating the presence of Ni and support alumina that prevent Rh catalyst from being easily reduced Rh metal [2]. This could also be observed by the low active metal site of Rh catalysts as illustrated in Appendix A.1.2 Figure A.1.2-1.

5.2 Conclusions

By combining the catalytic performance tests of APR of glycerol and results of X-ray Absorption Near Edge Spectroscopy (XANES), the experiments had contributed to the elucidation of issues concerning the Ni-catalysed APR reactions include: (i) the change in oxidation state and phase of metal component (e.g. Pd, Rh and Ru) in Ni catalyst supported on γ -Al₂O₃ after reduction (ii) in depth understanding of the structural mechanism of various metal loading impregnated with Ni catalyst.

Overall, Pd series of alumina supported catalyst depicted the highest H₂ rate of production followed by Ru- then Rh- Ni catalyst. This could be due to high dispersion of Pd on the alumina support. On the other hand, Rh-Ni catalyst showed the lowest rate of H₂ production and this is because Rh catalysts were not in their reduced state during APR reaction, the strong metal support interaction inhibited the alloy formation of the sample. This could then further verify the analysis in Chapter 4.

In general, the higher the metal loading impregnated on Ni catalyst the higher the H₂ production rate. This could be explained by three primary reasons: (i) the metal particle size decreases with increasing Ni contents which in turn greater surface species during the APR reaction [7].(ii) The larger particles size prevents the catalyst from being easily reduced to its metallic state and this would influence the retention of catalytic activities. (iii) The higher the nickel content in the catalyst, bimetallic samples are slightly more oxide and these would favour APR of glycerol in hydrogen production.

However, the Rh based catalyst did not obey this trend, in contrast, Rh/Al₂O₃ showed a higher H₂ production rate than that of Ni:Rh(1:1)/Al₂O₃. In the RSF obtained, the peak intensity corresponding to the Rh-O bond decreases in the order, reduced Rh/Al₂O₃ > reduced Ni:Rh(1:1)/Al₂O₃, indicating the presence of Ni and support alumina that prevent Rh catalyst

from being easily reduced Rh metal. Therefore, reducibility of the catalyst is one of the major factor towards catalytic in APR of glycerol.

5.3 References

- [1] A.E.P. de Lima, D.C. de Oliveira, In situ XANES study of Cobalt in Co-Ce-Al catalyst applied to Steam Reforming of Ethanol reaction, *Catalysis Today*, 283 (2017) 104-109.
- [2] W.B. Li, Y. Murakami, M. Orihara, S. Tanaka, K. Kanaoka, K.-i. Murai, T. Moriga, E. Kanezaki, I. Nakabayashi, XAFS and XRD studies of PdO-CeO₂ catalysts on γ -Al₂O₃, *Physica Scripta*, 2005 (2005) 749.
- [3] D. Beck, T. Capehart, C. Wong, D. Belton, XAFS Characterization of Rh/Al₂O₃ after Treatment in High-Temperature Oxidizing Environments, *Journal of Catalysis*, 144 (1993) 311-324.
- [4] Y. Mo, M.R. Antonio, D.A. Scherson, In situ Ru K-edge X-Ray absorption fine structure studies of electroprecipitated ruthenium dioxide films with relevance to supercapacitor applications, *The Journal of Physical Chemistry B*, 104 (2000) 9777-9779.
- [5] Y.H. Kim, J.E. Park, H.C. Lee, S.H. Choi, E.D. Park, Active size-controlled Ru catalysts for selective CO oxidation in H₂, *Applied Catalysis B: Environmental*, 127 (2012) 129-136.
- [6] H. Wang, J. Lu, C.L. Marshall, J.W. Elam, J.T. Miller, H. Liu, J.A. Enterkin, R.M. Kennedy, P.C. Stair, K.R. Poeppelmeier, In situ XANES study of methanol decomposition and partial oxidation to syn-gas over supported Pt catalyst on SrTiO₃ nanocubes, *Catalysis Today*, 237 (2014) 71-79.
- [7] L. Liu, J. Fei, M. Cui, Y. Hu, J. Wang, XANES spectroscopic study of sulfur transformations during co-pyrolysis of a calcium-rich lignite and a high-sulfur bituminous coal, *Fuel Processing Technology*, 121 (2014) 56-62.

This page intentionally left blank

CHAPTER 6: CONCLUSIONS AND RECOMMENDATIONS

Abstract

An overall summary of the research study obtained in Chapter 4 and 5 as well as an overview of future study recommendations.

Table of Contents

6.1	Conclusions	83
6.2	Hypotheses	85
6.3	Recommendations	85
6.4	References	87

6.1 Conclusions

APR process is a promising synthetic technique due to its energy efficiency and eliminates undesirable product which are typically occurred at processes conducted at elevated temperature as well as less complication processing requirement as APR reaction can be carried out in a single reactor than the multi-reactor steam reforming system. Moreover, water gas shift (WGS) reaction is an exothermic reaction which favours at lower temperature. Therefore, resulting in low level of CO (< 300ppm) production than the conventional steam reforming processes [1].

Reviewing previous studies on APR of glycerol has indicated that Ni monometallic catalysts are active towards the reactions. However, introduction of second metal to the catalytic system may provide significant changes in the catalytic activity and selectivity as compared with those of individual metals. Therefore, the research has focused on studying the effect of various additives with different metal loading, including Pd, Rh and Ru over Ni catalyst on their catalytic activity towards aqueous phase reforming reaction of glycerol with respect to their structural changes.

Ni impregnated with M (Pd, Rh and Ru) supported on alumina were prepared in various metal loading. While the concentration of support was kept constant, the metal loading of Ni:M was prepared in a stoichiometric ratio of (10:1, 1:1, 0:1 and 1:0). In **Chapter 4**, the effect of impregnating of metal on Ni on the overall rate of hydrogen production was analysed. Impregnating Ni with Pd and Ru increases the overall rate of hydrogen production. The higher the Pd and Ru on Ni catalyst, the higher the rate of hydrogen production. However, the trend did not match the Ni-Rh catalyst as it was suggested that the sample might not be well reduced, the strong metal-support interaction inhibited the alloy formation of the sample.

The Ni:Pd(x:y)/Al₂O₃ overall rate of hydrogen production decreased in the following order: Ni:Pd(10:1)/Al₂O₃ > Ni:Pd(1:1)/Al₂O₃ > Pd/Al₂O₃ > Ni/Al₂O₃ and Ni:Rh(x:y)/Al₂O₃ decreased in the following order: Ni:Rh(10:1)/Al₂O₃ > Ni/Al₂O₃ > Rh/Al₂O₃ > Ni:Rh(1:1)/Al₂O₃ while Ni:Ru(x:y)/Al₂O₃ catalyst decreased in the following order: Ni:Ru(10:1)/Al₂O₃ > Ni:Ru(1:1)/Al₂O₃ > Ru/Al₂O₃ > Ni/Al₂O₃. It could be deduced that introduction of noble metal to Ni catalytic system enhanced the rate of hydrogen production and this could be due to (i)

the alter of electronic structure of Ni catalysts affecting its metal dispersion (ii) favour of WGS reaction in Ni-M catalyst as compared to Ni monometallic catalyst supported on alumina (M=Pd, Rh and Ru).

By combining the catalytic performance tests of APR of glycerol and results of X-ray Absorption Near Edge Spectroscopy (XANES) as described in **Chapter 5**, the experiments had contributed to the elucidation of issues concerning the Ni-catalysed APR reactions include: (i) the change in oxidation state and phase of metal component (e.g. Pd, Rh and Ru) in Ni catalyst supported on γ -Al₂O₃ after reduction (ii) understanding of the shifting of XANES spectra due to Ni alloy formation in various metal loading impregnated with Ni catalyst.

Overall, Pd series of alumina supported catalyst depicted the highest H₂ rate of production followed by Ru- then Rh- Ni catalyst. This could be due to high dispersion of Pd on the alumina support. On the other hand, Rh-Ni catalyst showed the lowest rate of H₂ production and this has further confirm that Rh catalysts were not in their reduced state during APR reaction, the strong metal support interaction inhibited the alloy formation of the sample. This could then further verify the analysis as prescribed previously.

In general, the higher the metal loading impregnated on Ni catalyst the higher the H₂ production rate. This could be explained by three primary reasons: (i) the metal particle size decreases with increasing Ni contents which in turn greater surface species during the APR reaction [2].(ii) The larger particles size prevents the catalyst from being easily reduced to its metallic state and this would influence the retention of catalytic activities. (iii) The higher the nickel content in the catalyst, the bonding between noble metal and neighbouring atom are more similar to that of PdO, Rh₂O₃ and RuO₂ respectively. Even with the same reduction treatment, the high Ni loading in the sample lead to a higher oxidation state.

However, the Rh based catalyst did not obey this trend, in contrast, Rh/Al₂O₃ showed a higher H₂ production rate than that of Ni:Rh(1:1)/Al₂O₃. In the RSF obtained, the peak intensity corresponding to the Rh-O bond decreases in the order, reduced Rh/Al₂O₃ > reduced Ni:Rh(1:1)/Al₂O₃, indicating the presence of Ni and support alumina that prevent Rh catalyst from being easily reduced Rh metal. Therefore, reducibility of the catalyst is one of the major factor towards catalytic in APR of glycerol.

6.2 Hypotheses

Comparison between bimetallic and monometallic catalysts regarding to their particle size, electronic effects and oxidic coverages are discussed as follows :

(i) Particle size

The interaction between Ni and alumina was further strengthened through the addition of secondary metal species. Thus, the stronger interaction between bimetallic species and support resulting in smaller NiO size.

(ii) Electronic effects

Introduction of metal species alters the electronic structure of Ni catalyst. For examples, comparison of calcined Ni with calcined Ni:Pd(x:y)/Al₂O₃ shows a shift in XRD peaks which indicates lattice parameter changes which imply some electronic effect that promotes C-C cleavage over C-O cleavage. Thus, bimetallic samples enhances H₂ formation.

(iii) Oxide coverages

Noble metal assist in Ni reduction via hydrogen spill-over effect which helps maintain Ni sites in active Ni⁰ state during the reaction in presence of oxidising agents such as water.

6.3 Recommendations

To complete the full understanding of additive effect of noble metal on Ni catalyst, some future works are recommended:

- (i) **Study the physical effect of the bimetallic samples using EXAFS modelling to analyse the nanocrystal structural changes in return changes the electronic properties of catalyst:** Ex-Situ EXAFS technique is utilize to measure the as-synthesised and reduced Pd, Rh or Ru-edges to find evidence whether the bi- or mono-metallic form an alloy phase or individual particles in the supported catalytic system. It describes that alloying effect of catalyst might enhance the rate of C-O/C-C bond cleavage during the APR of reaction.

- (ii) **Conduct a X-Ray Absorption Fine Structure (XAFS) study at the Ni-K edges:** The complement proposal to correlate with the analysis of Pd, Rh and Ru edges to give a comprehensive analysis of the short range order around the Ni atom by providing an estimate of the distances, coordination number and type of noble atoms surrounding the element. The chemical state of the Ni species converted between Ni(0) and NiO during the reduction processes and this results in increasing of the reduction temperature.
- (iii) **In-situ XAFS analysis of the Pd-K, Rh-K and Ru-K edges prior to and after APR reaction to study the phase change of samples during the reactions:** This study will use to clarify the change of the chemical state prior to and after APR reaction of the catalytic system in a H₂/Argon atmosphere to prevent any external interference, for instance air to re-oxidise reduced catalyst immediately.
- (iv) **The application in large-scale reactors should be considered when a screening and fundamental research were fulfilled:** Industrial uses of converting glycerol into rich hydrogen gas mixture to be an alternative to support the energy supply in the future.
- (v) **Further identify the liquid products in the liquid phase, to obtain a greater understanding of the intermediates reaction during APR of glycerol:** An alternative reaction pathway could be determine by identifying the intermediates reaction during APR of glycerol. Intermediates liquid product that might be useful in a APR of glycerol including glyceraldehyde, hydroxyacetone, propylene glycol, 1,2-ethanodiol, acetaldehyde, propanal, 1-propanal, 2-propanol, 1-propanol, ethanol, methanol, 2-methyl propylene, butane, pentane, acetic acid, propanoic acid and lactic acid.

6.4 References

- [1] R. Davda, J. Shabaker, G. Huber, R. Cortright, J. Dumesic, A review of catalytic issues and process conditions for renewable hydrogen and alkanes by aqueous-phase reforming of oxygenated hydrocarbons over supported metal catalysts, *Applied Catalysis B: Environmental*, 56 (2005) 171-186.
- [2] L. Liu, J. Fei, M. Cui, Y. Hu, J. Wang, XANES spectroscopic study of sulfur transformations during co-pyrolysis of a calcium-rich lignite and a high-sulfur bituminous coal, *Fuel Processing Technology*, 121 (2014) 56-62.

This page intentionally left blank

APPENDIX

Abstract

Illustrated appendix of the research thesis.

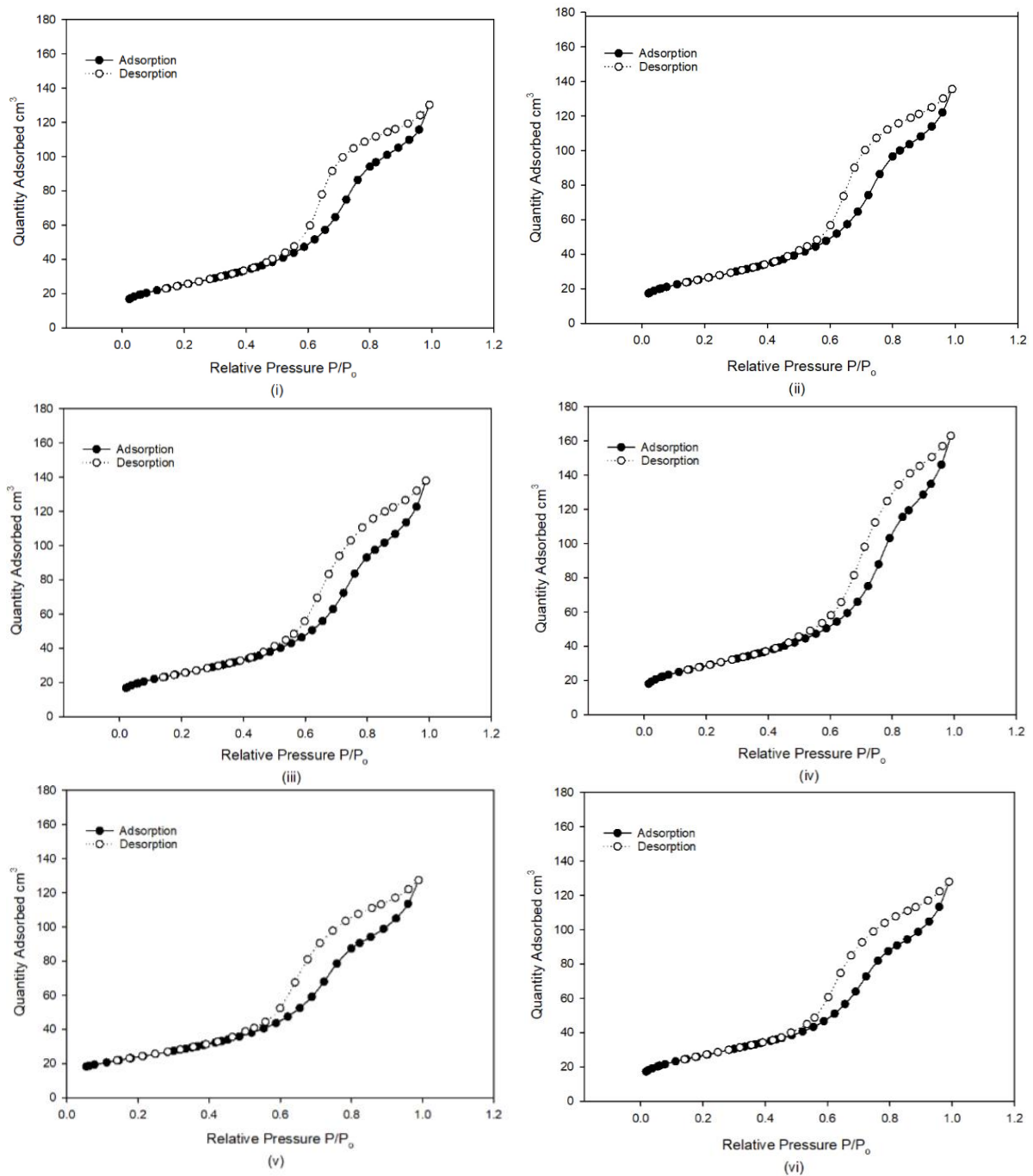
Chapter Contents

A.1	Catalyst Characterisation	90
A.1.1	Surface Area and Pore Structure by Physisorption	90
A.1.2	CO-Temperature Programmed Desorption (TPD)	92
A.2	APR Activity	94
A.2.1	Rate of Hydrogen Production and Glycerol Conversion	94
A.2.2	Rate of Carbon Dioxide and Carbon Monoxide Production	97

A.1 Catalyst Characterisation

A.1.1 Surface Area and Pore Structure by Physisorption

Isotherms of each catalyst were shown in the Figure A.1.1-1.



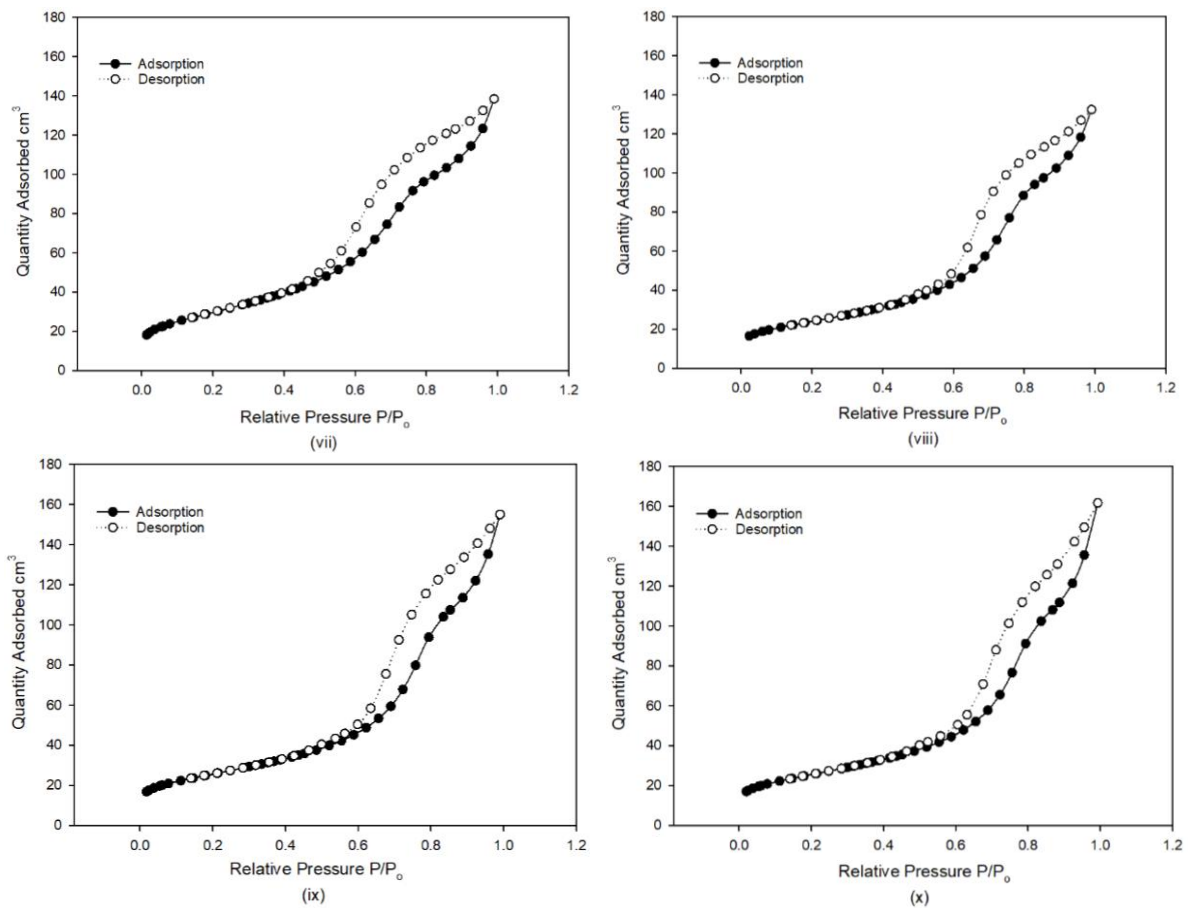
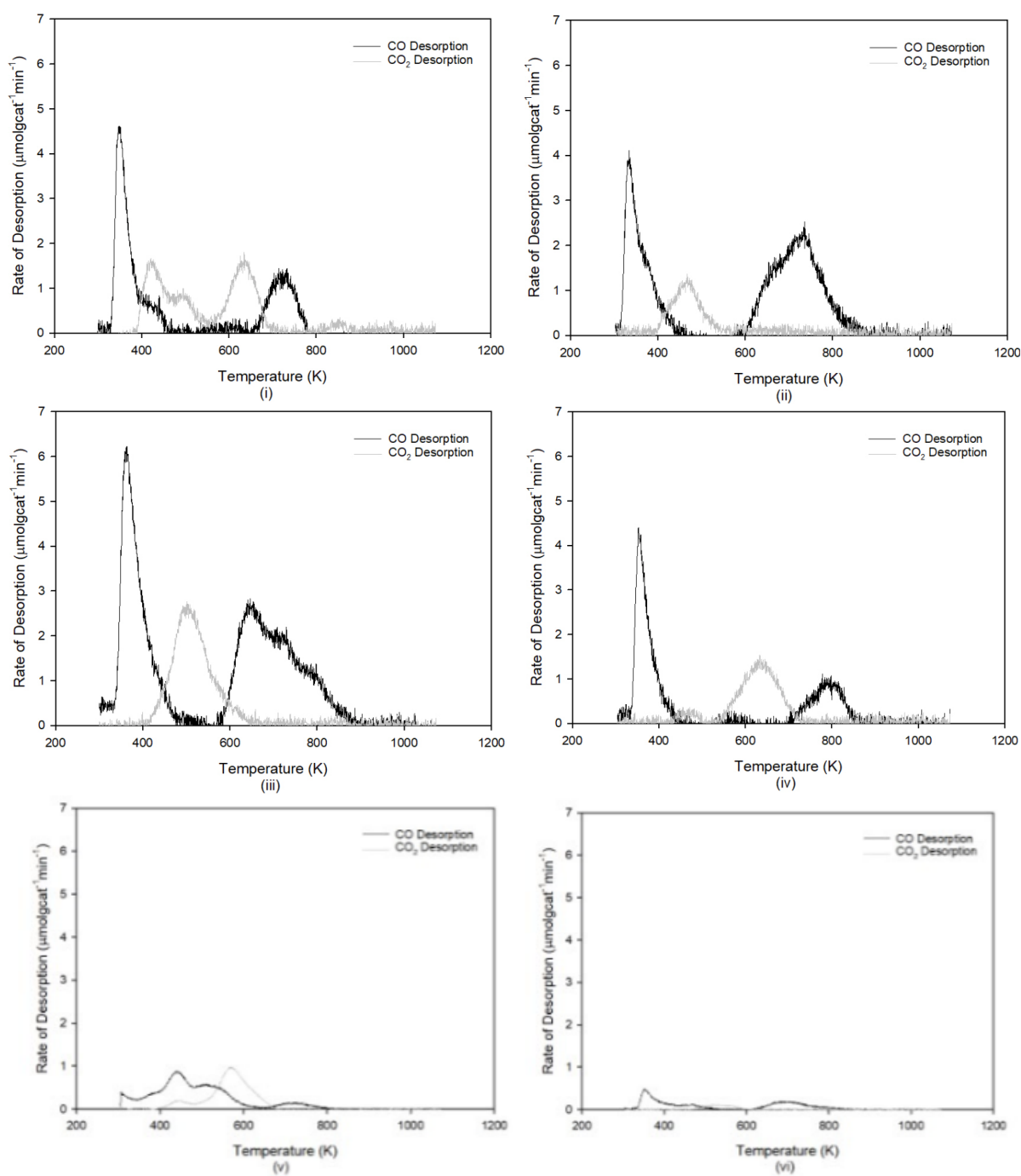


Figure A.1.1-1: N_2 physisorption isotherm linear plot of (i) Ni/Al_2O_3 (ii) $Ni:Pd(10:1)/Al_2O_3$ (iii) $Ni:Pd(1:1)/Al_2O_3$ (iv) Pd/Al_2O_3 (v) $Ni:Rh(10:1)/Al_2O_3$ (vi) $Ni:Rh(1:1)/Al_2O_3$ (vii) Rh/Al_2O_3 (viii) $Ni:Ru(10:1)/Al_2O_3$ (ix) $Ni:Ru(1:1)/Al_2O_3$ (x) Ru/Al_2O_3

A.1.2 CO-Temperature Programmed Desorption (TPD)

The CO-TPD profile of each catalysts were shown in Figure A.1.2-1.



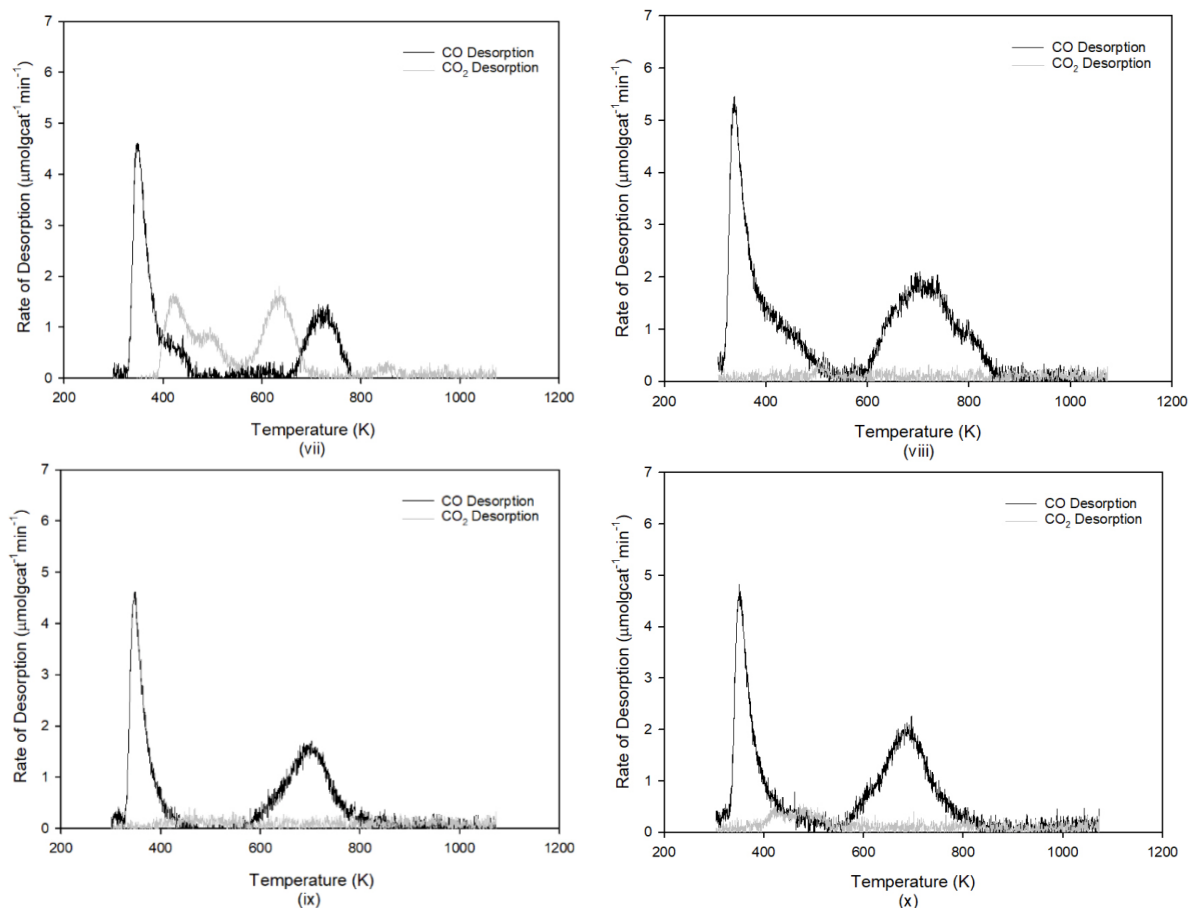
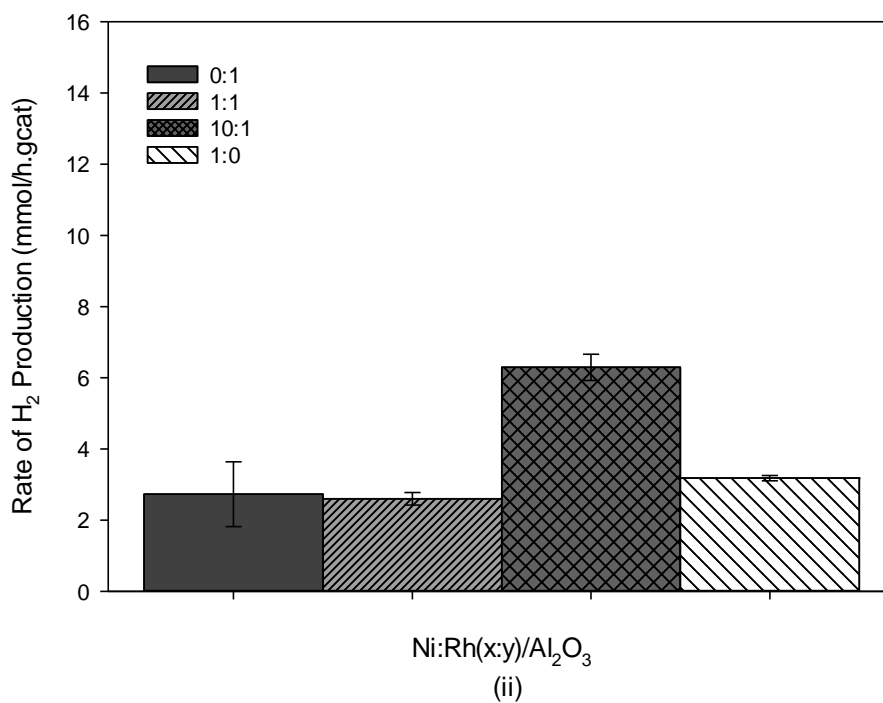
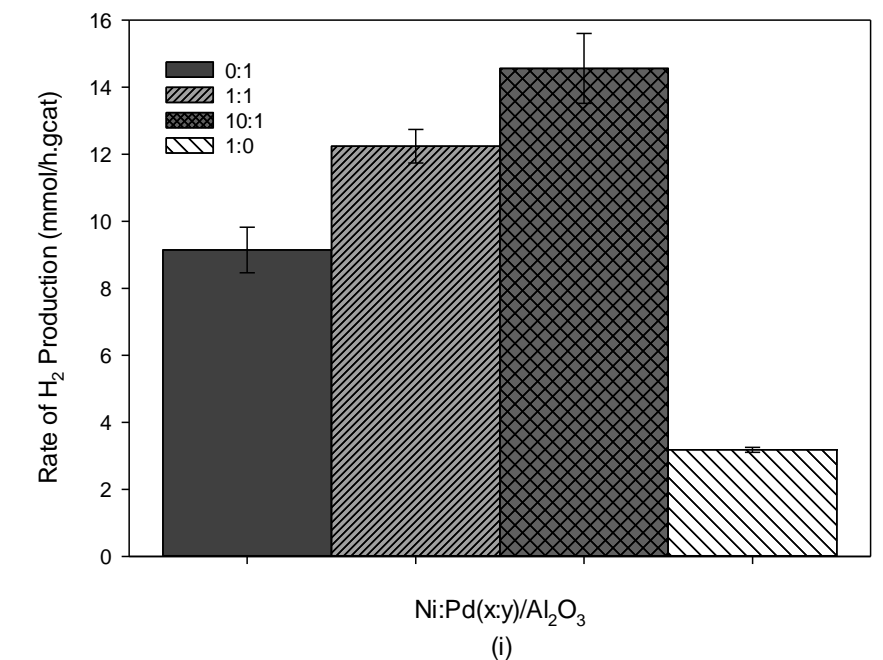


Figure A.1.2-1: Rate of CO and CO₂ desorption $\mu\text{molcat}^{-1}\text{min}^{-1}$ of (i) Ni/Al₂O₃ (ii) Ni:Pd(10:1)/Al₂O₃ (iii) Ni:Pd(1:1)/Al₂O₃ (iv) Pd/Al₂O₃ (v) Ni:Rh(10:1)/Al₂O₃ (vi) Ni:Rh(1:1)/Al₂O₃ (vii) Rh/Al₂O₃ (viii) Ni:Ru(10:1)/Al₂O₃ (ix) Ni:Ru(1:1)/Al₂O₃ (xi) Ru/Al₂O₃

A.2 APR Activity

A.2.1 Rate of Hydrogen Production and Glycerol Conversion



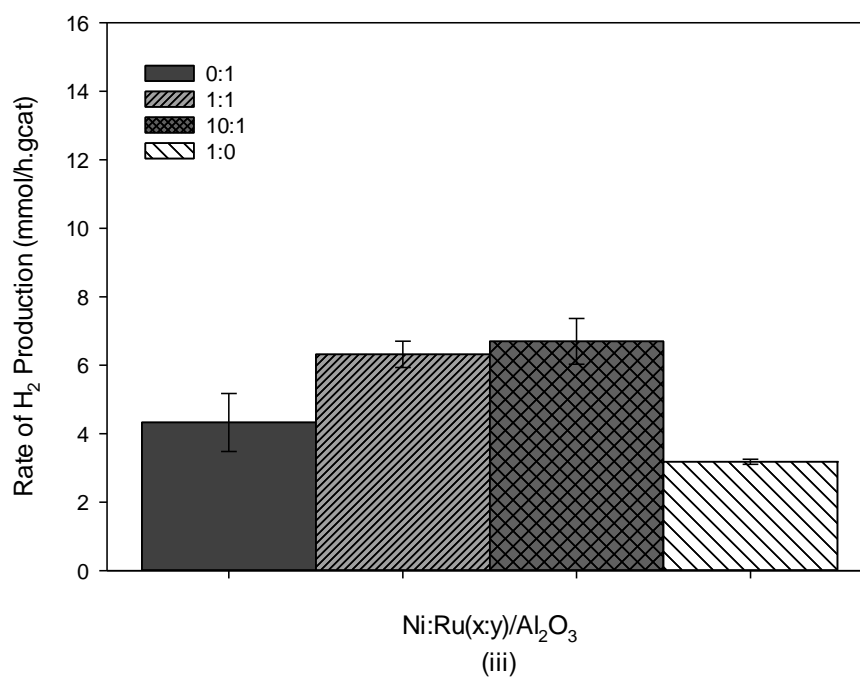
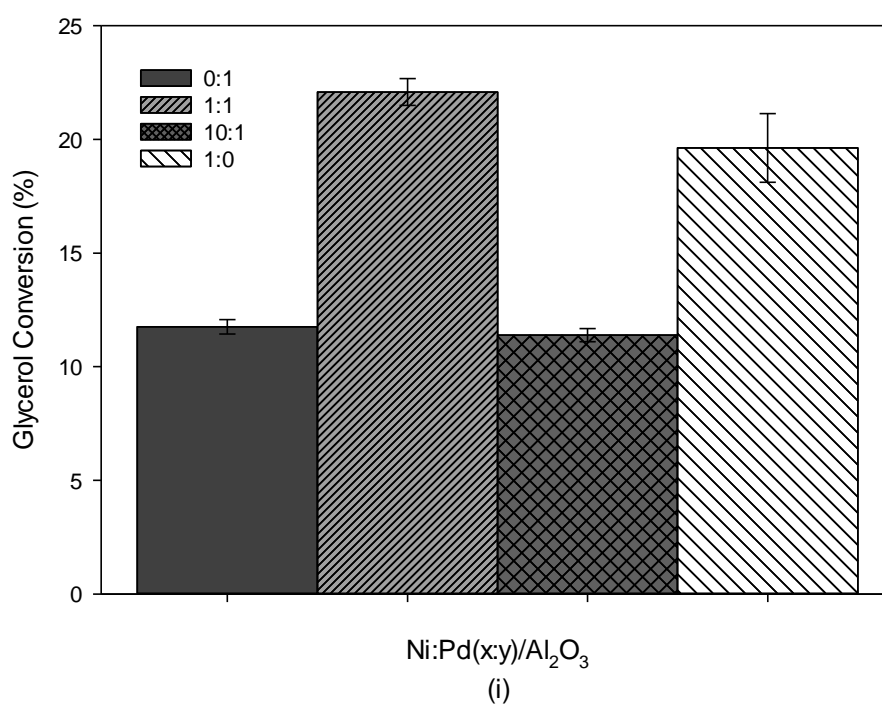


Figure A.1.1-1: : Rate of Hydrogen Gas Production with Standard Error Bar of Average 4 Runs (i) Ni:Pd(x:y)/Al₂O₃ (ii) Ni:Rh(x:y)/Al₂O₃ (iii) Ni:Ru(x:y)/Al₂O₃



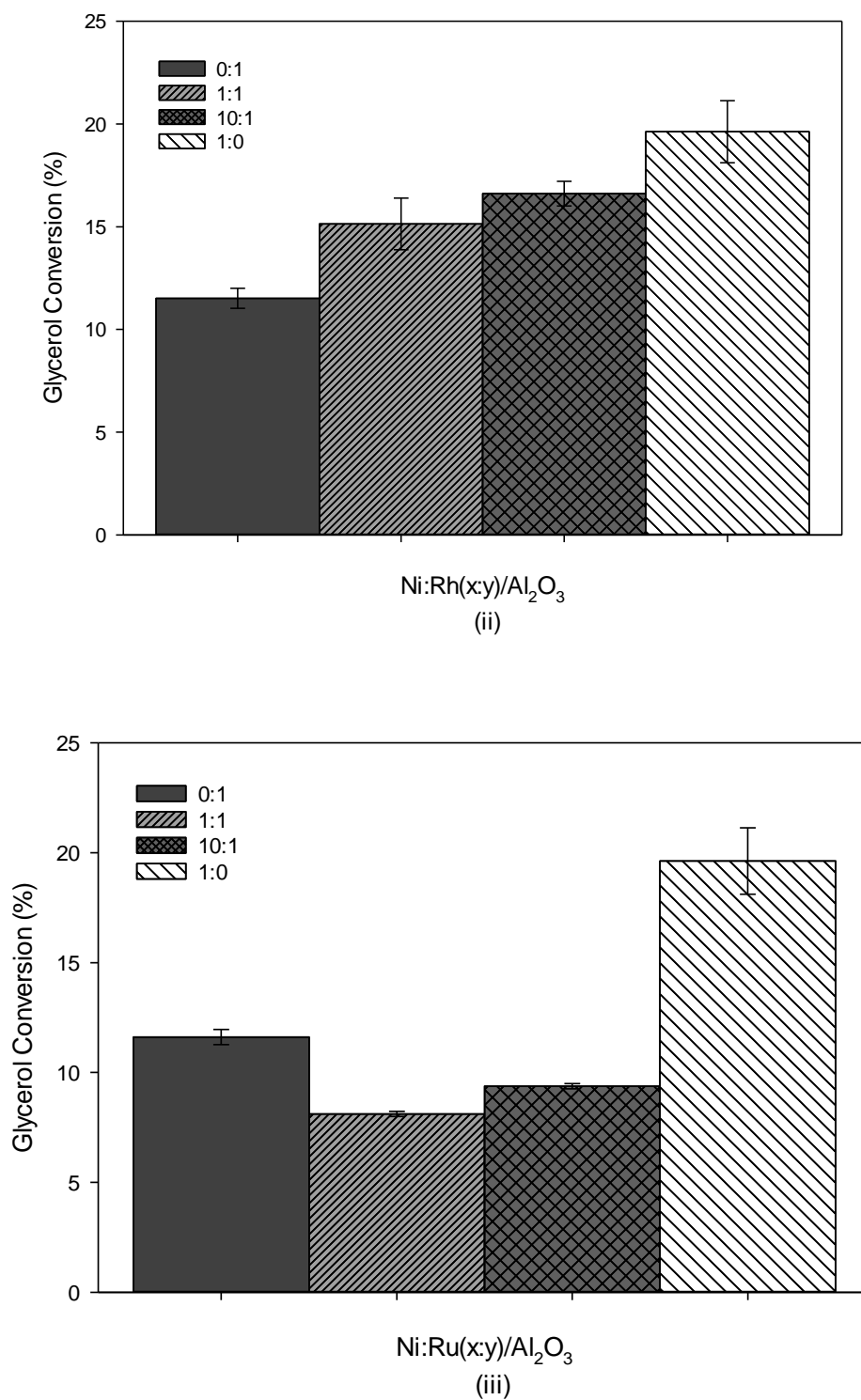


Figure A.2.1-2: Glycerol Conversion with Standard Error Bar of Average 4 Runs (i) Ni:Pd(x:y)/Al₂O₃ (ii) Ni:Rh(x:y)/Al₂O₃ (iii) Ni:Ru(x:y)/Al₂O₃

A.2.2 Rate of Carbon Dioxide and Carbon Monoxide Production

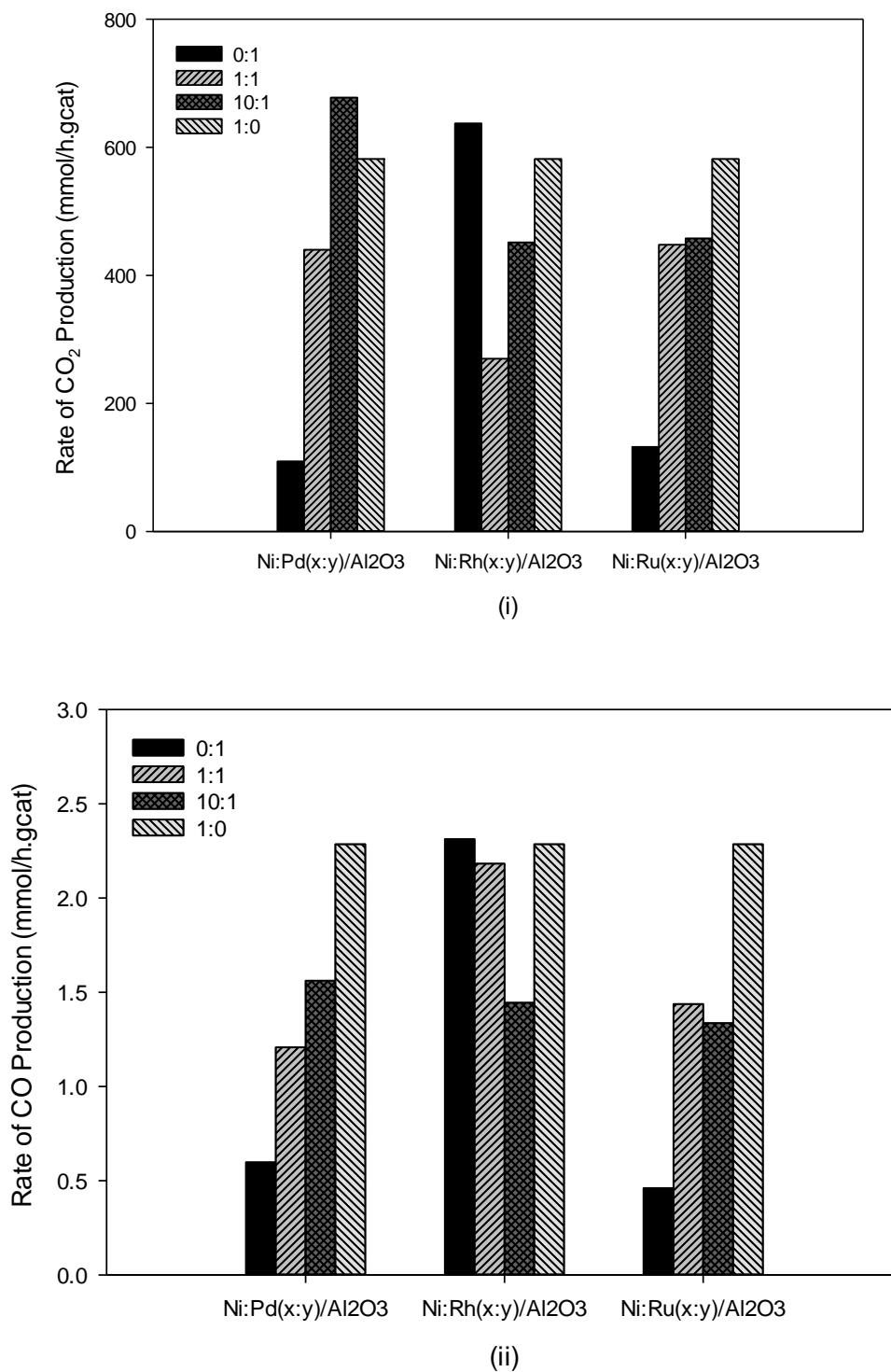


Figure A.2.2-1: Rate of (i) Carbon Dioxide and (ii) Carbon Monoxide production

This page intentionally left blank